FACULDADE DE ENGENHARIA DA UNIVERSIDADE DO PORTO

Development of a near-field anechoic chamber

Henrique José Silva Bastos Sul da Rocha

Mestrado em Engenharia Eletrotécnica e de Computadores

Supervisor: Luís Manuel de Sousa Pessoa

Co-Supervisor: Hugo Miguel Guedes Pereira dos Santos

July 27, 2023

Abstract

Antenna technology has rapidly advanced over the years, leading to more complex designs capable of beamforming. Although antenna sizes have been getting smaller, antenna arrays can still be large when compared to the wavelength of operation, which means that the far-field of the array can extend far beyond its surface. With the increased distance, measurements in the far-field can become unfeasible to perform in an anechoic chamber. A solution to this problem is to measure the antenna in the near-field.

The work presented in this dissertation focuses on the development of a multi-probe near-field measurement system. The algorithms involved in the transposition of the near-field information into the far-field are beyond the scope of this dissertation and are left for future work. Four probes were designed and tested using electromagnetic simulations, with one manufactured and measured using an existing far-field anechoic chamber. The Radio Frequency (RF) switching circuit and respective control circuitry were also developed and tested. Lastly, preliminary designs of the chamber structure and positioning system are proposed.

Resumo

A tecnologia em antenas avançou rapidamente ao longo dos anos, levando a modelos mais complexos capazes de direcionar o feixe de radiação. Embora o tamanho das antenas tenha diminuido, os *arrays* de antenas podem ser grandes quando comparados com o comprimento de onda de operação, o que significa que o campo distante se pode estender muito além da superfície do mesmo. Com o aumento da distância, torna-se inviável efetuar medições em campo distante numa câmara anecoica. Uma solução para este problema é fazer a medição da antena em campo próximo.

O trabalho apresentado nesta dissertação foca-se no desenvolvimento de um sistema de medição de campo próximo multi-sonda. Os algoritmos envolvidos na transposição da informação de campo próximo para o campo distante estão além dos objetivos definidos, sendo remetidos para trabalho futuro. Quatro modelos de sondas foram avaliados usando simulações eletromagnéticas, sendo que um dos modelos foi fabricado e avaliado experimentalmente usando uma câmara anecoica de campo distante, já existente. O circuito de comutação de Rádio Frequência (RF) e respetivo circuito de controlo foram também desenvolvidos e testados. Por fim, são propostos desenhos preliminares da estrutura da câmara e do sistema de posicionamento.

Acknowledgments

Hoping no one is left behind, I would like to give special thanks to

Professor Luís Pessoa for supervising this work and contributing with his expertise.

Professor Hugo Santos for co-supervising this work and contributing with his experience in RF circuit and antenna design.

all my family, especially my parents Henrique and Rosa, who supported me my whole life and especially during the development of this dissertation, encouraging me to conclude this work.

INESC TEC and FEUP for providing the required financial and technical resources.

all my friends and colleagues that either with technical help or unique friendship stood by my side keeping me motivated to achieve my objectives: João Araujo, Joana Tavares, Armando Rodrigues, António Barros, and Nuno Alves.

Henrique Rocha

"It's fine to celebrate success but it is more important to heed the lessons of failure."

Bill Gates

Contents

List of Figures

List of Tables

Abbreviations

AC	Alternating Current
ADS	Advanced Design System
AUT	Antenna Under Test
BALUN	Balanced to Unbalanced
CPWG	Coplanar Waveguide with Ground plane
DC	Direct Current
DMC	Diamond Microwave Chambers
DXF	Drawing Interchange Format
FET	Field Effect Transistors
HFSS	High-Frequency Structure Simulator
IC	Integrated Circuit
LASER	Light Amplification by Stimulated Emission of Radiation
LHCP	Left Hand Circular Polarization
MEMS	Micro Electronic Mechanical Systems
MIMO	Multiple Input Multiple Output
MOSFET	Metal Oxide Field Effect Transistor
MVG	Microwave Vision Group
NMOS	N-channel MOSFET
OBD++	Open Database ++
PCB	Printed Circuit Board
PIN	Positive Intrinsic Negative
PN	Positive Negative
PMOS	P-channel MOSFET
RF	Radio Frequency
RHCP	Right Hand Circular Polarization
SBR+	Shooting and Bouncing Rays +
SPDT	Single Pole Double Throw
SPTT	Single Pole Triple Throw
TEM	Transverse Eletromagnetic
UHF	Ultra High Frequency
USB	Universal Serial Bus
VHF	Very High Frequency
VISA	Virtual Instrument Software Architecture
VNA	Vector Network Analyzer
VSWR	Voltage Standing Wave Ratio

Chapter 1

Introduction

1.1 Motivation

With an increasing number of devices and the demand for wireless connectivity between them, the use of antennas for establishing communication in the physical layer is mandatory. With the advance in technology, tighter requirements in antenna design arise. For example, in 5G communication (Figure 1.1), the use of beamforming allows for the use of less power by shaping the antenna's radiation pattern in such a way that the receiving device has maximum signal power.

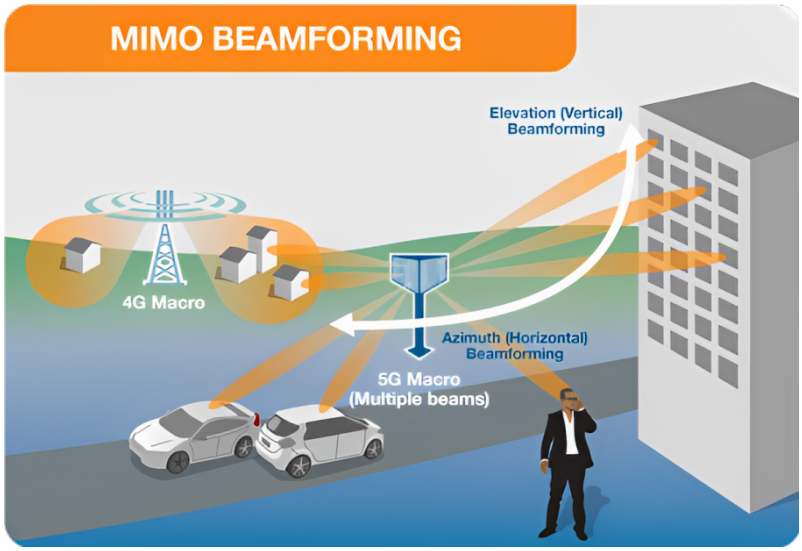

Figure 1.1: 5G beamforming example using MIMO [1].

To validate the correct operation of the base station antenna *i.e.* the main lobe of the antenna is pointing to the desired direction, experimental tests are undertaken. For this purpose, anechoic chambers are used to allow for a low interference space to collect data.

Usually, anechoic chambers, like the one shown in Figure 1.2, are designed to operate in the far-field of an antenna. This means that the probe antenna is sufficiently far away from the

Antenna Under Test (AUT) so that the radiated wave front, emitted either by the AUT or the probe, depending on the experimental setup, when received, can be considered as a plane wave.

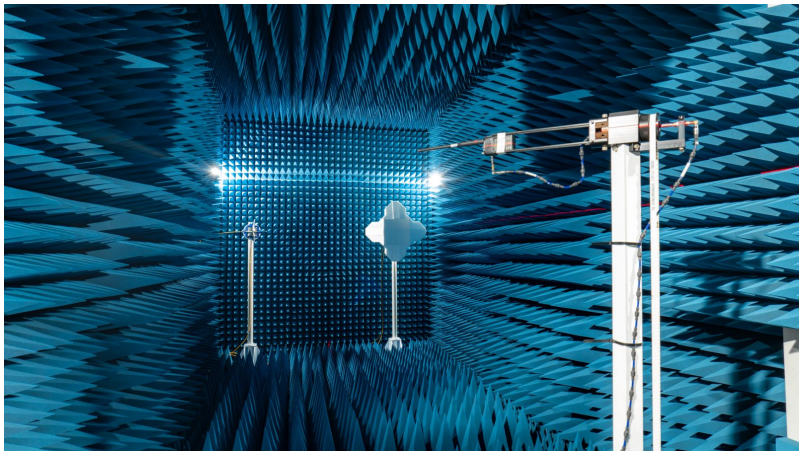

Figure 1.2: Far-field anechoic chamber [2].

The minimum distance required between devices is analyzed in section 2.2. For example, an antenna with its biggest dimension being ten wavelengths operating at 3 GHz, according to [3], would require the probe to be at least 20 m away from the AUT. By comparison, the near-field from the previous example starts at a tenth of the distance, meaning that the space required to characterize this antenna would decrease tenfold when using a near-field measuring technique, in this case.

Furthermore, a near-field chamber could also operate in the far-field, depending on the antenna size and frequency of operation. This is possible because near-field equations are also valid in the far-field, though the opposite does not apply, adding one more benefit to the use of near-field chambers. Although near-field equations are valid in the far-field, the standard for antenna parameters refers to the far-field conditions, as such, conversion algorithms are used to transpose the data collected to the far-field.

To further increase the advantage of an anechoic chamber, a three-dimensional measurement system can be used to better characterize the antenna in space. Usually, the antenna is only measured on two planes or put simply, in two orthogonal planes, for example, the electric and magnetic field planes of a dipole antenna. This is done as a compromise between detail in the measurements, the complexity of the system used and the time it takes to perform said measurements. This method is acceptable for single, and relatively simple, antennas, but starts to lose the ability to portray the radiation pattern for more complex antennas, such as arrays capable of generating multi-beam, in this case, a full 3D characterization is desirable. Such measurements can be performed in the far-field, though, as described above the dimensions required for such a technique can become physically large. Regardless, two types of systems can be used to measure the AUT, single probe or multi-probe.

Single probe systems require that the AUT positioner rotates in two axes, assuming that the

probe used is dual-polarization (vertical and horizontal) so that the polarization alignment is maintained. With dual polarization a combination of vertical and horizontal polarization can be used to emulate a single polarization antenna rotated by a given amount, this way the alignment is maintained. The AUT positioner will need to rotate three hundred and sixty degrees in the horizontal and vertical planes, to cover all directions.

Multiple probe systems also use one positioner, assuming that the probes used are also dual-polarization, for the same reason described above, though in this case, the probes surround the AUT, meaning that the positioner only needs to rotate in one plane, reducing mechanical complexity but at the same time increasing electrical complexity. The main advantages of using the described system are the reduced measuring time not only because RF switches are faster than a mechanical positioner but also because if the probes fully surround the AUT then the rotation is reduced to one hundred and eighty degrees. In some cases, the probes surrounding the AUT can be rotated around it to further increase the measurement points, essentially doing a mechanical interpolation, as illustrated by Figure 1.3.

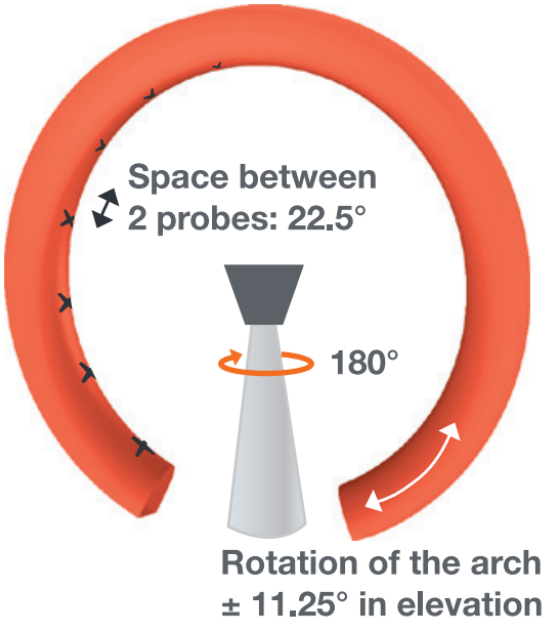

Figure 1.3: Multiple probe measurement system [4].

Usually, multi-probe systems are not used in far-field chambers due to the dimensions required to do so, specifically for low frequencies and large antennas. For high frequencies, for example, millimeter waves, the far-field boundary starts to be at an acceptable distance from the AUT, although the cost of the probing system also increases.

1.2 Objectives

Considering the challenges described in the previous section, the main objective of this dissertation is to develop a near-field measurement system that is capable of characterizing an AUT in

three dimensions. It must implement a multi-probe system similar to the one presented in Figure 1.3, though the probes are not required to perform mechanical interpolation, to simplify the system. Furthermore, the system should be capable of operating from 1 to 30 GHz. To fulfill these objectives, all the subsystems must also be developed, as described below.

The mechanical subsystem includes the measurement structure (an arch) that holds the probes and the positioner that rotates the AUT. The structure must also be designed in a way that the reflections are kept to a minimum to obtain the best results possible. The positioning system should have adjustment mechanisms to allow the AUT to be centered in the measurement system.

The electrical subsystem includes dual polarization probes and a switching circuit along with the control circuitry. The probes are only required to receive signal, meaning that the measurement system will be unidirectional, where the signal originates from the AUT and is radiated to the probes that surround it. The signal received by the probes must be switched with $2N$ (one input per polarization) inputs and one output, where N is the number of probes used. The measurement systems should also be modular, and easily connectable, to allow for more probes to be added, or fewer to be used, depending on the radius of the measurement structure. Furthermore, the goal is to have a dual polarization probe designed in PCB, where the vertical and horizontal polarizations are fitted together in one assembly.

At the end of the work, it is expected to have at least one probe and switching circuit along with the positioner control circuit operational and connected to the control circuitry. As the conversion algorithms that transpose the near-field information into far-field are outside the scope of this dissertation the probes will be designed and measured in the far-field, although following the requirements imposed by the conversion algorithms.

1.3 Contributions

The main contributions of this dissertation are summarized below:

- Development of a dual polarization near-field probe;
- Modular RF switching circuit integrated into the probe's design;
- Preliminary measurement structure analysis;
- Four axis positioning structure to align the AUT.

1.4 Document Structure

This dissertation is organized into eight chapters. This chapter presents an overview of the work along with the motivations, objectives and document structure. Following the first, chapter 2 provides the fundamentals needed for the comprehension of this dissertation. Chapter 3 shows the research that was made on the systems to be developed. In chapter 4 the design process of the switching circuit used is described. Chapter 5, 6 and 7 follow the same structure, describing the

design process of each subsystem. In chapter 5, the digital control circuitry developed is described, while in chapter 6, four probe designs were studied. However, in Chapter 7 only a preliminary study of the structure of the chamber and the positioning system was performed, due to the limited time available.

Chapter 2

Background

2.1 Antenna Fundamentals

An antenna is a passive device that converts an electric signal into free-space electromagnetic waves and vice-versa. In some applications, an antenna is accompanied by active circuitry for transmission or reception, and sometimes both, becoming a transceiver. In a situation where an antenna is combined with dedicated driving circuitry, it is designated as an active antenna. An antenna can be characterized by certain parameters such as directivity, efficiency, radiation pattern, and polarization, among others. In this section, some underlining concepts are given to support the following topics, in which the rationale follows the work of Balanis [3].

2.1.1 Radiation Mechanism

To understand how an antenna operates, we first need to understand how the radiation mechanism works. To answer this question, we can start by analyzing the flow of electric charge in a single wire.

Considering a very thin, straight and perfectly conductive wire, so that, the current analysis can be reduced to the thin wire (ignoring surface charges), oriented along the Z axis, equation (2.1)[3, p.9] expresses the derivative of the current in the wire (along the Z axis) as a function of the charge per unit length q ($\mathrm{C\,m^{-1}}$) and the change in charge velocity, v_z ($\mathrm{m\,s^{-1}}$).

$$\frac{dI_z}{dt} = q\frac{dv_z}{dt} = qa_z \tag{2.1}$$

From equation (2.1) we can conclude that the change in current is directly related to the acceleration of the charges. Considering a wire of length l, equation (2.1) can be rewritten as equation (2.2)[3, p.9].

$$l\frac{dI_z}{dt} = lqa_z \tag{2.2}$$

In fact, equation (2.2) is the basic relation between current and charge, also serving as the fundamental relation of electromagnetic radiation [5], [6]. In other words, to radiate, there must

be a change in the velocity of the charges, *i.e.* an acceleration applied to them. In a situation where the current applied to the wire is constant, radiation can only exist if the conductor is curved, bent, cut or terminated [7], [5], which means that there will be a change in direction, and thus a change in velocity of the charges, as illustrated by Figure 2.1.

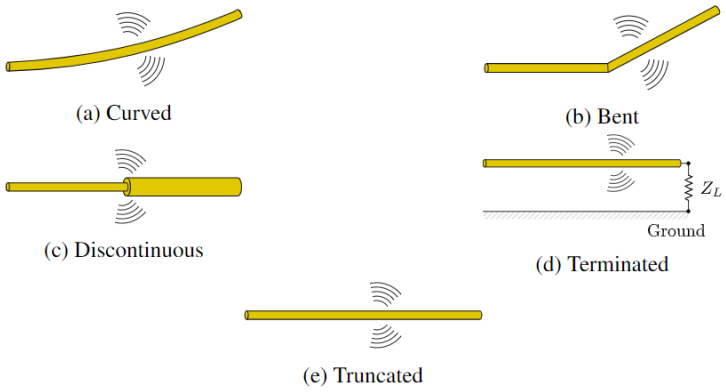

Figure 2.1: Radiative single wire configurations [8, p.8].

We now consider an oscillating source connected to a two-conductor transmission line (parallel wires) that is connected to an antenna, as illustrated by Figure 2.2.

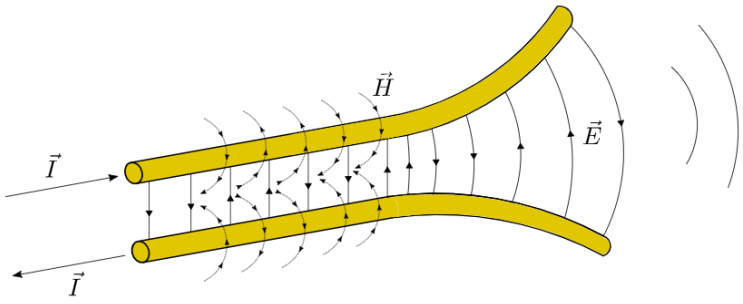

Figure 2.2: Two-wire radiating system, with electric and magnetic field lines represented [8, p.8].

In a two-wire system, a Transverse ElectroMagnetic (TEM) wave exists in the space between the conductors that form the transmission line, as illustrated by Figure 2.2. Furthermore, in this configuration, the TEM wave will also be radiated at the end of the line.

Nevertheless, other types of radiation mechanisms exist like the one present in aperture antennas [8, p.8]. For example, at the end of an open waveguide, there will be radiated waves. The amount of radiation will depend on the aperture at the end of the waveguide, as there will be a discontinuity in wave impedance, between the air and the transmission line. Similarly to the example presented in Figure 2.2, a horn antenna uses a tapered aperture to gradually match the impedance of the wave inside the transition line to the wave impedance in the propagation media (usually air), as illustrated by Figure 2.3.

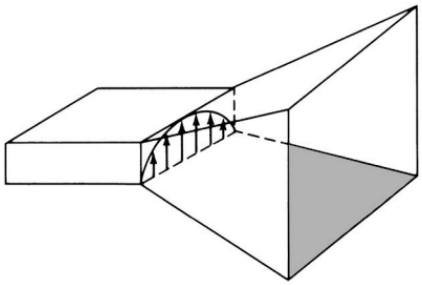

Figure 2.3: Horn antenna with waveguide feed [3, p.720].

2.1.2 Radiation Pattern

An antenna radiation pattern is a graphical representation of the radiation properties of an antenna. Typically, the radiation pattern is represented in the far-field and can portray more than one property of the antenna such as power flux density, radiation intensity, field strength, directivity, phase or polarization [3, p.25]. Radiation patterns can be represented in two dimensions, usually one for the electric field (E) plane and one for the magnetic field (H) plane, or in three dimensions. An example of a three-dimensional pattern is illustrated by Figure 2.4, where the scale of colors represents the antenna gain in decibels, where dark red represents the maximum and dark blue (visible only from above) represents the minimum.

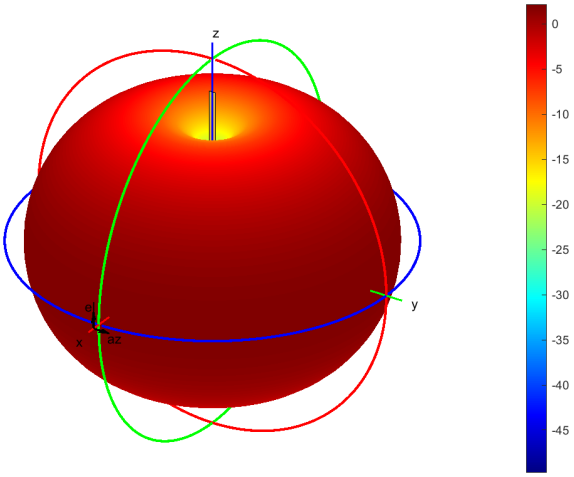

Figure 2.4: Three-dimensional radiation pattern for a $\lambda/2$ dipole.

Furthermore, for the cases where the radiation pattern is more complex, other characteristics can be defined, as illustrated by Figure 2.5. In this case, the radiation pattern has more than one lobe, meaning that the energy is mostly radiated in the direction of the main lobe, but it is also radiated in the direction of the secondary lobes. We can also observe that when this is the case, the phase of the wave is shifted by half a cycle from one lobe to the next.

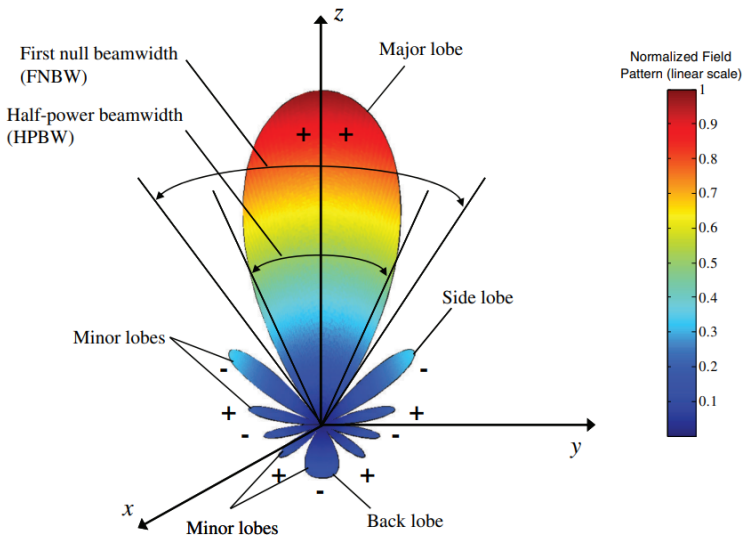

Figure 2.5: Radiation pattern characteristics [3, p.28].

2.1.3 Gain

An essential parameter for the measurement of the radiation pattern of an AUT is the gain of the probe antennas since without it only a relative measurement can be performed, usually, as a function of the maximum power received.

Gain (G) of an antenna is defined as the ratio, in a given direction, of the field intensity to the one obtained if an isotropic antenna was used. The average radiation intensity (U_{av}) corresponding to the isotropically radiated power is equal to the power accepted (P_{in}) by the antenna divided by 4π [3, p.61], as illustrated by equation (2.3)[9], where $U(\theta,\phi)$ is the radiation intensity in the direction defined by θ and ϕ, and P_{in} is the total power absorbed by the antenna.

$$G(\theta,\phi) = \frac{U(\theta,\phi)}{U_{\text{av}}} = 4\pi\frac{U(\theta,\phi)}{P_{\text{in}}} \tag{2.3}$$

Furthermore, the gain is often defined as a relative gain, where P_{in} is equal in both antennas [3, p.62]. The most common reference antenna is a lossless isotropic antenna, in this case, when the gain is presented in decibel scale, the unit used is dBi. When no direction is specified, the gain is considered to be the one in the direction of maximum radiation.

Another useful parameter is the realized gain, which is obtained by multiplying the gain obtained in (2.3) by the mismatch efficiency, given by equation (2.7). The realized gain is a better way to compare antennas as it includes the power reflected in the feed port.

2.1.4 Polarization

On the one hand, the polarization of an antenna in a given direction is defined as the polarization of the wave transmitted (radiated) by it. Similarly to the gain, when the direction is not stated, the polarization is considered to be the one in the direction of maximum gain. [3, p.66].

On the other hand, the polarization of a wave is defined as the direction and relative magnitude of the time-varying electric-field vector, more specifically, the figure traced as a function of time by the extremity of the vector at a fixed location in space [3, p.66]. In other words, it can be seen as the vector that is collinear with the electric field vector at any point of the far-field [8, p.13].

Furthermore, wave polarization can be categorized into two main groups: linear and circular. The most common polarization is the linear one, as it is simpler than the other, allowing for simpler antenna designs. One of the drawbacks of using this polarization is the importance of antenna alignment, as polarization mismatch will degrade the power received by a factor of $\cos(\Psi)$, where Ψ is the angle between the polarization of the two antennas [8, p.14].

In circular polarization, the electric (E) field rotates in time. This polarization can be obtained by superimposing two linearly polarized waves, generated by two perpendicular dipoles, for example. The main advantage of using circular polarization is the insensitivity to misalignment of the axes of the antennas used. Furthermore, circular polarization can be subdivided into right-hand circular polarization (RHCP) and left-hand circular polarization (LHCP). Given that an antenna designed for right-hand polarization greatly attenuates left-hand polarization, multipath reflections can be mitigated. This is because a right-hand polarized wave becomes left-hand polarized when reflected. Figure 2.6 illustrates the rotation of the electric field vector in time for an RHCP wave.

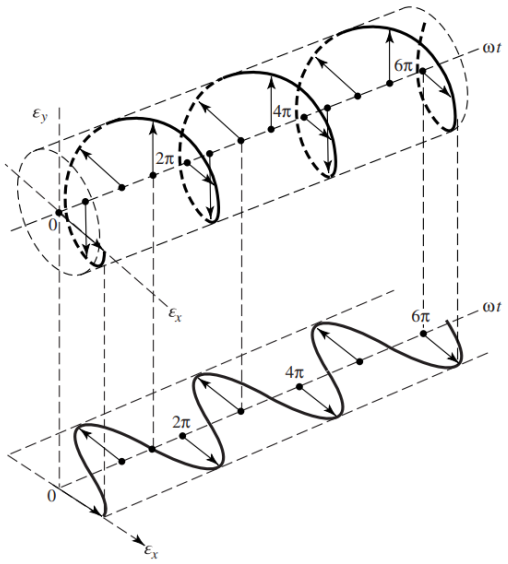

Figure 2.6: Circularly polarized wave (RHCP) [3, p.67].

2.1.5 Input Impedance

Input impedance is the impedance viewed by the transmission line into the antenna terminals [3, p.75]. An antenna can be modeled as discrete inductors capacitors and resistors, as such, its input impedance will depend on the operating frequency. For maximum power transfer, the input impedance must match the impedance of the transmission line that is connected to it, as illustrated by equation (2.4). Due to the vast variety of antenna designs, the input impedance was determined

analytically for a limited number of practical antennas [3, p.79]. For all other cases, it has to be determined in simulation, using an electromagnetic simulator (eg. ADS, HFSS), or experimentally with a Vector Network Analyser (VNA).

2.1.6 Bandwidth

The bandwidth of an antenna can be seen as the range of frequencies within which the performance of the antenna remains within the specified interval concerning some antenna characteristic [10]. In other words, bandwidth can be considered a range of frequencies, usually centered in the resonant frequency of the antenna, in which the antenna parameters are within an acceptable range when compared to the ones at the center frequency. Usually, more than one antenna parameter changes with frequency, with some altered faster than others, as such, bandwidth can be defined by one or more parameters, depending on the application. For use in an anechoic chamber, the most relevant parameters are the radiation pattern and the input impedance, as the last will affect the realized gain. Even though these can be compensated with post-processing of the data collected, ideally the probe antennas would have constant parameters within the operation bandwidth. Concerning the radiation pattern, this would have to be characterized in simulation using the parameters defined in subsection 2.1.2. Regarding the input impedance, its bandwidth is usually characterized by the reflection coefficient (Γ) or the Voltage Standing Wave Ratio (VSWR). In most antennas, it can be seen that the restrictions in terms of reflection coefficient are VSWR < 2, equivalently $|\Gamma| < 0.3$ or in decibel $|\Gamma|_{\text{dB}} < -10$. These are well-known quantities from transmission line theory [8, p.12], which are given by equation (2.4)[11], where Z_{in} is the antenna's input impedance and Z_0 the characteristic impedance of the transmission line that feeds the antenna.

$$\Gamma = \frac{Z_{\text{in}} - Z_0}{Z_{\text{in}} + Z_0} \tag{2.4}$$

The VSWR is related to the reflection coefficient by equation (2.5)[11].

$$\text{VSWR} = \frac{1 + |\Gamma|}{1 - |\Gamma|} \tag{2.5}$$

Furthermore, it is also usual to define antenna parameters in terms of scattering parameters. The S_{11} parameter is given to evaluate the impedance bandwidth of an antenna and it coincides with Γ, for one-port antennas [8, p.12]. Its magnitude, in decibels, is given by equation (2.6)[8, p.12].

$$|S_{11}|_{\text{dB}} = |\Gamma|_{\text{dB}} = 20\log_{10}(|\Gamma|) \tag{2.6}$$

Another measurement that can be defined is the mismatch efficiency (η_{m}), which is the ratio of incident power to the power which is delivered to the antenna, it represents how good the matching between the transmission line and the antenna is. Equation (2.7)[3, p.60] defines mismatch efficiency as a function of S_{11}.

$$\eta_{\mathrm{m}} = 1 - |S_{11}|^2 \tag{2.7}$$

2.1.7 Phase Center

The phase center of an antenna is the point of reference for the phase of the wave emitted. In other words, if a sphere is centered in the phase center, then for any fixed distance from the center point, r, the phase of the wave at the surface of the said sphere is the same for the whole surface [12, p.1]. The phase center is relevant when performing antenna measurements because the AUT is rotated to plot a radiation pattern. To ensure that the phase of the received signal remains constant, the center of rotation has to coincide with the phase center of the AUT.

2.2 Region Limits

The space surrounding an antenna is usually subdivided into three regions: reactive near-field, radiating near-field or Fresnel and far-field or Fraunhofer regions, as shown in Figure 2.7. The computations for the region boundaries will be performed next. Even though there are no abrupt changes in the fields when crossing a boundary, there are distinct differences among them. The boundaries separating these regions are not unique, although several criteria have been established and are commonly used to identify the regions [3, p.31].

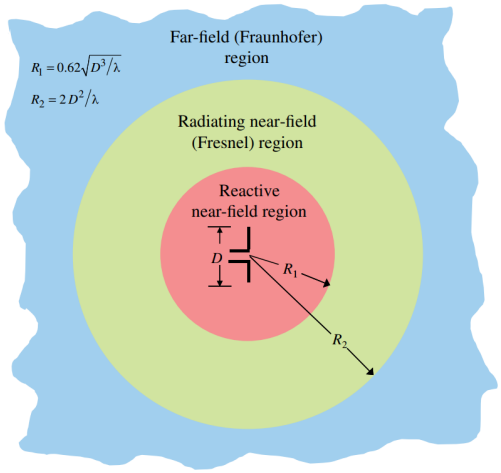

Figure 2.7: Field regions of an antenna [3, p.32].

2.2.1 Far-field

Far-field (Fraunhofer) region is the region of space where the field of an antenna has its angular field distribution essentially independent of the distance from the source. In this region, the field components are essential transverse and the angular distribution is independent of the radial distance where the measurements are performed [3, p.32]. In other words, the wavefront is *quasi* planar and a TEM wave propagates. Also, the energy transported by the fields in a given time

(power) is mostly real, meaning that it represents radiative power. To compute the lower boundary of this region (the upper boundary being infinity), the following computations can be done, based on the phase error in the wavefront. We start by computing the distance R, as illustrated by Figure 2.8, in equation (2.8)[3, p.159].

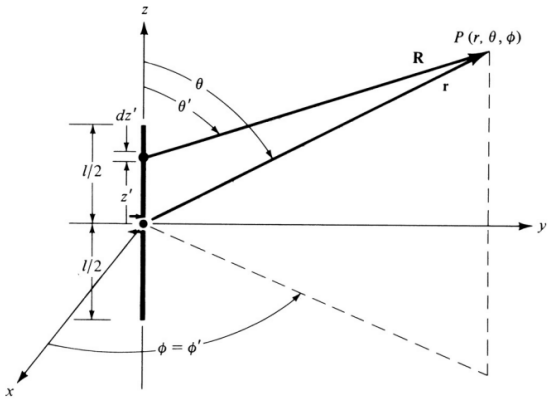

Figure 2.8: Finite length dipole geometry [3, p.160].

$$R = \sqrt{r^2 + (-2rz'\cos(\theta) + z'^2)} \tag{2.8}$$

Using the binomial expansion, we can write equation (2.8) in a series as illustrated by equation (2.9)[3, p.159], whose higher order terms become less significant provided $r \gg z'$.

$$R = r - z'\cos(\theta) + \frac{1}{r}\left(\frac{z'^2}{2}\sin^2(\theta)\right) + \frac{1}{r^2}\left(\frac{z'^3}{2}\cos(\theta)\sin^2(\theta)\right) + \ldots \tag{2.9}$$

In this region of space, the most convenient approximation is the one performed in equation (2.10)[3, p.160], where R is approximated by the first two terms of equation (2.9), considering that all others are close to zero.

$$R \approx r - z'\cos(\theta) \tag{2.10}$$

The most significant term discarded in (2.9) is the third, whose maximum value is given by equation (2.11)[3, p.160], which means that as this term can be seen as the approximation error.

$$\frac{1}{r}\left(\frac{z'^2}{2}\sin^2(\theta)\right)_{\max} = \frac{z'^2}{2r} \qquad \text{when } \theta = \pi/2 \tag{2.11}$$

It has been shown by many researchers through numerous examples that for most practical antennas, with overall lengths greater than a wavelength ($l > \lambda$), a maximum total phase error of $\pi/8$ rad (22.5°) is not very detrimental in the analytical formulations [3, p.161]. With this in mind, we can rewrite equation (2.11) multiplied by $k = 2\pi/\lambda$ (wavenumber), which converts the distance, relative to the wavelength λ, into phase, resulting in equation (2.12)[3, p.161].

$$k\frac{z'^2}{2r} \leq \frac{\pi}{8} \tag{2.12}$$

Considering that the antenna is centered at the origin and has a total length of l, equivalent to $-l/2 \leq z' \leq l/2$, then:

$$r \geq 2\left(\frac{l^2}{\lambda}\right) \tag{2.13}$$

Equation (2.13)[3, p.161] states that to maintain the minimum phase error of 22.5° the distance r to the antenna has to be greater than $2l^2/\lambda$, where l can be taken as the largest dimension of the antenna provided that it is large when compared to the wavelength [10].

2.2.2 Radiating Near-field

Following the same line of thought for this region, we can define a maximum phase error equal to the one defined previously, but now adding an extra term to better approximate R to the real distance between point P and the point contained in the antenna (shown in Figure 2.8), as illustrated by equation (2.14)[3, p.162].

$$R \approx r - z'\cos(\theta) + \frac{1}{r}\left(\frac{z'^2}{2}\sin^2(\theta)\right) \tag{2.14}$$

The most significant term discarded from equation (2.9) is the fourth, including one more term in the equation, when compared to the last region. To find the maximum phase error, the fourth term relative to θ just needs to be differentiated and set equal to zero, as illustrated by equation (2.15)[3, p.162].

$$R = \frac{\partial}{\partial\theta}\left[\frac{1}{r^2}\left(\frac{z'^3}{2}\cos(\theta)\sin^2(\theta)\right)\right] = \frac{z'^3}{2r^2}\sin(\theta)[-\sin^2(\theta)+2\cos^2(\theta)] = 0 \tag{2.15}$$

The trivial solution $\theta = 0$ represents the minimum phase error, as such, the maximum is given by equation (2.16)[3, p.162].

$$-\sin^2(\theta)+2\cos^2(\theta) = 0 \tag{2.16}$$

Resulting in $\theta = \tan^{-1}\left(\pm\sqrt{2}\right)$. If this value is applied to the fourth term of equation (2.9), multiplied by k to convert the distance to phase, and considering that the antenna is centered in the origin, we obtain [3, p.163]:

$$\frac{kz'^3}{2r^2}\cos(\theta)\sin^2(\theta) = \frac{\pi}{12\sqrt{3}}\left(\frac{l^3}{\lambda r^2}\right) \leq \frac{\pi}{8} \tag{2.17}$$

which reduces to

$$r \geq 0.62\sqrt{\left(\frac{l^3}{\lambda}\right)} \tag{2.18}$$

We now have the lower boundary of this region, limited by equation (2.18)[3, p.163]. Considering that the upper boundary is set by equation (2.13) (the lower boundary of the far-field), then the radiative near-field region is defined for every r that satisfies equation (2.19). Furthermore, the boundaries for separating the far-field (Fraunhofer), the radiating near-field (Fresnel), and the reactive near-field regions are not very rigid. Other criteria have also been established [13]. Nevertheless, the boundaries introduced are the most commonly used. Also, as previously stated, the fields are continuous, as such, the transition between regions is gradual.

$$0.62\sqrt{\left(\frac{l^3}{\lambda}\right)} \leq r < \frac{2l^2}{\lambda} \tag{2.19}$$

2.2.3 Reactive Near-Field

The reactive near-field region is the space immediately surrounding the antenna wherein the reactive field or reactive power predominates [3, p.31]. In other words, there is energy being exchanged between the propagation media and the antenna. Because of this, everything that is inside the reactive near-field region will affect the antenna operation. This is why no measurements can be taken in this region of space without significantly altering the results. This region of space is limited by the lower boundary of the radiating near-field and the antenna ($r = 0$), as illustrated by equation (2.20)[3, p.163].

$$0 \leq r < 0.62\sqrt{\left(\frac{l^3}{\lambda}\right)} \tag{2.20}$$

2.3 Transmission Lines

A transmission line guides a signal from the input to the output. RF transmission lines have different architectures for different applications and performances, ranging from simple parallel wire transmission lines, shown in Figure 2.9(a), to Substrate-Integrated Waveguides (SIW), shown in Figure 2.9(b).

Some transmission lines are affected more than others by external electromagnetic fields. For example, a coaxial cable has very high insolation to external interference, given its mechanical construction. At the same time, parallel conductor transmission lines are more prone to interference as both their connectors are exposed.

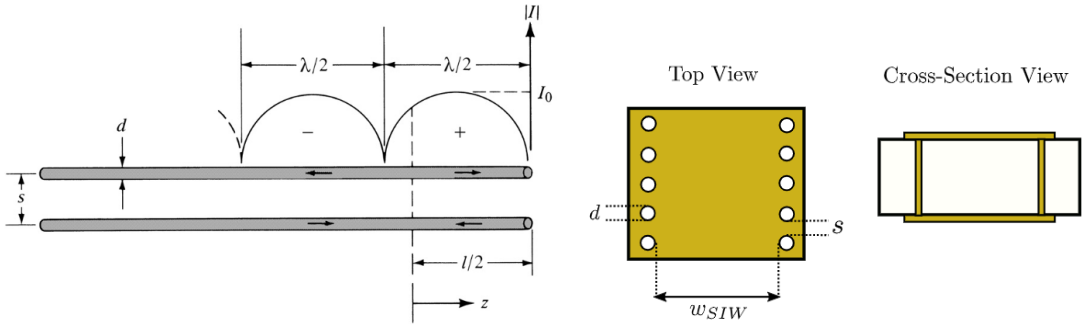

(a) Parallel conductor transmission line [3]. (b) SIW [8].

Figure 2.9: Transmission line examples.

Furthermore, transmission lines can be divided into balanced and unbalanced. On the one hand, a balanced transmission line, by definition has symmetrical currents on the conductors when referenced to ground. On the other hand, an unbalanced transmission line does not follow the specified criteria, which is usually because the conductors used for the return current path is the ground itself. A parallel wire transmission line is an example of a balanced line, while a coplanar waveguide is an unbalanced line. This is relevant because some antennas require a balanced feed line, such as a dipole. If the feed line is unbalanced, a BALUN has to be placed between the transmission line and antenna to ensure proper operation.

2.4 Sumary

In this chapter, an overview of the key concepts needed to understand and developed the work of this dissertation was presented. The fundamental figures of merit related to antenna design were also analyzed, as they will be used to characterize the antennas developed in this work.

Chapter 3

State of the Art

3.1 Anechoic Chamber

An anechoic chamber is a device that provides a space where there is close to zero outside interference and reduced reflections on the inside. Within the scope of electromagnetic anechoic chambers, they can be subdivided into far-field and near-field chambers, although they have the same objective, the construction can be different.

3.1.1 Far-Field Chamber

Within the scope of electromagnetic anechoic chambers, the most common type operates in the far-field. Figure 3.1 illustrates an example of a far-field chamber. Note that in this Figure the absorber material has more depth (the pyramids are higher) towards the center of the chamber. The absorbers in the center are higher not to allow for lower frequency operation, but to better attenuate the signal (reduce reflections) in this critical area. In fact, the wave propagated in this direction only suffers one reflection in the path between antennas (lower attenuation), whereas in other areas, to reach the AUT, the wave would encounter multiple reflections (greater attenuation). The effect is more pronounced when measuring a side lobe of the AUT as the main lobe can be pointed to this critical area of the chamber.

Anechoic chambers for antenna measurements at low frequencies (VHF and UHF bands) are typically made with rectangular and tapered designs [15, p.13]. The main idea is to reduce the reflections that result in the direction of the AUT or the probe antenna while illuminating the AUT with an electric field that is as uniform as possible. Recent work in anechoic chamber design [16], [17] significantly improve chamber performance when compared to conventional rectangular chambers, which is acheived by shaping the chamber walls along with the absorber material, as illustrated by Figure 3.2.

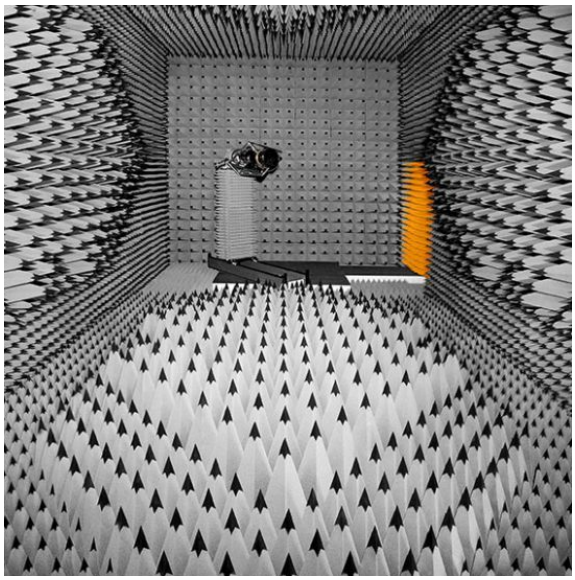

Figure 3.1: Far-field electromagnetic anechoic chamber (rectangular design) [14].

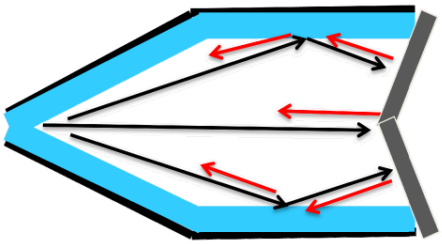

Figure 3.2: Improved far-field electromagnetic anechoic chamber design [16, p.4].

3.1.2 Near-Field Chamber

Near-field chambers are designed to operate in the radiating near-field region of an antenna. In fact, they can also operate in the far-field region, depending on the size of the antenna, the chamber and the frequency of operation as demonstrated by equation (2.19). By opposition, they cannot operate in the reactive near-field, as in this region, the field power is mostly reactive, meaning that the measurement equipment would be interfering with the measurements, rendering the data collected useless. Because the probe antenna can be placed closer to the AUT, considering the same antenna and operating frequency, when compared to a far-field chamber, the whole system becomes more compact. Used in a classical way, the shape of the chamber would be similar to the ones presented in the previous section.

To further improve the advantages of near-field measurements, a three-dimensional measuring system can be used, as illustrated by Figure 3.3. Due to the small form factor of this type of chamber, the use of a 3D measurement technique becomes feasible. The system presented was developed by Microwave Vision Group (MVG) and allows for the measurement of 3D radiation patterns, gain, sidelobe levels, among other parameters. Even though the measurements are taken

in the near-field region the results are presented in the far-field, which is achieved with the use of near to far-field conversion algorithm.

Figure 3.3: Near-field electromagnetic anechoic chamber [18].

Other solutions for three-dimensional near-field measurements do exist, like the one presented in [19] which implemented a hand-held probe for the same purpose but with intended use in an open space. Even though the measurement error in this system is more significant, when compared to a traditional approach, it presents a smaller and simpler, yet effective solution for fast antenna validation in the field, which can be advantageous.

3.2 Probing System

Traditional anechoic chambers use a single probe at the far end of the chamber. Figure 3.1 shows the point of view of the probe at the end of the chamber, as such, the AUT and positioner are visible at the other end. In this system, a VNA is connected to both the AUT and the probe directly, usually using coaxial cables. The VNA can either send an RF signal via the AUT to be received by the probe or vice versa, this will depend on the AUT and the probe used, as they may not be reciprocal. To plot the radiation pattern of the AUT using this approach, it would have to be rotated horizontally by a given amount for every vertical rotation, which normally is never done due to the time it takes to cover the entire space around the AUT, with sufficient precision to validate the radiation pattern.

Another solution is to surround the AUT with probes, at a fixed distance from the antenna and uniformly distributed on a circle centered in the AUT, multiplexed electronically. In this case, the measurement time would be greatly reduced, as the AUT would only need to move in one plane and the switching action is faster than the rotation. It is considered that the number of sampling points is equal to the number of probes so that the resolution remains the same. To achieve this in a far-field chamber the radius of the circle described by the probing system would be equal to the length of a standard far-field chamber, which would result in a very large space when compared to

the standard solution. The same approach can be taken for near-field chambers, but in this case, as the near-field boundary is approximately $3.23\sqrt{l/\lambda}$ times closer to the antenna when compared to the far-field boundary (considering the boundaries defined in equation (2.19)), it allows for a much more compact design. A more detailed analysis regarding the radius of the chamber is performed in section 7.2. To maintain the alignment needed for antennas that use linear polarization the probes would either need to be rotated according to the rotation of the AUT or support dual-polarization (vertical and horizontal). With dual polarization, we can achieve the same result by collecting and storing the measurement of each perpendicular polarization and joining them in post-processing. Furthermore, when using near-field techniques a dual polarization probe is already required by the near-to-far-field conversion algorithms [3, p.997].

Probe antennas should also be broadband to allow for different AUT that operate at different frequencies without needing to change the probe.

3.3 RF Switches

In RF circuits, sometimes, the signal is required to go through different paths, meaning that the signal can come from more than one source and go to more than one receiver, and for this purpose switches are used. These circuits are designated switching matrices, which allow any input to connect to any output. In the more complex circuits, each input can connect to more than one output simultaneously.

There is more than one type of RF switch, as described in the following subsections. The RF switching circuit, in this application, creates a path from each probe polarization to the VNA. To fulfill this task, multiple solutions are possible with different complexities and scalability capabilities.

3.3.1 Mechanical

Mechanical (usually electromechanical) RF switches, as the name implies have moving parts that are actuated to switch the signal from one port to the other, or simply to connect and disconnect a transmission line. Moving parts imply slower switching times when compared to solid-state solutions, with switching times reaching dozens of milliseconds. Within this type of switch, there are different architectures such as the electromechanical relay, shown in Figure 3.4(a) and the Micro Electronic Mechanical Systems (MEMS) which are microscopic mechanical structures embedded into an integrated circuit, as shown in Figure 3.4(b).

One other type of RF switch uses a cut waveguide to close or open the transmission line. Even though they are more limited in bandwidth due to the waveguide characteristics, these types of switches can usually carry more power than their counterparts. Moreover, these devices tend to be much larger and slower when compared to the previous solutions. Figure 3.5 illustrates an example of a waveguide RF switch.

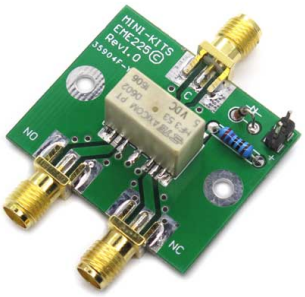

(a) Relay [20].

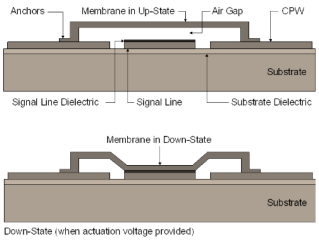

(b) MEMS structure [21].

Figure 3.4: Mechanical RF switches.

Figure 3.5: Waveguide RF switch [22].

3.3.2 Semiconductor

Semiconductor RF switches are divided into two subfamilies: diodes-based and Field Effect Transistor-based (FET). As expected, their behavior and the way they are activated are different. The main difference between FETs and diodes is that diodes are two-terminal devices while FETs are three-terminal devices.

Diode-based switches require a current bias to enable them, as illustrated by the Single Pole Double Throw (SPDT) circuit in Figure 3.6. Enabling the switch (allowing the signal to pass from the input to the output) requires current to flow through the diode in the forward direction, allowing the signal to pass through it. Essentially the RF signal modulates the current passing through the diode. Assuming that the current variation does not cause the forward current to reach zero, the signal is passed from the input to the output with no distortion. Because of this biasing current, the circuit will draw power from the source while it is on, which is undesirable. On the off state, the diode should be reversed polarized so that the diode's depletion zone gets extended, reducing the capacitance between the contacts.

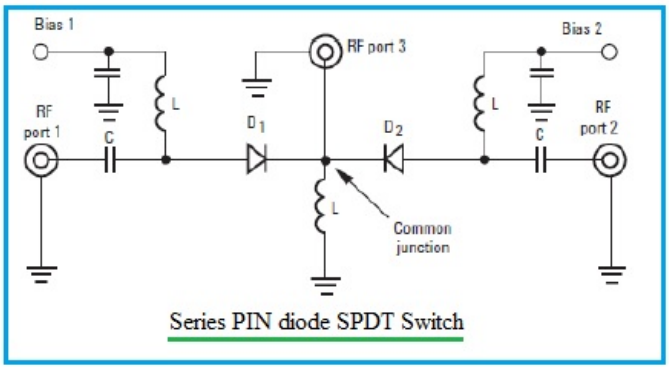

Figure 3.6: Diode based RF switch [23].

Positive Intrinsic Negative (PIN) diodes are used in this application because their off-state capacitance is smaller than standard Positive Negative (PN) junction diodes. As previously stated, a smaller capacitance provides a greater impedance in the path of the RF signal, which is desired in the off state.

FET-based RF switches use transistors to switch the signal. Since these devices have a high impedance on their gate (considering Direct Current (DC)), the on-state and the off-state current will be close to zero (there is always some parasitic draw present). Figure 3.7 shows a possible transistor-based SPDT RF switch. Furthermore, these circuits may operate down to DC levels, even though some designs use Alternating Current (AC) coupling in the RF path, depending on the manufacturer.

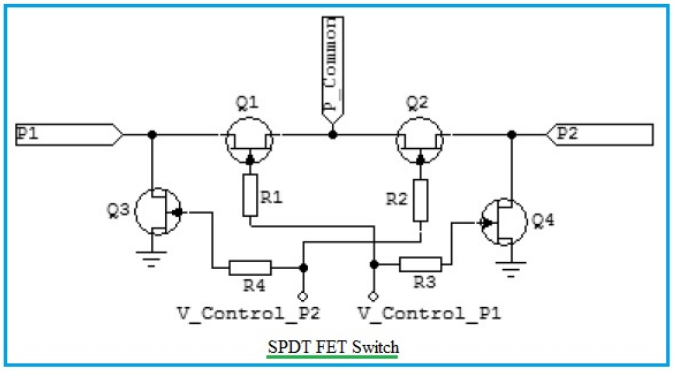

Figure 3.7: Transistor based RF switch [23].

3.4 Positioning System

The positioning system is responsible for moving the antenna with a specified level of accuracy to a given angle. In this situation, the positioning system only needs to orient the antenna in a plane, which means that it can be a simple platform, like the one illustrated in Figure 3.8. Nevertheless, the phase center of the antenna should be positioned at the center of rotation of the positioner, so that a phase measurement does not get affected by the rotation of the AUT.

Figure 3.8: Horizontal plane positioner [18].

Furthermore, the positioner would have to be strong enough to support the weight of the AUT, but at the same time be transparent to radio waves. This is because the positioner is located in the reactive near-field of the antenna, as such, any material will affect the antenna, some more than others, depending on the electric and magnetic characteristics of the material. The ideal material would have to be mechanically robust and have the same electric permittivity, ε, and magnetic permeability, μ of air.

3.5 Absorbers

Absorbers are designed, as the name implies, to absorb a radio wave that reaches them. They are used to cover the internal surfaces of an anechoic chamber to attenuate reflections that invalidate the measurements. There are several types of absorbers, varying in shape and materials, designed for different applications. The main types are called pyramidal, wedge and tile, being based on a range of possible materials, polyurethane (the most common ones), polypropylene and ferrite. In all cases, the energy absorbed is dissipated as heat, this is why absorbers have a limited power absorption capability, usually given in $\mathrm{W\,m^{-2}}$.

All the measurements for reflectivity, presented in this section, used an incident wave that is normal to the absorber.

3.5.1 Tiles

A tile absorber is a simple rectangle as illustrated by Figure 3.9. Table 3.1 lists the frequency limits of operation and respective reflectivity for tile absorbers according to Diamond Microwave Chambers (DMC) manufacturer [24].

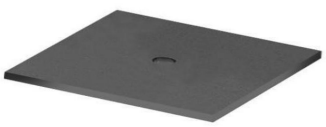

Figure 3.9: Ferrite tile absorber [24].

Table 3.1: Tile absorber characteristics.

Material	Frequency range (GHz)	Reflectivity (dB)	Height (mm)
Ferrite	0.03 to 1	-25.5 to -10	6.7
Polypropylene	1 to 40	-15 to -34	40
Polypropylene	1 to 40	-21 to -39	100
Polyurethane	1 to 40	-10 to -22	50

It is possible to see why ferrite tiles are not suited for the intended application as they become more reflective (lower attenuation on the reflected wave) with the increase in frequency. Furthermore, they have a small bandwidth when compared to the other solutions available.

3.5.2 Wedge

DMC offers a range of wedge absorbers in polyurethane, as illustrated by Figure 3.10, with varying heights. Compared to tiles, these absorbers are not only taller but offer better reflectivity and higher bandwidth, meaning that the reflected wave is more attenuated over a bigger span of frequencies. On the flip side, more height means a bigger anechoic chamber to maintain the distance between the highest surface of the absorber and the AUT. Table 3.2 lists the frequency limits of operation and respective reflectivity for wedge absorbers supplied by DMC.

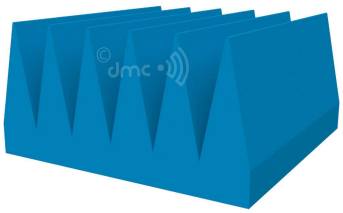

Figure 3.10: Polyurethane wedge absorber [24].

Table 3.2: Wedge absorber characteristics.

Material	Frequency range (GHz)	Reflectivity (dB)	Height (mm)
Polyurethane	1 to 110	-25 to -45	200
Polyurethane	1 to 110	-30 to -45	300
Polyurethane	0.5 to 110	-20 to -45	500
Polyurethane	0.5 to 110	-25 to -45	700

3.5.3 Pyramid

Pyramidal absorbers are typically manufactured in polyurethane or polypropylene. Figure 3.11 illustrates a polypropylene pyramidal absorber and Table 3.3 lists the frequency limits of operation

and respective reflectivity for pyramidal absorbers supplied by DMC. In terms of physical dimensions, these absorbers are very similar to the wedge absorbers but have a better impedance gradient when compared to the wedge. This is because there is less material at the tips of the pyramids and more at the base. When a wave reaches the absorber the impedance is close to the impedance of the air ($\approx 377\,\Omega$) then as it propagates deeper into the absorber the impedance decreases approaching the impedance of the absorber (η_A) [25, p.6], given by equation (3.1). Considering that the material is non-magnetic $\mu = \mu_0$ (not the case for ferrite tiles) where ε_r is the electric permittivity of the absorber material. It is important to note that the electric permittivity of the absorber material is complex, as such, it has an associated loss tangent, $\tan(\delta)$. Both electric permittivity and loss tangent can be determined experimentally as described by [26], in case they are not provided by the manufacturer.

$$\eta_A = \sqrt{\frac{\mu_0}{\varepsilon_0 \varepsilon_r}} \approx \frac{377}{\sqrt{\varepsilon_r}} \tag{3.1}$$

Figure 3.11: Polypropylene pyramidal absorber [24].

Table 3.3: Pyramidal absorber characteristics.

Material	Frequency range (GHz)	Reflectivity (-dB)	Height (mm)
Polypropylene	0.03 to 40	-18 to -32	200
Polypropylene	0.03 to 40	-20 to -35	300
Polypropylene	0.03 to 40	-21 to -42	500
Polyurethane	6 to 110	-30 to -45	50
Polyurethane	1 to 110	-27 to -48	100
Polyurethane	0.5 to 110	-25 to -47	200
Polyurethane	0.3 to 110	-20 to -48	500

3.5.4 Comparison

Considering that the chamber design is cylindrical, a mechanically flexible absorber material is desired, ruling out the ferrite tiles and polypropylene. This leaves polyurethane pyramids, wedges and tiles, due to the geometry of the chamber the wave will always be normal to the absorber, meaning that the performance of the first two would be very similar and superior to the tiles. Given

the fact that pyramidal absorbers have a higher frequency range of operation and lower reflectivity (better attenuation), they would be more adequate for the purpose. Another consideration to be taken is the height of the pyramid, in this case, the higher the better in terms of attenuation of the reflected wave but there is a trade-off with the size of the chamber, a higher pyramid implies a larger chamber.

3.6 Sumary

In this chapter, a study of the existing anechoic chamber technology was performed. The study also included the building blocks of the system to be developed, such as the probing and positioning systems. An analysis of the available RF switching circuits technology was also performed. The mechanical components were also analyzed, including the chamber structure and absorber design and materials.

Chapter 4

RF Switching

4.1 Introduction

As already mentioned, switching is often required in RF circuits. In this case, it is required to forward the signal received by each probe polarization to the VNA.

In this chapter, the design process of the RF switching network is presented, starting by analyzing possible switching circuit architectures. Followed by the PCB design of the selected circuit, simulation, and experimental tests.

4.2 Circuit Architecture

4.2.1 Cascaded Circuit

On a cascaded architecture, the switches are arranged in levels where the signal propagates from the previous level to the next, reducing the number of devices on each level as the signal approaches the output port, as illustrated by Figure 4.1.

Furthermore, switches come with a different number of ports. For example, switches with single output and dual input (SPDT), single output and triple input (SPTT), among others. On the one hand, the more inputs a switch has, the more expensive it gets. On the other hand, fewer switching stages are required, so there is less attenuation of the signal. A relation can be established between the number of inputs to the number of stages of the switching circuit, given by equation (4.1), where S_{ges} is the number of switching stages, I is the number of inputs of a switch (for an SPDT, there are two inputs and one output), and N is the number of total inputs to the circuit. In this case, N equals twice the number of probes, as each probe has two outputs, one for each polarization. Equation (4.1) assumes that the switches used are all equal.

$$S_{\text{ges}} = \log_I(N) \tag{4.1}$$

The main advantage of using this design is that the attenuation of each input is the same. In reality, the attenuation can vary as the transmission lines connecting the different stages can have

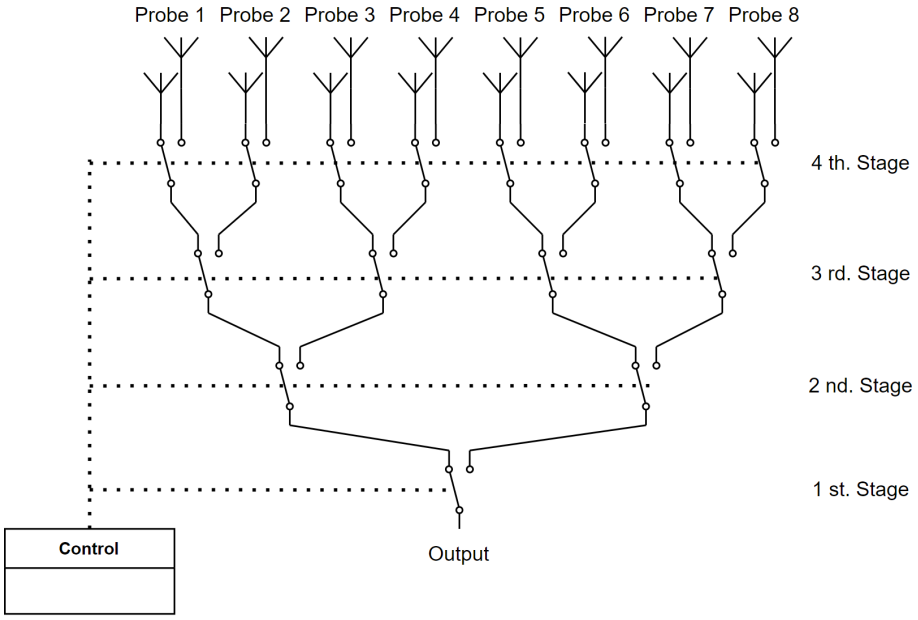

Figure 4.1: Cascaded switching circuit using SPDT switches.

different lengths. Furthermore, the attenuation of the switching circuit is reduced when compared to other solutions (like the one analyzed in section 4.2.2) as the number of switches connected in series depends on a log operation, as defined by equation (4.1).

There are two main disadvantages to this design. The first one is that it requires two cables per probe, which would cause cable management problems and could get expensive depending on the length of cable used. The second one is scalability. Increasing or decreasing the number of outputs would require a new PCB design. Of course, one can design a PCB to include more outputs than needed and then leave the inputs open or terminate them with a load, but this would increase production costs.

4.2.2 Series Circuit

In a series switching circuit, the probes are connected in series, meaning that one probe connects to the next, and so on, and the last probe connects to the VNA. In this case, only two switch types make sense: SPDT and SPTT, given that there are two polarizations per probe and one connection that comes from the previous probe.

The main advantage of using this architecture is that it is very easily scalable. However, the switch and cable attenuation limit it to a maximum number of probes.

The main disadvantage of this circuit is the different attenuation suffered by each probe. Considering the same attenuation in each switch, the first probe (the one further away from the VNA) will have the most attenuation. In other words, a calibration for each probe would be required. Assuming that the circuit remains unchanged while the measurements are being taken, one just needs to allocate sufficient space for the calibration data in post-processing. The problem lies in the loss of signal quality throughout the chain. In other words, the Signal to Noise Ratio (SNR)

decreases due to signal attenuation. To counteract this effect, an LNA can be placed right after the antenna connection to allow for a larger SNR at the beginning of the chain, and then some LNAs can be placed in the signal path to reamplify the signal. However, there is a limit to the number of amplifiers that can be placed, this is because the signal is not reconstructed, as such, the SNR will continue to decay. The most crucial amplifier in the chain is the first, as it is this one that most affect the system noise figure F_{sys} ($F_{\text{sys}} = 10\log(f_{\text{sys}})$) as demonstrated by equation (4.2) [27, p.8], where f_n is the noise factor of the device at position n, and G_n the gain at position n in the amplification chain. Note that the gain can be smaller than one, meaning the device attenuates the signal. For example, it could represent a transmission line.

$$f_{\text{sys}} = f_1 + \frac{f_2 - 1}{G_1} + \frac{f_3 - 1}{G_1 G_2} + \frac{f_4 - 1}{G_1 G_2 G_3} + \cdots + \frac{f_n - 1}{G_1 G_2 \ldots G_{n-1}} \tag{4.2}$$

4.3 Implemented Design

Based on the analysis performed in the previous sections, a series switching circuit was chosen due to its scalability. Nevertheless, cost, availability, and Integrated Circuit (IC) packaging are still significant when choosing electronic components. For the intended range of frequencies (1 to 30 GHz), encapsulated SPTT switches were not available, for this reason, they were ruled out. The solution was to use SPDT switches, which were readily available.

Once again, a compromise must be made between switch performance, and the complexity of the driver circuit required (ideally embedded in the device). Based on the options available at the time, the MASW-011102-TR0500 was chosen, which provides acceptable attenuation (insertion loss), a fair price when compared to the other available switches, and an easy way to control it (with -5 to 0 V logic).

To compensate for the attenuation of the switches, the MAAM-011109-TR1000 LNA was selected. After some research, this LNA was selected due to its operating frequency range, simple circuit integration and because it maintains a matched input even when disabled, which allowed it to be switched off when not in use, reducing the current required to power the system. A more detailed analysis of this device is performed in Appendix A.

4.4 PCB Design

When designing a PCB for an RF circuit extra variables become significant. Namely, the substrate material and height, what type of transmission line is used, and what connectors. The main concern when choosing a material is its loss at high frequencies, in this case, at the highest operating frequency, 30 GHz. Considering different substrates and their availability in the manufacturer, the choice was made to use RO4350 with 0.254 mm of thickness. The height of the substrate directly influences the impedance of a transmission line. Having considered different transmission lines, the Coplanar Waveguide with Ground plane (CPWG) was selected for the switching circuit.

Because the antenna used in the probe is small, any extra radiation originating from the transmission line can affect its operation. As a rule of thumb, to reduce the transmission line radiation, the track width was kept smaller than a tenth of the wavelength at the maximum operating frequency. To better understand how much a CPWG transmission line radiates with different widths, an analysis was performed in Appendix B. Because the wavelength depends on the characteristics of the propagation media, the actual relative permittivity must be computed. To design the transmission line to 50 Ω (standard line impedance), four parameters are required, the height of the substrate h (0.254 mm), the electric permittivity in vacuum $\varepsilon_0 = 8.854^{-12}\ \mathrm{Fm}^{-1}$ and the relative electric permittivity ε_r (from the material datasheet $\varepsilon_r = 3.66$), the line width S and the isolation to the coplanar ground W, as illustrated in Figure 4.2.

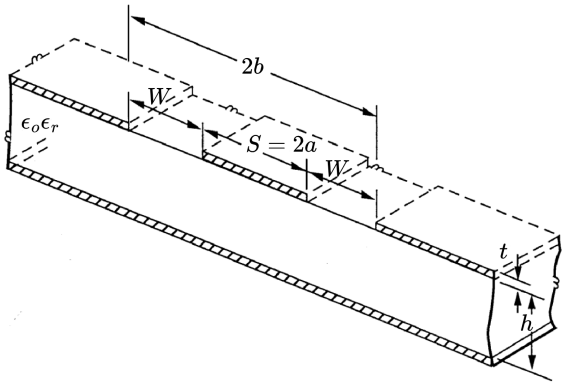

Figure 4.2: CPWG line model [28, p.88].

To design this transmission line to match the desired impedance, some intermediate variables are required, as described by equations (4.3), (4.4), (4.5) and (4.6) [28, p.89].

$$k = \frac{a}{b} \tag{4.3}$$

$$k_3 = \frac{\tanh\left(\frac{\pi a}{2h}\right)}{\tanh\left(\frac{\pi b}{2h}\right)} \tag{4.4}$$

$$k' = \sqrt{1-k^2} \tag{4.5}$$

$$k'_3 = \sqrt{1-k_3^2} \tag{4.6}$$

Then, with equations (4.7), (4.8), the effective electric permittivity and impedance can be computed, respectively [28, p.89], where $K(k)$ is the complete elliptic integral of the first kind with modulus k.

$$\varepsilon_{\mathrm{eff}} = \frac{1+\varepsilon_r \frac{K(k)}{K(k')}\frac{K(k_3)}{K(k'_3)}}{1+\frac{K(k)}{K(k')}\frac{K(k_3)}{K(k'_3)}} \tag{4.7}$$

$$Z_0 = \frac{60\pi}{\sqrt{\varepsilon_{\text{eff}}}} \frac{1}{\frac{K(k)}{K(k')} + \frac{K(k_3)}{K(k_3')}} \tag{4.8}$$

By setting the value of the relative electric permittivity to $\varepsilon_r = 3.66$, the height of the substrate to $h = 0.254\,\text{mm}$, and $W = 0.2\,\text{mm}$, S was adjusted until the line impedance matched $50\,\Omega$. The obtained value for S was $0.5\,\text{mm}$, corresponding to a line impedance of $50.3\,\Omega$ and a effective electric permittivity $\varepsilon_{\text{eff}} \approx 2.7$. Considering the computed ε_{eff}, the wavelength in the transmission line is $\sqrt{2.7}$ times larger when compared to propagation in a vacuum. With a wavelength of approximately $6.1\,\text{mm}$ at $30\,\text{GHz}$ the transmission line should be smaller than $0.61\,\text{mm}$, which it is. With the computed transmission line dimensions, the PCB was designed. Note that to emulate the simulated ground block (used to reduce simulation complexity) via stitching was used with a separation of $\lambda/10$ (considering the wavelength on the transmission line) on the sections of higher currents, *i.e.* close to the transmission lines, and a separation of $\lambda/5$ on the rest of the PCB.

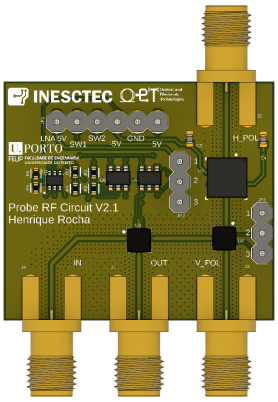

Figure 4.3: RF switching circuit 3D model.

The circuit presented in Figure 4.3 serves as a test board, allowing for the validation of the switch control logic and the LNA response in the frequency range. In this design, only one LNA is present to reduce costs in the production of the test board. Furthermore, when included in the probe design, the LNA for the other polarization (vertical) is placed in the other PCB, this is done to ensure that the signal path between the probe and the LNA remains as short as possible to reduce signal degradation.

As one may notice on the PCB there are three jumpers on each side of the transmission line that connects the output of the LNA (the biggest IC on the PCB) to the input of the RF switch on the far right, beside the bottom jumpers. These jumpers were placed so that the positive supply of the LNA and the two control connections to the switch did not have to be routed under the transmission line. As the electric field is present between the line and the ground, placing a control line where it is supposed to be ground causes undesired effects, which were simulated.

4.5 Design Validation

To validate the design, an electromagnetic co-simulation was performed using ADS Momentum. The Open Database ++ (OBD++) files, which contain the PCB layout and stackup information, were imported to ADS and calibrated ports were inserted in the edges of the transmission lines. The calibration of a port is intended to include or ignore, depending on the type used, certain effects at the start of the transmission line, such as fringing fields or other parasitic behaviors already included in the component's S parameters supplied by the manufacturer. A simulation was performed for each signal path possible *i.e.* from all inputs to the output. Then for each path, a symbol was created to be imported to a schematic that joins all the circuit components, including the S parameters supplied by the manufacturer. The resulting schematic for the path horizontal polarization to the output is represented in Figure 4.4. In the following simulations, the effect of the probe was not considered, as the intent was to validate the correct operation of the switching circuit.

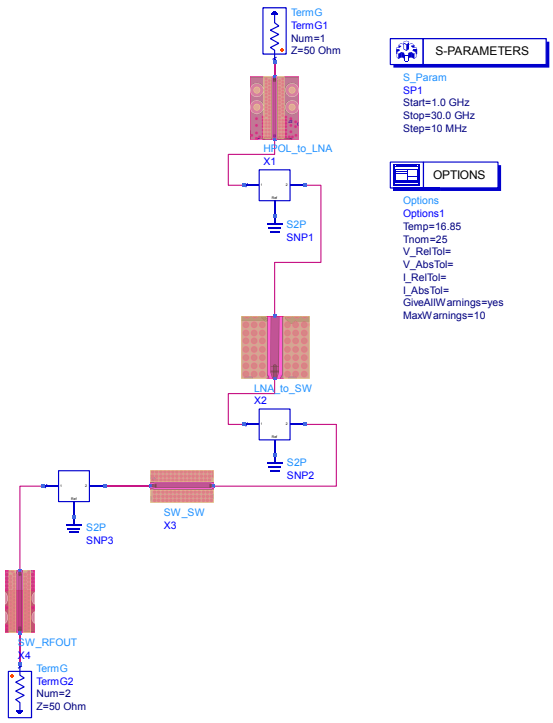

Figure 4.4: Co-simulation schematic for the horizontal polarization to output signal path.

4.5.1 RF Input to Output

Starting with the simplest path, having only one switch, allows us to better understand the results of the more complex signal paths. The path from the previous probe input connector (connector on the far left of Figure 4.3) to the output (center connector in the same Figure) is a

critical one. The attenuation in this path has to be as small as possible as it is cumulative throughout the series connection, meaning that the total attenuation is directly proportional to the number of probes used as explained in section 4.2.2. The simulation results for this path are shown in Figure 4.5.

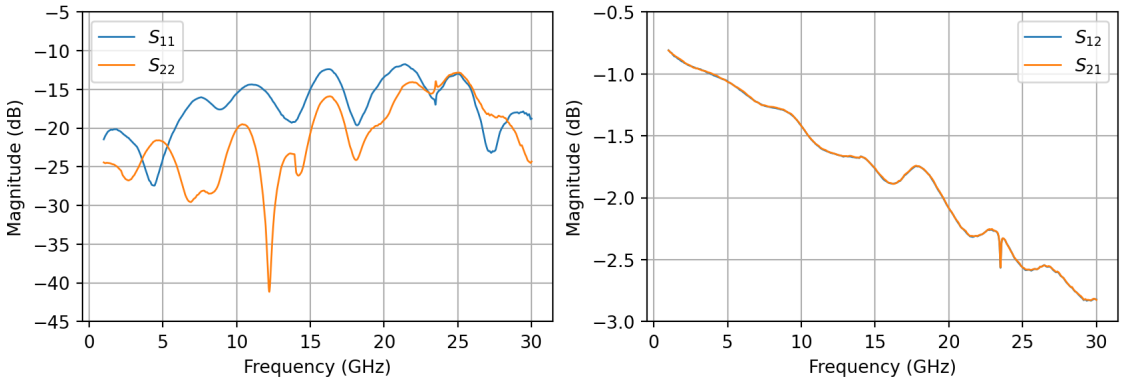

Figure 4.5: Simulated S parameters from RF input to output.

From the results, we can observe that the attenuation, which in most part is due to the switch (about 2.8 dB at 30 GHz), is considerably high. This is undesired as it limits the maximum number of probes that can be used. For example, if just ten probes were used the signal from the first antenna in the chain would have an attenuation of about 28 dB, just in the switching circuit, not considering the cables that connect the probes between each other. This is a design limitation.

4.5.2 Vertical Polarization to Output

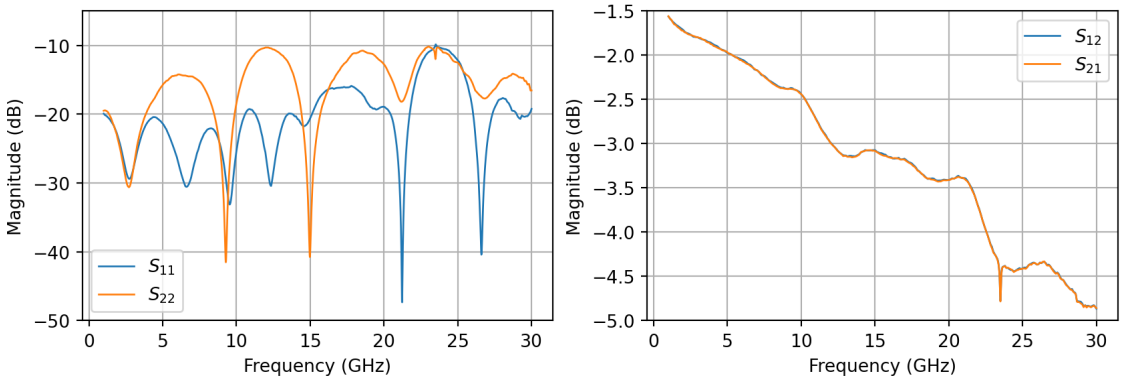

Figure 4.6: Simulated S parameters from vertical polarization to output.

Considering the simulation results for the signal path from the vertical polarization connector (Figure 4.3 bottom right) to the output (bottom center connector on the same Figure) shown in Figure 4.6, one can see that the circuit is matched and that the maximum attenuation of this path is about 4.8 dB. A part of this loss comes from the transmission lines, about 1.2 dB (computed on a different simulation), and the rest is divided by the two RF switches as they are equal. Adding

up to 1.8 dB per switch, which agrees with the value obtained in section 4.5.1, considering a transmission line attenuation of 1 dB.

4.5.3 Horizontal Polarization to Output

This last signal path includes all the active devices used. The simulation results for this path are shown in Figure 4.7.

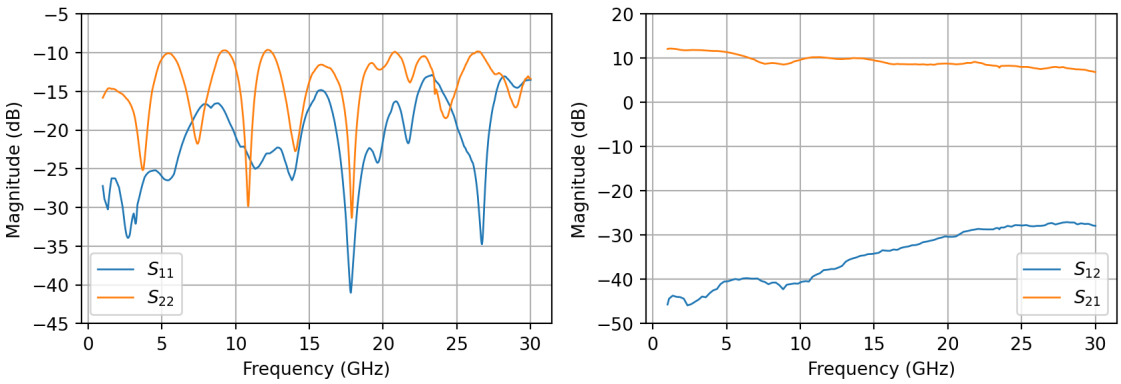

Figure 4.7: Simulated S parameters from horizontal polarization to output.

The simulation results show that the return loss in both the input and the output (S(1,1) and S(2,2)) are below -10 dB for the majority of the frequencies plotted. In certain frequencies, the return loss of the output is at most 1 dB above the -10 dB design goal, but it is still acceptable. In fact, the return loss on the input will not be as low as the results show, this is because the input impedance of the probe will vary with frequency. A 50 Ω input impedance for such a large bandwidth (at these frequencies) is hard to achieve. In that case, the noise figure of the probe and switching circuit would be of interest to characterize, as it directly influences the system's SNR, and consequently the quality of the measurements performed. To compute the noise figure of the probe and switching circuit, the port impedance (at the input of the LNA) would be replaced by the simulated probe impedance. However, this study was not performed as the model of the LNA and switches, provided by the manufacturer did not include noise parameters, which are required to compute the noise figure. Regarding the transmission parameters, on the one hand, the isolation provided from the output to the input, as expected, is high, in this case, above 25 dB. On the other hand, the gain from the input to the output follows the gain of the amplifier minus the attenuation of both switches and the transmission lines. A more detailed analysis of the LNA is performed in Appendix A.

4.6 Experimental Tests

4.6.1 PCB Assembly

Prior to testing the developed switching circuit, the components first need to be soldered to the PCB. This process was done in-house using solder paste and stencil, followed by reflow using a hot plate. The decision to solder the components in-house proved to be a mistake, as demonstrated by the results presented in subsection 4.6.2.

The first step was to solder the surface mount components as described above, and then the through-hole components were soldered. The fully assembled PCB is illustrated in Figure 4.8.

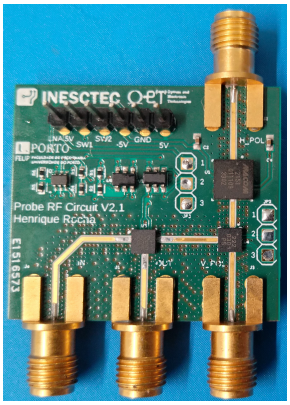

Figure 4.8: RF switching circuit PCB.

4.6.2 Measurements

With the assembled circuit, the measurements performed in the simulation were repeated using a VNA. These measurements were intended to confirm that the LNA and the switches were operating correctly. The RF switches are accompanied by an external digital driving circuit. A detailed description of this circuit is done in section 5.2. In fact, before manufacturing the RF switching circuit PCB the digital circuit operation had already been validated.

The first step in the measurement process is to perform a port calibration to remove the effect of the coaxial cables used to connector the circuit to the VNA. The calibration kit available at the time was the 85052D from Keysight. Note that the kit is only capable of operating up to 26.5 GHz, which is a limitation imposed by the maximum operating frequency of the SMA (or 3.5mm) connectors it uses. As such, the measurements were only performed up to the kit's maximum operating frequency. The following subsection describes the measurement process for each signal path, *i.e.* RF input to output, vertical polarization to output, and horizontal polarization to output. During the measurement process, the RF power was reduced to -10 dBm so that neither the VNA nor the LNA could be damaged. The measurement setup used is shown in Figure 4.9, where port one is connected to the input of the LNA and port two is connected to the output of the switch.

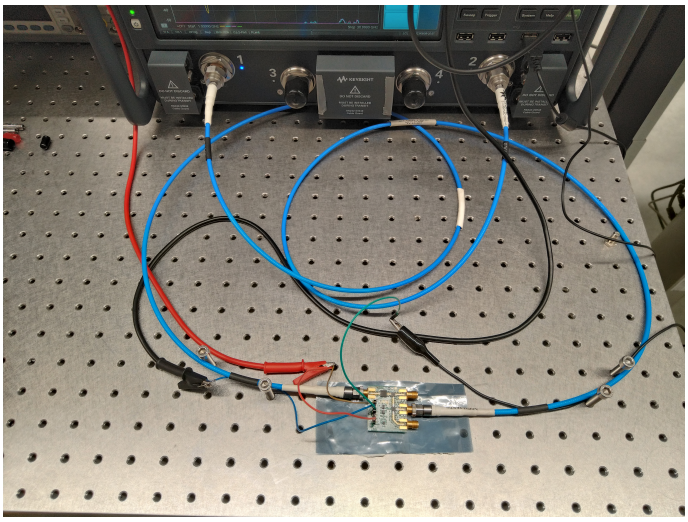

Figure 4.9: Horizontal polarization to output measurement setup.

4.6.2.1 RF Input to Output

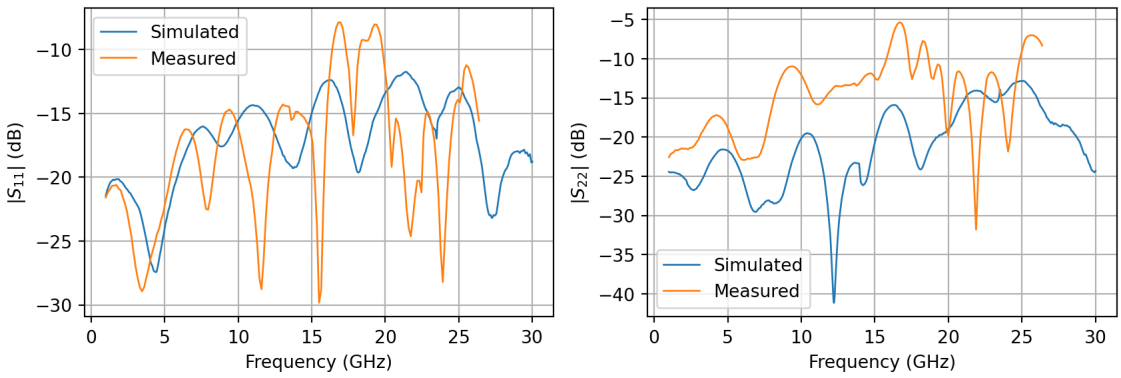

(a) Reflection.

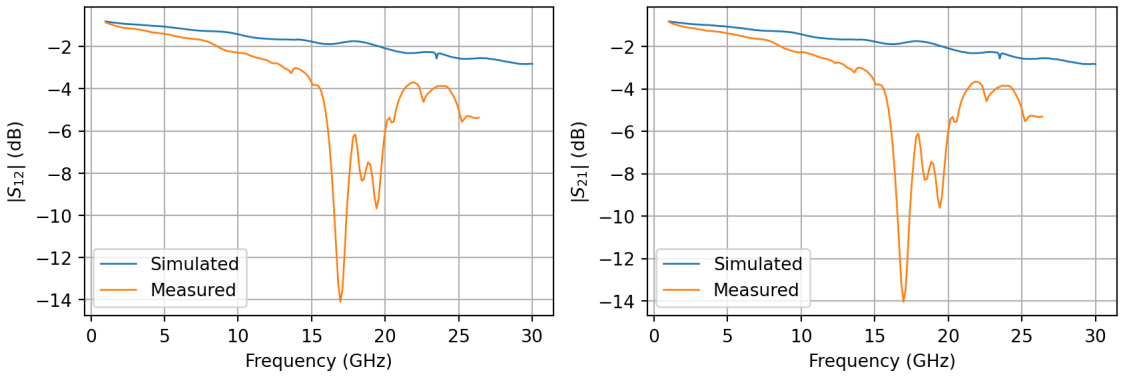

(b) Transmission.

Figure 4.10: RF input to output simulated and measured S parameters.

To measure this signal path, port one of the VNA was connected to the RF input, and port two to the output. The switches were then latched to the proper position and the LNA remained disabled. The measured S parameters are shown in Figure 4.10.

From the presented plots, it is possible to see that for lower frequencies, the measured and simulated results agree, but quickly start to diverge from one another. The behavior is typical of poorly soldered components. As such, future work should include new measurements with professionally soldered components. Given that this switch is used in the other signal path it is expected that the observed results diverge further from the simulation. Although bad results are expected, the measurements were still performed to verify the circuit operation.

4.6.2.2 Vertical Polarization to Output

After the measurements of the last signal path were completed, the vertical polarization signal path was measured. The measurement setup remained the same, with only one connection swapped. Port one was now connected to the vertical polarization input. The measured S parameters are shown in Figure 4.11.

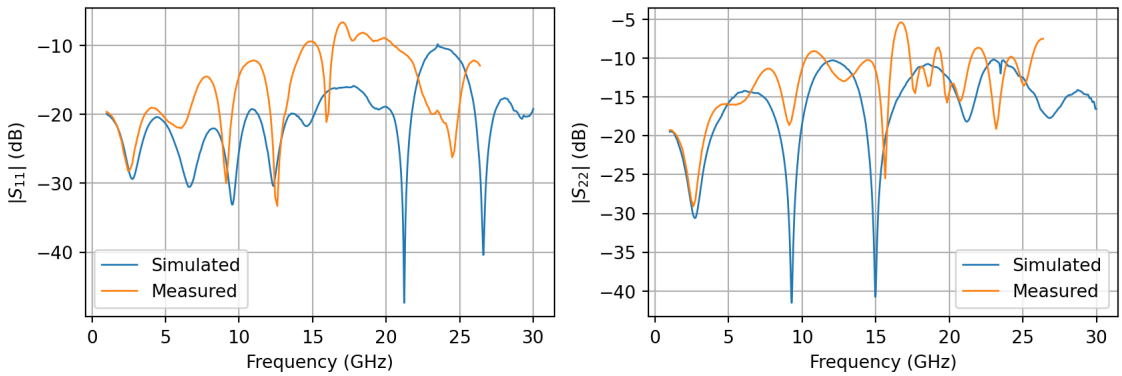

(a) Reflection.

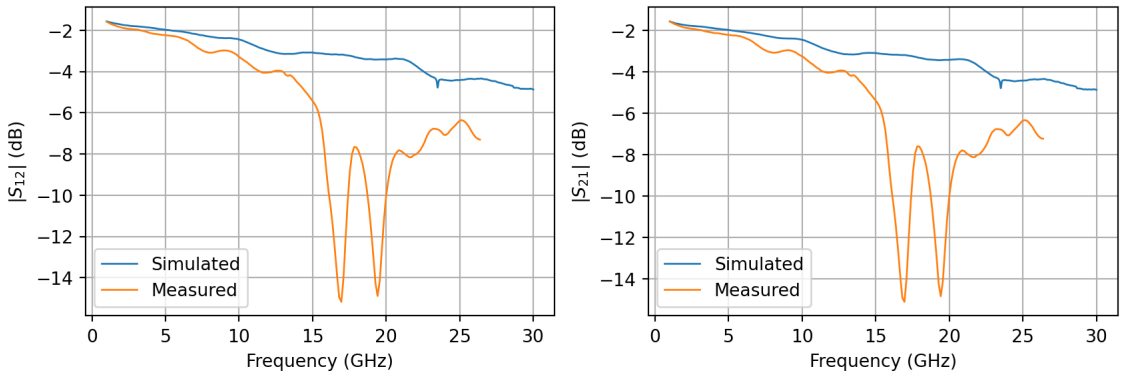

(b) Transmission.

Figure 4.11: Vertical polarization to output simulated and measured S parameters.

The obtained results are similar to the last measurement, which indicates that both switches are poorly soldered. In Figure 4.10(b), we can observe that the insertion loss around 17 GHz is close to 14 dB while in Figure 4.11(b) it increases to 15 dB, which means that the second switch at this frequency is operating as intended. However, closer to 19 GHz we can observe a significant increase in insertion loss when the second switch is in use. In other words, the second switch is also poorly soldered, only differing on the most affected frequency. Nonetheless, it is possible to see that, for the lower end of the spectrum, the attenuation has doubled, which is expected as there are now two switches in the signal path.

4.6.2.3 Horizontal Polarization to Output

For this signal path, the LNA was enabled by first applying the ground and negative rail and then powering the positive rail. After powering on the LNA, the switches were latched to complete the signal path from the horizontal polarization (LNA input) to the RF output. The measured S parameters are shown in Figure 4.12.

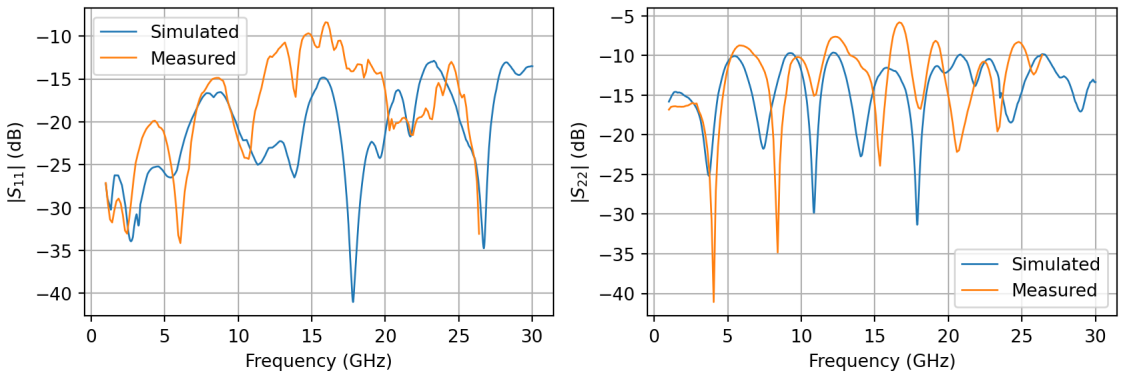

(a) Reflection.

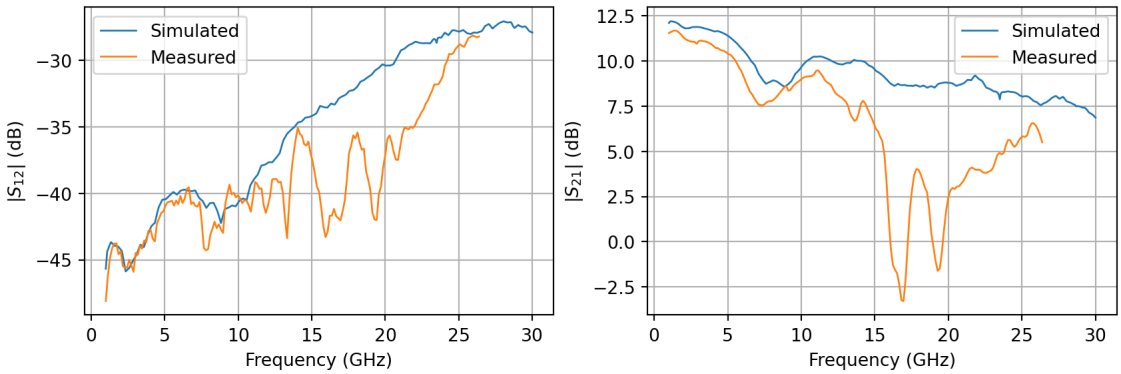

(b) Transmission.

Figure 4.12: Horizontal polarization to output simulated and measured S parameters.

Similarly to the last measurements, the lower end of the spectrum is consistent with the simulated model, which indicates that the control circuit and DC operating point are correct. Neverthe-

less, we can observe that all the components appear to be poorly soldered, which is observed in a more detailed analysis of the LNA performed in appendix A.

4.7 Sumary

In this chapter, the development of the RF switching circuit is presented. First, two different switching architectures were analyzed, resulting in the selection of a series architecture. After the selection of the components, the PCB layout was designed and then simulated to ensure that it was working as intended. In the end, the manufactured switching circuit was measured experimentally.

After the experimental tests, it was concluded that the components were not soldered correctly. Therefore, future work should include the measurements of the designed circuit with the components properly soldered, so that the design can be fully tested and validated.

Chapter 5

Control Circuitry

5.1 Introduction

In this chapter, the design process of the control system of the near-field chamber is presented. The first circuit presented is the one used to drive the RF switching circuit, followed by the custom breakout board, the positioner and LASER controller, and the power supply. In the end, the circuits are validated experimentally.

5.2 RF Switching Circuit Driver

With the switching circuit components selected, we now require a circuit to control them. The goal is to have a microcontroller in each probe that takes care of the control and communication. Having a microcontroller in each probe greatly reduces the connections required to control them, as serial communication protocols can be employed. Considering the already implemented communication protocols, I^2C was chosen because it only requires two wires for communication.

With the communication protocol defined, a suitable microcontroller needs to be selected. For this purpose, the Attiny84 from Atmel was selected. Three of the GPIO pins available were used to drive an RGB LED to indicate the state of the switching circuit.

To control the RF circuit, two GPIOs were used to enable the LNAs for the vertical and horizontal polarizations. These are important because the device requires a power-up sequence, which is ensured by the use of PMOS transistors with pull-up resistors.

Regarding the RF switches, the input logic levels specified in the datasheet are -5 and $0\,\mathrm{V}$, which means that the standard 0 to $5\,\mathrm{V}$ logic levels of the microcontroller need to be converted. To convert the logic levels, a simple circuit depicted by Figure 5.1 was used.

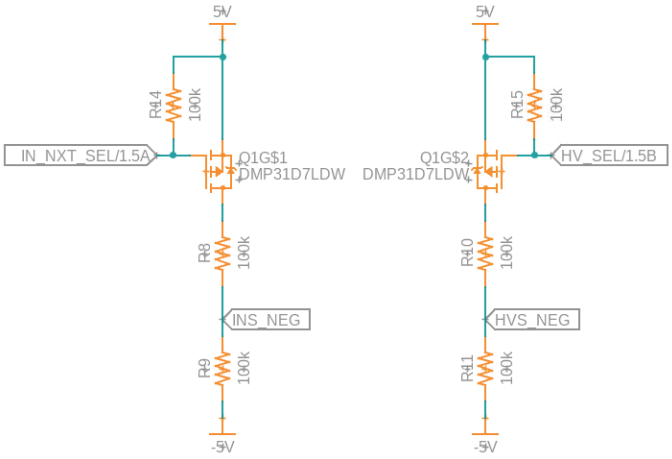

Figure 5.1: Logic level shifters.

In this circuit, a resistor divider controlled by a PMOS transistor is used to convert the 0 to 5 V logic levels to 0 to −5 V logic levels, respectively. Although the circuit operates as intended, the RF switch used does not have an internal driver circuit, as such, it has an input pin for each side of the switch. Only one side of the switch will be connected to the output at any given time, this is why two dual inverter logic gates were used (a pair of gates per switch). The circuit used is illustrated by Figure 5.2.

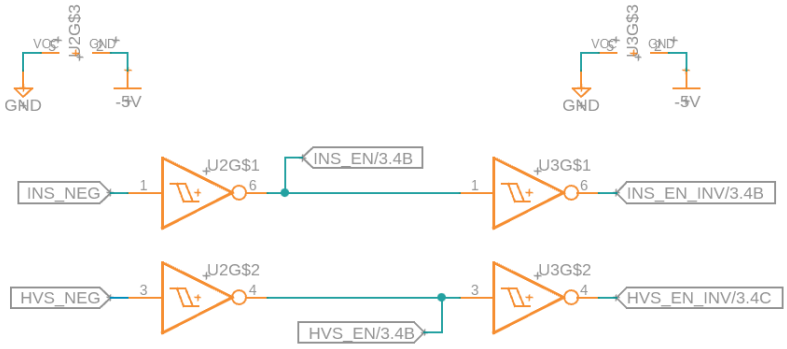

Figure 5.2: RF switch driver circuit.

Note that this circuit operates in the same logic levels as the switches. Hence, the positive supply of each inverter integrated circuit connects to the ground rail, and ground connects to the negative rail.

5.2.1 PCB Design

After the circuit design, the PCB layout was created. A dedicated PCB was designed and manufactured to allow for the validation of the circuit. The design goal was to keep the circuit as small as possible so that when it is included in the probe, it occupies as little space as possible to reduce the chance of interfering with the antenna itself. The test board layout is shown in Figure 5.3.

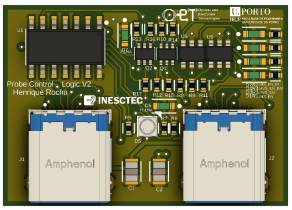

Figure 5.3: RF switching circuit driver test PCB.

To be able to visualize that the circuit was working properly, LEDs were installed in the place of the RF switches and LNAs, for this purpose, standard green LEDs were used. To smooth current spikes that may be required by the microcontroller and logic circuitry, 10 µF decoupling capacitors were installed in each of the supply rails. Last but not least, a connector had to be chosen, which had to be readily available, provide sufficient pins for communication and power, and have enough current carrying capability. For this application, the USB-C connector was selected, which is rated up to 5 A. Only the connector was used in this scenario, not the USB protocol, as such, custom USB-C breakout boards and cables were made. The detailed implementation is described in section 5.3.

5.3 USB Breakout Board

As previously mentioned, the USB protocol was not used. As such, a custom USB-C cable is required for proper operation. A simple breakout board was designed for the male version of the aforementioned USB-C connector. Figure 5.4 shows the pinout used for the USB-C connector.

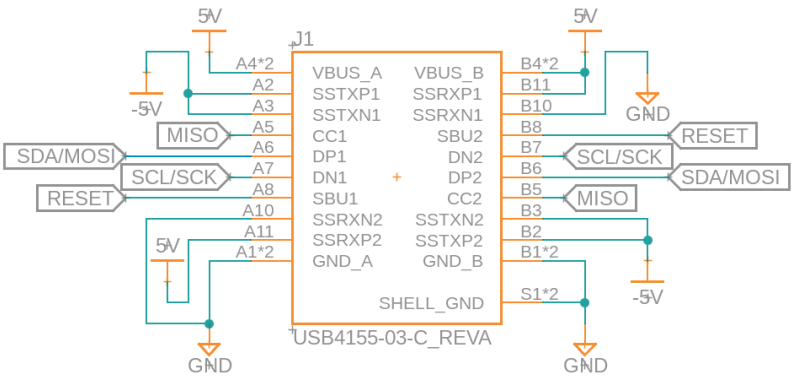

Figure 5.4: USB-C connector pin assignment.

5.3.1 PCB Design

The design of this PCB is very simple. The only function of the PCB is to allow the connection of a wire to the plug, as the pins are too small. Furthermore, some extra PCB length was added to provide space to fit the legend of the connections and to secure the cable that will be connected. Figure 5.5 shows the 3D model of the breakout board.

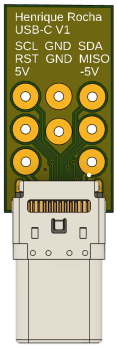

Figure 5.5: USB-C breakout board 3D model.

5.4 IO Expander

A dedicated expansion board was developed to provide a way to control extra devices in the anechoic chamber system. These devices include the positioner driver and a LASER to allow the user to properly align the phase center of the AUT with the center of rotation of the positioner. In this circuit, all eight GPIOs were used. Four available GPIOs control the gate of four NMOS transistors with pulldown resistors. The outputs are open drain and allow higher-current devices, up to 500 mA per output, to be connected. The remaining four GPIOs can be programmed in runtime to behave as inputs or outputs. This board only has one connector, as it is intended to be the last device in the chain.

5.4.1 PCB Design

Once again, the goal was to keep the layout as small as possible, even though, for this circuit, it is not critical. Terminal blocks were used to facilitate the connections to this board. Figure 5.6 shows the 3D model of the designed PCB.

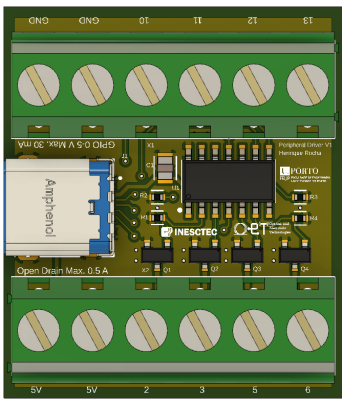

Figure 5.6: IO expander 3D model.

5.5 Power Supply

The power supply board serves two purposes. The first is to provide the correct voltage levels to the circuits described before. The second is to provide a place to connect the programmer and the communication master. As a safety measurement, a reverse polarity input protection circuit was designed. The circuit is designed around a PMOS transistor that allows the circuit to operate more efficiently when compared to simple diode protection.

After the input protection, the 5 V is directly connected to the positive rail, with some smoothing capacitors in parallel. A charge pump circuit was used to power the negative rail, as the current demand for this rail is quite low. Nevertheless, the negative rail can provide up to 200 mA to the load. The circuit used is the LM2663M/NOPB, as illustrated in the schematic in Figure 5.7.

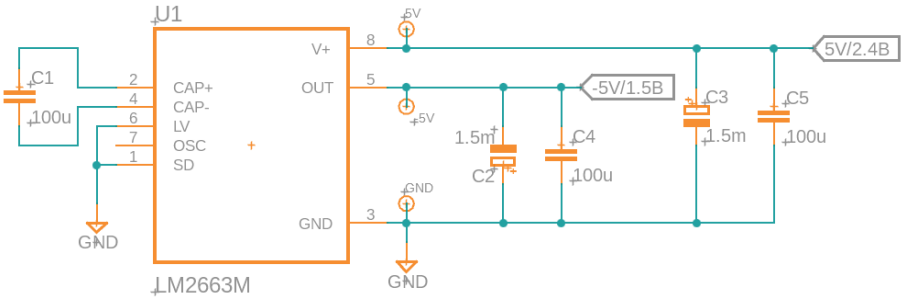

Figure 5.7: Negative rail power supply circuit schematic.

5.5.1 PCB Design

Similarly to the last designs, the goal was to design the circuit as compact as possible. In this design, a terminal block was used for easy connection of the external 5 V power supply. However, for the programming and communication pin headers were used. Figure 5.8 shows the PCB layout 3D model.

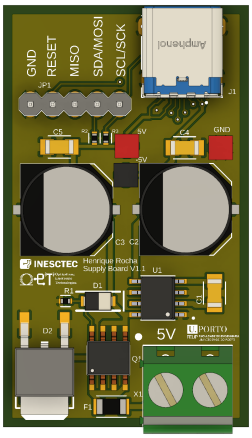

Figure 5.8: Power supply 3D model.

5.6 Experimental Tests

5.6.1 PCB Assembly

After applying the solder paste and placing the components, the PCB was placed on a hotplate to reflow the solder paste. The soldered RF switching circuit driver PCB can be seen in Figure 5.9.

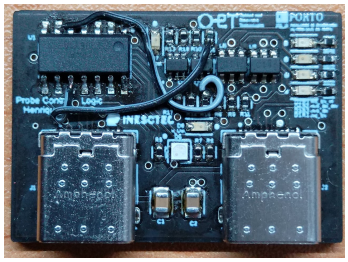

Figure 5.9: RF switching circuit driver PCB.

As you can see, in Figure 5.9, there are some jumper wires. The wires were added due to an error in the design process that led to the misconnection between the GPIOs and the gate of the transistors that drive the logic of the RF switches. This mistake was then corrected in the probe PCB.

The completed IO expander board can be seen in Figure 5.10.

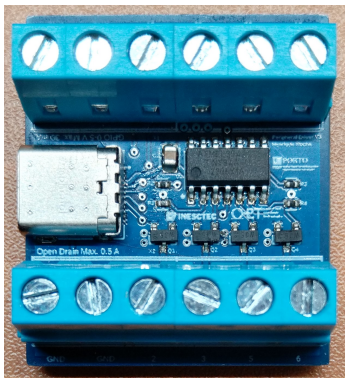

Figure 5.10: IO expander PCB.

Figure 5.11 shows the power supply PCB. Although this PCB was operational, some details were missing, namely the legend for the pins assigned to the programmer, which was then fixed.

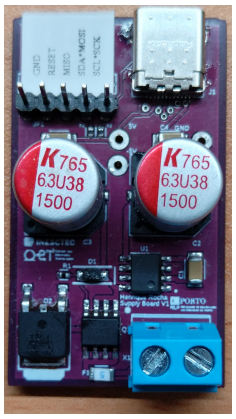

Figure 5.11: Power supply PCB.

Last but not least, the USB-C breakout board was also assembled, allowing for complete programming and communication tests. The final result can be seen in Figure 5.12.

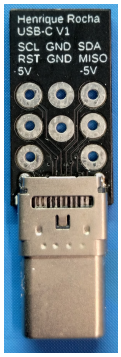

Figure 5.12: USB-C breakout board PCB.

5.6.2 Measurements

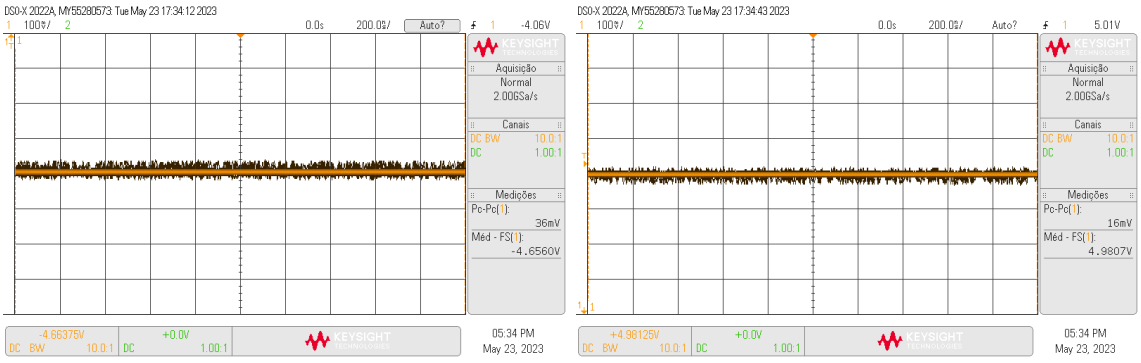

(a) Negative rail. (b) Positive rail.

Figure 5.13: Power supply output voltage measurement.

To fully test the designed circuits, several steps were taken. First, the power supply was measured using dedicated test points, visible in 5.11 as unpopulated through holes. The results shown in Figure 5.13 were performed for a load current of 150 mA.

Considering that the power supply used has 5 V across its output terminal, the small voltage drop of 20 mV can be justified by the voltage drop caused by the on-resistance of the input protection Metal Oxide Field Effect Transistor (MOSFET) and the cable resistance of the jumper wires used to connect the lab power supply to the designed PCB. We can also see that the negative rail is not exactly symmetrical to the positive rail, though this slight difference should not pose a problem. To better probe the voltage, a small inductance ground connection was used, shown in Figure 5.14. With this method, a maximum voltage variation of 36 mV was measured. The ripple voltage represents a 0.7 % variation of the DC value.

Figure 5.14: Low impedance ground probe.

After validating the correct operation of the power supply, the USB-C breakout board was tested. In fact, by confirming that there is a connection between the exposed pads on the breakout board and the programming/power pins and the power supply PCB both the solder joints in the breakout board and the power supply are validated. This process was repeated for all manufactured breakout boards. In the end, all six passed the test. With the breakout boards operational, some cables were made using a flat ethernet cable, as seen in Figure 5.15. Ethernet cables have eight wires, so the GND connection has two pads, corresponding to two wires.

Figure 5.15: Custom USB-C to USB-C cable.

With the cable manufactured, the RF switching circuit driver PCB was plugged in. Then the connections between the power supply board and the switching circuit could be tested. After validating the connections on both USB-C ports, an Arduino was used to flash the bootloader and upload a simple sketch to enable the outputs used one by one and check that everything was

operational. As already mentioned, some problems were encountered and then fixed in the final design.

The last circuit to be tested was the IO expander. Similarly to the last circuit, first, the connections were validated followed by the operation of the circuit. No problems were found with this circuit.

Having the two circuits operational allowed communication tests to be performed. The testing setup is depicted in Figure 5.16.

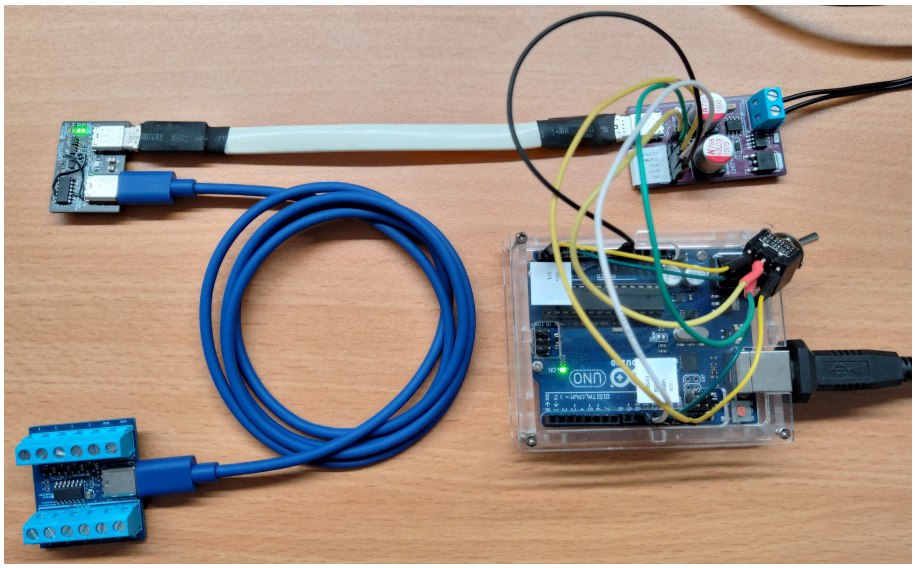

Figure 5.16: Control circuitry test setup.

On the bottom right corner of Figure 5.16, the Arduino UNO serves a dual purpose. On the one hand, the UNO is the programmer. On the other hand, it serves as a master for the I^2C communication protocol. The toggle switch, visible on top of the UNO, allows for easy rewiring between the communication pins and the programming pins. The blue cable, visible in the same Figure, is a commercial USB-C cable that only supports USB 2.0. As such, it can be used to power the IO Expander, as it does not require a negative supply.

To better interact with the developed system, a custom front panel was designed for testing purposes. The main interface windows can be seen in Figure 5.17. Note that in the IO extender window, it is possible to define the GPIO pins as either inputs or outputs in runtime, allowing more circuit flexibility even after installation.

The program was written in Python and used the images obtained from Fusion 360 (the software used to design the PCBs), for the case of the PCBs and from HFSS for the case of the chamber structure. With this program, it was clear to see that the system was operating as expected.

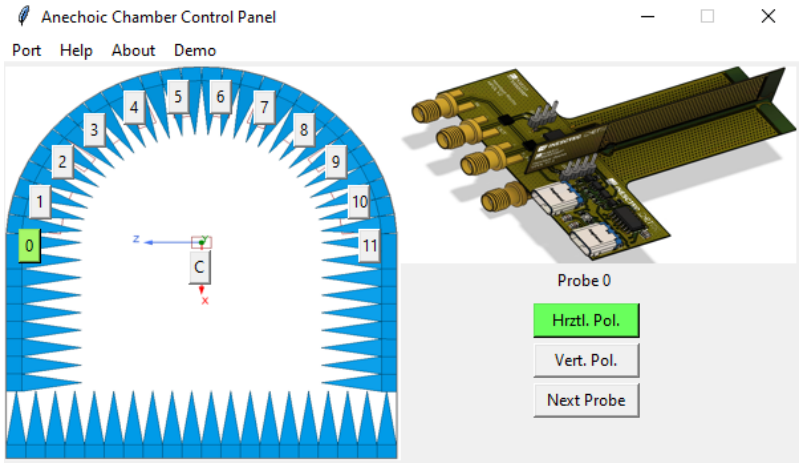

(a) Probe window.

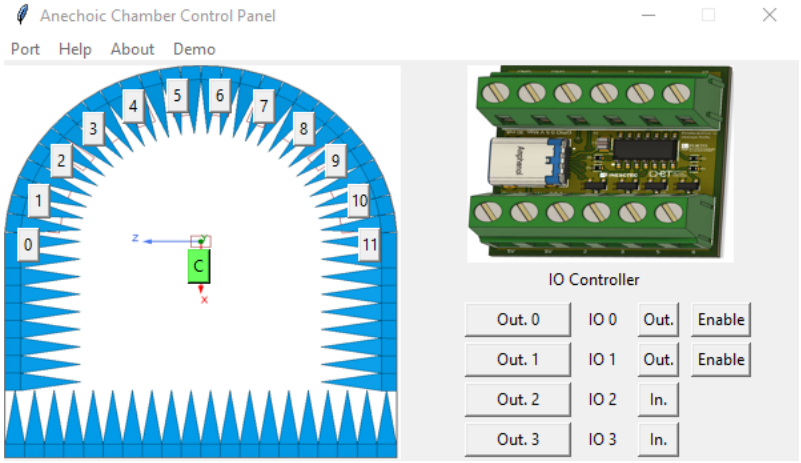

(b) IO expander window.

Figure 5.17: Control circuitry graphical interface.

5.7 Sumary

In this chapter, the work developed regarding the control circuitry was presented. This work included the design and validation of the driver circuit developed for the RF switching circuit, the IO expander board used to control the alignment LASER and the positioner, and a power supply to power the circuits. Furthermore, a custom USB-C cable was developed to allow for easy connections between devices, along with a test program to validate the system's operation.

Chapter 6

Probe Design

6.1 Introduction

This section will go through the design process of the measurement probes. In this case, the probes will only receive the signal emitted by the AUT. The decision was made because the conversion algorithms require dual polarization to process the collected data [3, p.997]. If the probes were used as transmitters the AUT would require dual polarization which is not always the case.

A near-field probe should follow the listed requirements to accurately measure the electric field distribution surrounding the AUT [29]:

- Any distortion of the fields by the probe and associated equipment must not seriously affect the accuracy of the measurements.
- The probe's aperture must be small enough to approximate the measurement of the field to a point.
- The probe must have the desired polarization to a high degree of accuracy.
- The probe must deliver a suitable signal voltage for accurate measurement.

In terms of frequency, the probe was intended to operate between 1 and 30 GHz. Knowing that, for such large bandwidth, it was expected that the probe would not be matched to the typical characteristic impedance of 50 Ω. It is also expected that the gain and radiation pattern of the probe will change with the frequency. Nevertheless, the probe was designed with the intent of not having a null in the radiation pattern towards the front of the probe.

Following the requirement list shown above, the probe was designed with the intent of having an antenna aperture that is small when compared to the wavelength. An LNA was installed between the probe output and the RF switching circuit's input to achieve a better signal level and, consequently, a better SNR. In fact, the LNA has two important tasks, one already stated, and the other is to isolate the radiative element of the probe to the rest of the RF circuit, *i.e.* the impedance

of the output of the LNA is designed to maintain the nominal impedance of 50 Ω. Even though the transmission line that feeds the antenna was designed to have a characteristic impedance of 50 Ω, the impedance of the antenna varies, which causes reflections in the feed line, which can cause the line to radiate. Finally, a goal of more than 40 dB of cross-polarization isolation and isolation between each polarization was set [3, p.1024].

Several probe antenna types were considered based on the literature reviewed, such as shielded loops, tapered waveguides, electric dipoles, and biconical antennas. From which it was concluded that the size of half-wave dipoles or smaller were determined to be necessary for accurate measurements [30]. Based on the information retrieved, a small electric dipole was selected.

The challenging task of the near field probes lies in the mechanical construction and how the dipole is fed. Ideally, the dipoles would be placed in the same plane so that the measurement surface remained unchanged as well as the dipole phase center. The intended probe design features one PCB per polarization that must fit in each other. In this design, only RF ground is shared, and the signal is transported via a coaxial cable between PCBs. The final probe design is based on the work presented in [31]–[33].

In the next subsections, the four simulated probe designs are presented. The first design was based on a dipole fed by a parallel conductor transmission line. While the last iteration also used a dipole, the feeding network changed to a different approach. All the antenna simulations were performed in the far-field, considering the limitation mentioned above. The simulations were performed in the far-field as the conversion algorithms that transpose the information from the near-field to the far-field were beyond the scope of this dissertation. Furthermore, the antenna tests were also performed in the far-field given the equipment available.

6.2 Parallel Conductor Fed Dipole

The first probe design used a dipole fed by a parallel conductor transmission line, one conductor per copper layer. When using a dipole antenna, some care has to be taken in the way the feed network is implemented. A dipole is a balanced antenna, and the rest of the RF signal path is unbalanced, as explained in section 2.3. To avoid radiation occurring from the ground plane, a BALUN has to be designed to connect the balanced line to the unbalanced one.

To verify if the design would work, a simulation was performed with only one polarization with no BALUN, this was done to validate that the dipole operated as expected in the entire frequency range. Note that the way the transmission line is fed is balanced as the lumped port used touches both conductors. The simulation model, shown in Figure 6.1, was defined so that the substrate and copper thickness, as well as the substrate type, were the same as those available for manufacturing. In this case, the model uses RO4350 with 0.254 mm thickness and 35 µm thick copper on the top and bottom layer, these properties were kept for all the subsequent designs.

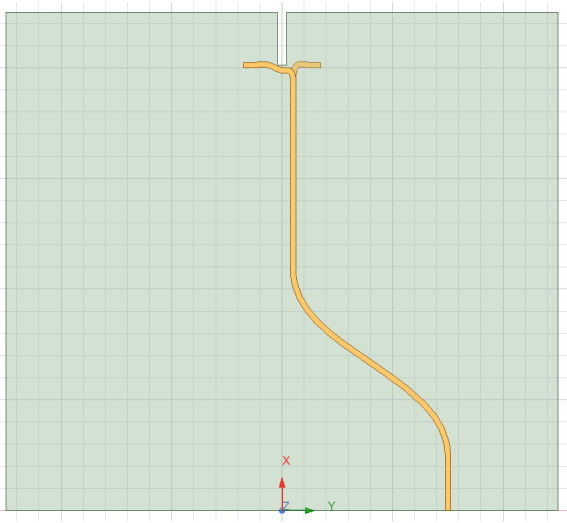

Figure 6.1: Dipole probe simulation model.

After performing the simulation the co and cross-polarization realized gain towards the front of the model were measured and plotted, as illustrated in Figure 6.2 with the blue and orange lines, respectively.

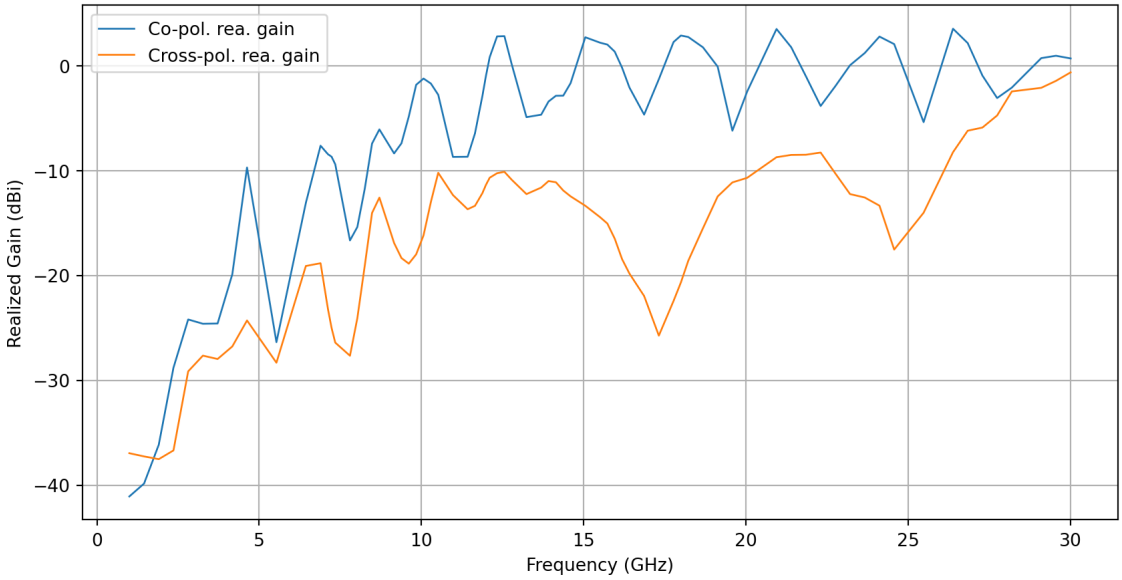

Figure 6.2: Dipole probe simulated realized gain (dBi) in the X axis direction.

After analyzing the results, we can observe that the cross-polarization isolation was not satisfactory. Another problem with this design has to do with the way the dipole is fed. Due to the construction of the probes, the transmission line that feeds the dipole has to suffer a sharp turn, causing unbalance in the dipole, in turn, this causes the direction of maximum gain to shift towards the longer arm, which is undesired. Due to the results obtained, this design was put to the side.

6.3 Slot Line Fed Dipole

A slot line is quite convenient to use in the intended design, as it serves a dual purpose. First, by design, this transmission line does not have copper in its center, which allows for easy assembly of the orthogonal probes. Furthermore, it serves as a BALUN because the connection to the dipole is done as a balanced transmission line but the feed of the slot line itself is unbalanced. The inspiration for this design came from the typical feed of a Vivaldi antenna, usually done with a slot line (Figure 6.3(a)), but instead of feeding a Vivaldi the slot line would feed a dipole as illustrated by Figure 6.3(b).

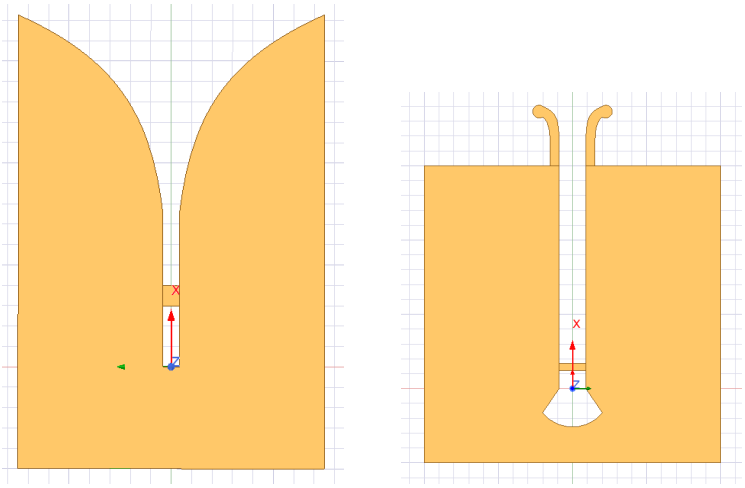

(a) Vivaldi fed with slot line. (b) Dipole fed with slot line.

Figure 6.3: Slot line feed.

The feed of a slot line can be done in more than one way [34], [35]. This is why microstrip and CPWG transmission lines were used in the simulation. The first approach was to use a microstrip line feed.

6.3.1 Open Microstrip

A microstrip-to-slot line transition uses two copper layers to do so. To achieve the best line coupling between a microstrip and a slot line, they have to be orthogonal to each other and adequately terminated [34]. For this application, the slot and microstrip lines were terminated by an open stub. Given that the probe has to operate in such a large frequency band, the transition between the aforementioned lines was first designed based on existing designs and then optimized in a separate simulation to then be placed on the probe model. Figure 6.4 shows the model used to optimize the transition.

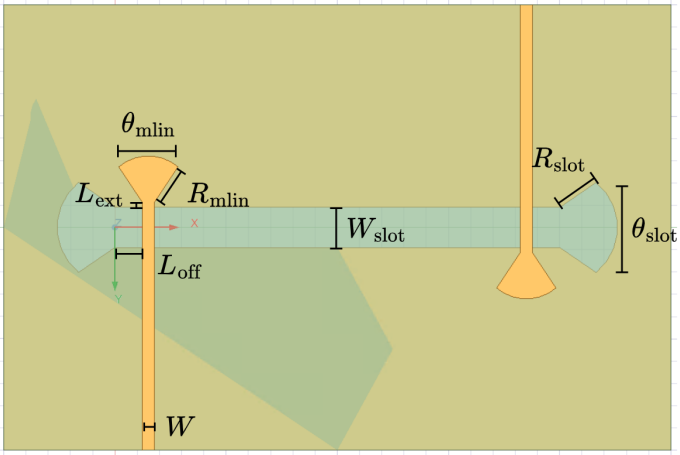

Figure 6.4: Open microstrip to slot line transition optimization model.

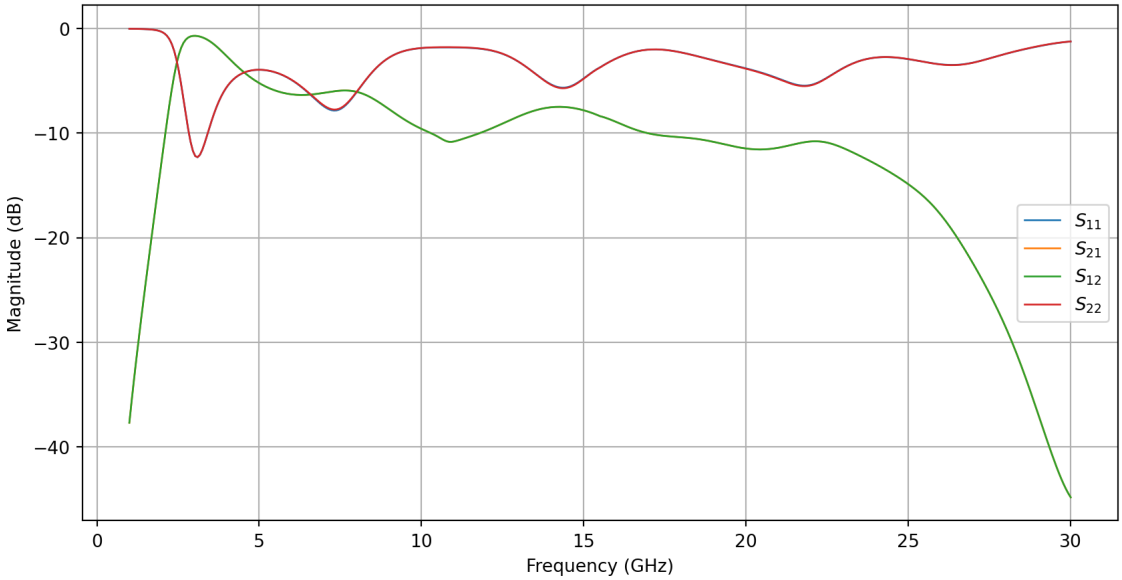

Figure 6.5: Open microstrip to slot line transition S parameters.

The first optimization was performed for a fixed slot line width of 1 mm. The initial width was chosen considering the space required to fit the other polarization board. The height of the fully assembled PCB used is approximately 0.324 mm, so a 0.3 mm gap on each side was considered sufficient. This proved not to be the case, as the coupling between polarizations was above the desired maximum (which is not represented for this design), as explained in section 6.3.3, so the slot line width was increased to 1.8 mm. Although the microstrip designs were put to the side due to the insufficient cross-polarization isolation of the probe, the same slot line width was used so that the designs could be better compared. The length of the slot line was chosen arbitrarily in such a way that the feed lines were far enough from each other to avoid direct coupling between them, as demonstrated in Appendix D.

During the optimization process, the position of the microstrip line relative to the end of the slot line was changed, as well as the radius of the microstrip line and slot line stubs, and the angle of the previous was also changed.

After performing the optimization, the S parameters were plotted, as illustrated by Figure 6.5. The dimensions obtained after the optimization process, as specified in Figure 6.4 are listed in Table 6.1.

Table 6.1: Dimensions used in the transition model.

Variable	Final Value
W_{slot}	1.8 mm
R_{slot}	2.6 mm
θ_{slot}	51°
L_{off}	2.2 mm
L_{ext}	0.2 mm
W	0.56 mm
R_{mlin}	2.1 mm
θ_{mlin}	40°

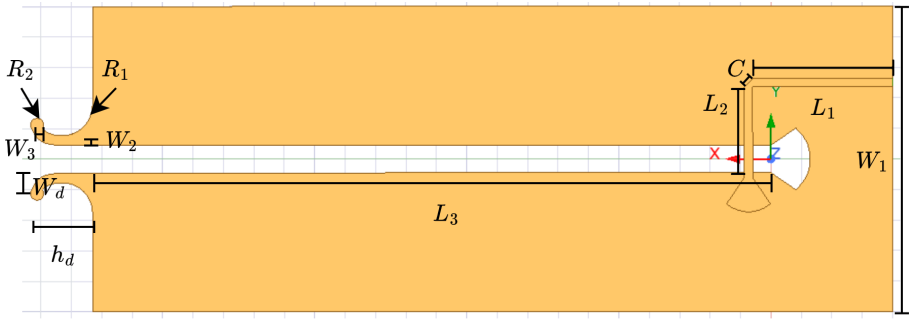

(a) Top view.

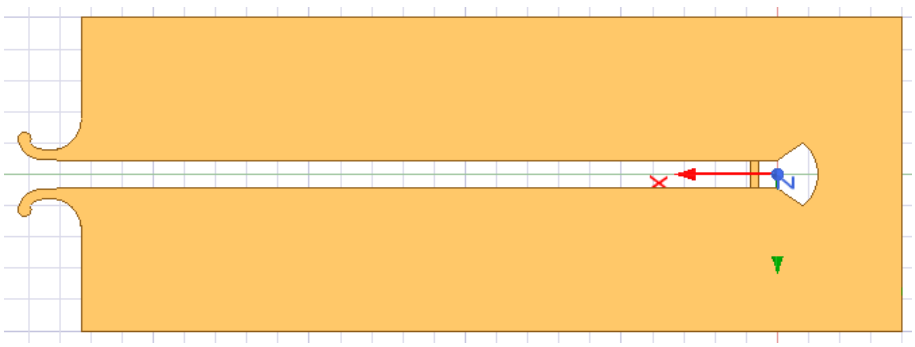

(b) Bottom view.

Figure 6.6: Open microstrip simulation model.

In fact, the results show that there is a high insertion loss in the transition between the microstrip line and the slot line. It is possible to obtain a lower insertion loss as demonstrated in Appendix E, however, the resulting slot line width is not compatible with the intended design. With the values listed in Table 6.1, the probe model was built as illustrated by Figure 6.6.

The presented model was optimized by changing the slot line length, the dipole length and distance to the slot line, and the curvature from the dipole base to the arm extremity. The curve of the dipole is defined by equation (6.1), where $0 \leq k \leq h_{\mathrm{d}}$ and remained unchanged for the subsequent designs. This is because the feed of the dipole (the slot line) remained unchanged also. Note that a_1 and a_3 were computed so that the dipole would have width W_{d} and height h_{d}.

$$\begin{aligned} x(k) &= k \\ y(k) &= a_1 * \exp(2k) + a_2 \\ z(k) &= 0 \end{aligned} \tag{6.1}$$

The values of the variables presented in Figure 6.6(a) and equation (6.1) are listed in Table 6.2, note that the position of the feed line relative to the slot line remained the same.

Table 6.2: Dimensions used in the probe model.

Variable	Final Value
W_1	26 mm
L_1	9.2 mm
L_2	9.3 mm
C	0.55 mm
L_3	44.6 mm
W_2	0.7 mm
W_3	0.6 mm
W_{d}	2 mm
h_{d}	4 mm
R_1	2 mm
R_2	0.5 mm

The realized gain for co and cross-polarization for this design are illustrated by Figure 6.7, represented by the blue and orange lines respectively.

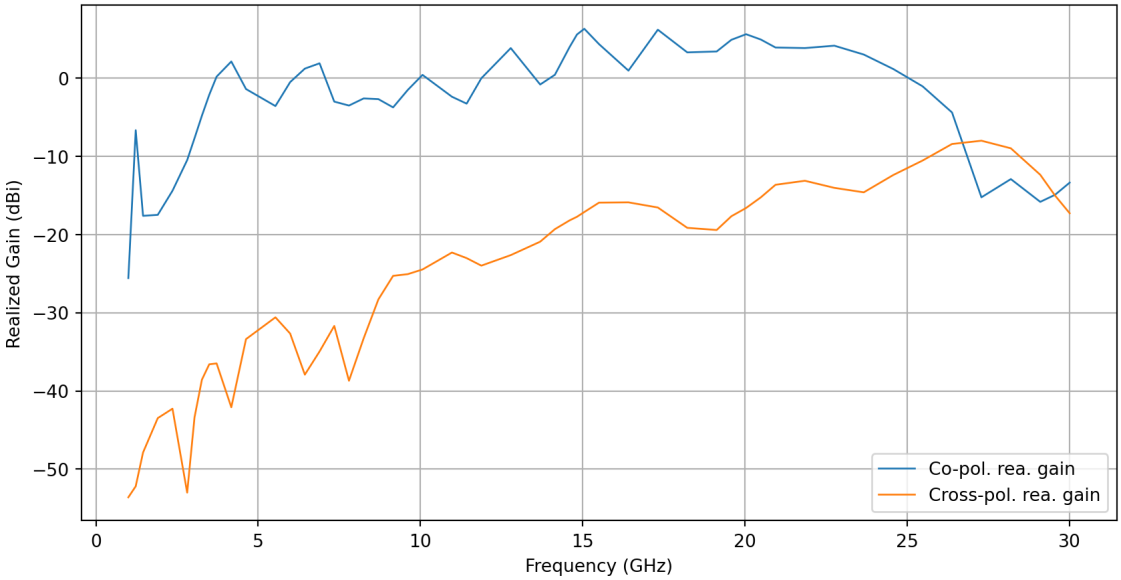

Figure 6.7: Open microstrip simulated realized gain (dBi) in the X axis direction.

Ideally, the cross-polarization gain would be zero (in linear scale). For this design, the cross-polarization gain is higher than the co-polarization gain for frequencies above 27.5 dB. For this reason, no further analysis was performed for this design, as better results were not achieved.

6.3.2 Shorted Microstrip

As stated in section 6.3, there is more than one way to feed a slot line. In this subsection, a shorted microstrip line feed was tested. The design process was similar to the previous one. The optimization model is shown in Figure 6.8. Because the termination of the slot line had already been optimized, in this case, only the distance to the end of the slot line was optimized.

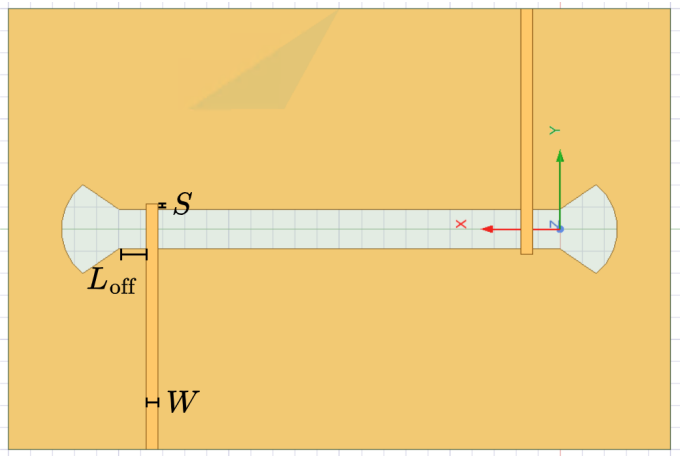

Figure 6.8: Shorted microstrip to slot line transition optimization model.

The dimensions obtained after the optimization process, as specified in Figure 6.8 are listed in Table 6.3. Note that the L_{off} value obtained is equal to the one previously obtained. This is expected as the open stub on the microstrip line is intended to create a virtual short.

Table 6.3: Dimensions used in the transition model.

Variable	Final Value
W	0.56 mm
L_{off}	2.2 mm
S	0.2 mm

Figure 6.9 contains the S parameters obtained after the optimization process, which are similar to the previous design.

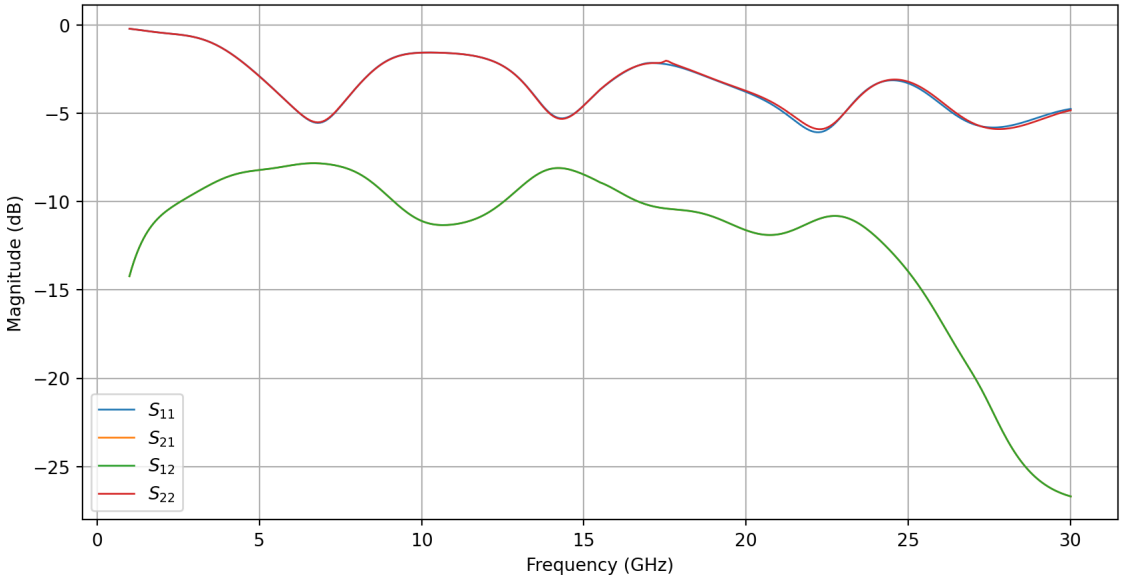

Figure 6.9: Shorted microstrip to slot line transition S parameters.

The probe model was then created, as illustrated by Figure 6.10. Given that in the last design, the length of the slot line and dipole dimensions were already optimized no changes were made to them in this design.

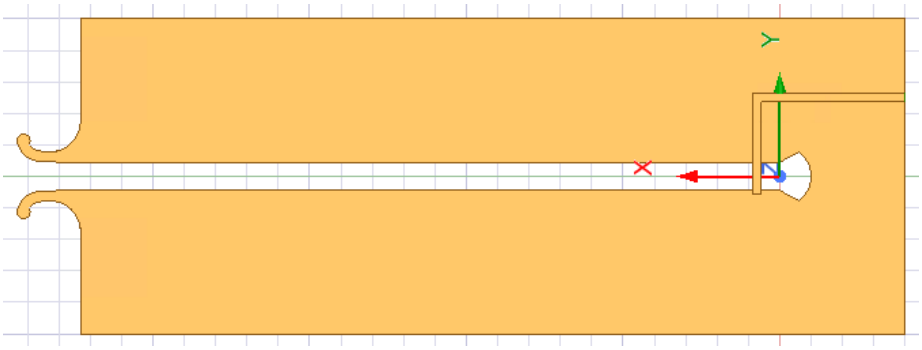

(a) Top view.

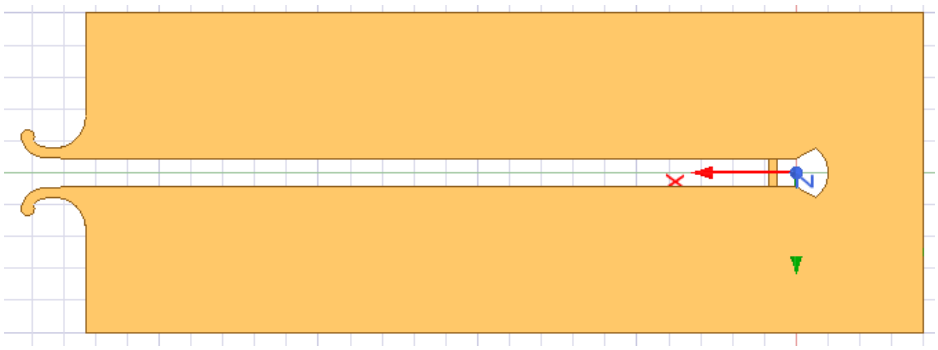

(b) Bottom view.

Figure 6.10: Shorted microstrip simulation model.

Similarly to the previous design, the realized gain in co and cross-polarization was plotted to verify that this design is suitable for the intended application. Figure 6.11 illustrates the obtained results for the realized gain, using the same color code as in the last design.

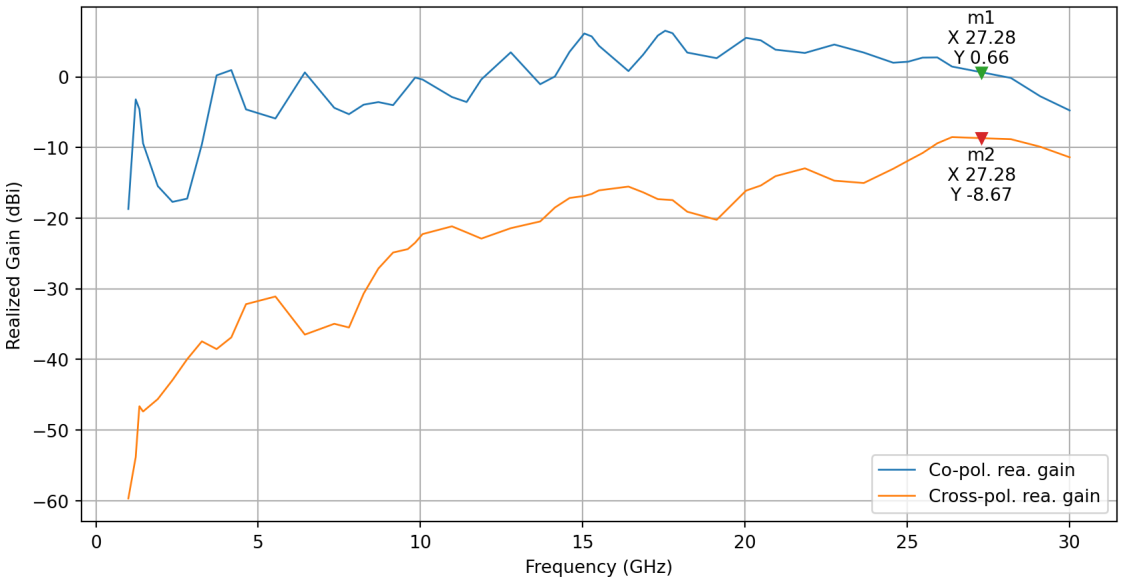

Figure 6.11: Shorted microstrip simulated realized gain (dBi) in the X axis direction.

In this case, there was a performance improvement when compared to the last design. However, at the higher frequencies, the cross-polarization gain is still too close to the co-polarization gain. For this reason, no further analysis was performed for this design and the feed transmission line was changed to CPWG as explained in the next section.

6.3.3 Shorted CPWG

In this design, a shorted CPWG transmission line was used to feed the slot line. As for the previous designs, first, an optimization of the transition was performed. In this scenario, given the way the slot line is fed, an optimization of the slot line termination was performed along with the distance of the feed to the end of the slot line. The width of the slot line, as previously mentioned was increased to at 1.8 mm to reduce the coupling between polarizations, it was not further increased as a larger width had a small effect on the polarization coupling. The optimization model used is shown in Figure 6.12. A block of metal was used as the ground plane instead of two separate sheets, this is done to ensure that top and bottom copper are kept at the same voltage potential. In the PCB, this is achieved by using via stitching, which was not included in the model to remove unnecessary complexity. Using a block of metal in the simulated model is valid as long as the distance between vias is kept small enough. As a rule of thumb, for regions close to the transmission lines, where the current is maximum, a distance between vias of $\lambda/10$ was used, and for the rest of the ground plane, a distance of $\lambda/5$ was used.

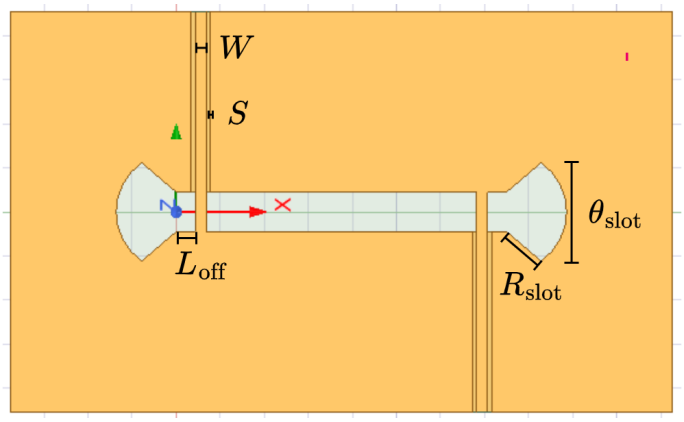

Figure 6.12: Shorted CPWG to slot line transition optimization model.

Figure 6.13 shows the S parameters of the transition obtained after the optimization. From the simulated designs, this one obtained the best results. As we can see, the insertion loss is lower when compared to the previously simulated models.

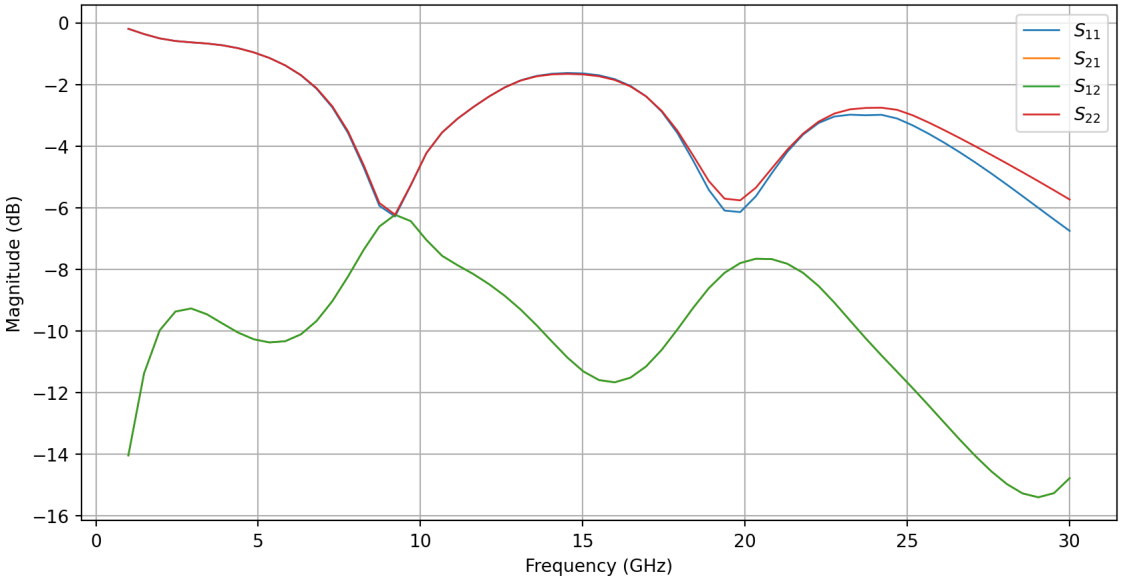

Figure 6.13: Shorted CPWG to slot line transition optimization S parameters.

The dimensions obtained after the optimization process, as specified in Figure 6.12 are listed in Table 6.4.

Table 6.4: Dimensions used in the transition model.

Variable	Final Value
W	0.5 mm
S	0.2 mm
R_{slot}	2.7 mm
θ_{slot}	55°
L_{off}	0.86 mm

After optimizing the transition, the probe model was created as illustrated by Figure 6.14.

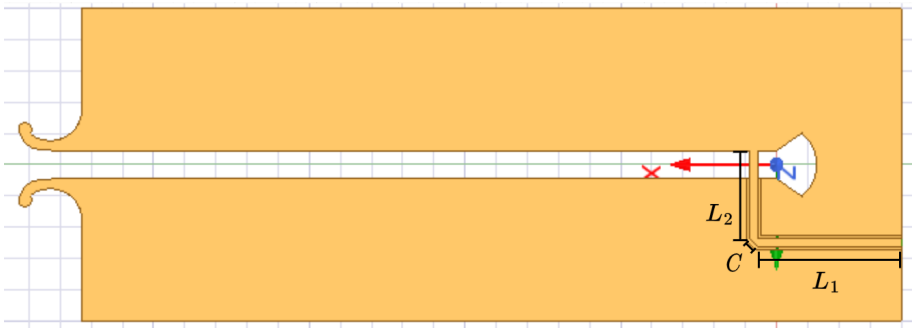

(a) Top view.

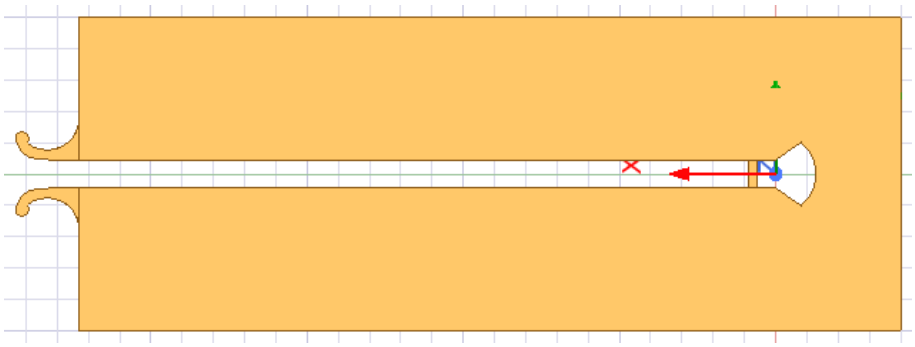

(b) Bottom view.

Figure 6.14: Shorted CPWG simulation model.

The dimensions of the dipole and slot line were kept the same as in the last models, changing only the line termination and the feed line. The values of the variables presented in Figure 6.14(a) are listed in Table 6.5.

Table 6.5: Dimensions used in the probe model.

Variable	Final Value
L_1	9.2 mm
L_2	9.2 mm
C	0.5 mm

After running a simulation, the realized gain of the co and cross-polarization were measured, as illustrated by Figure 6.15, where the co-polarization gain is represented by the blue trace, and the cross-polarization by the orange trace.

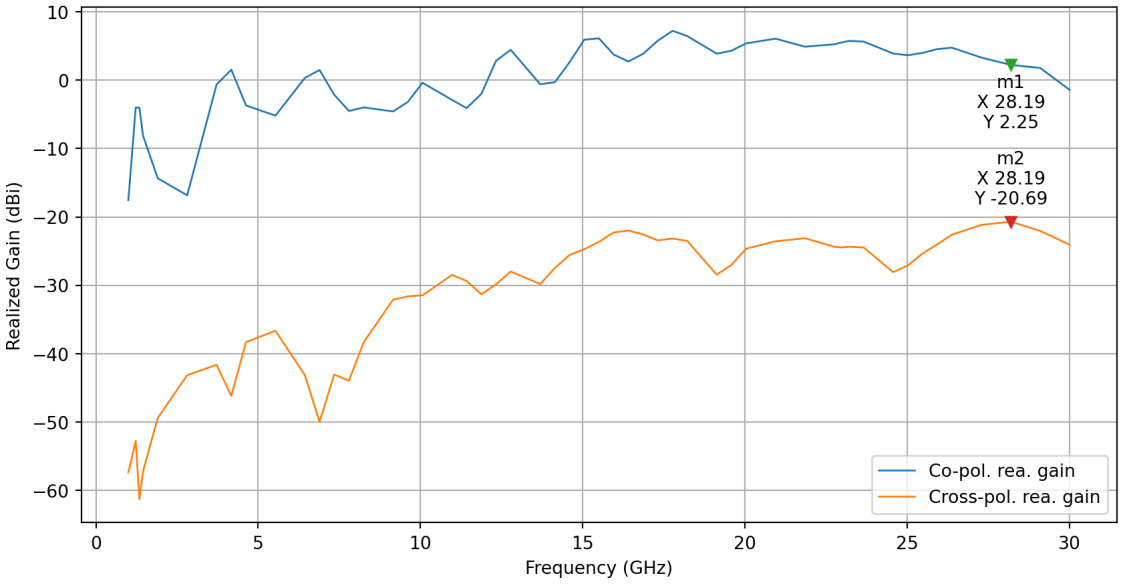

Figure 6.15: Shorted CPWG simulated realized gain (dBi) in the X axis direction.

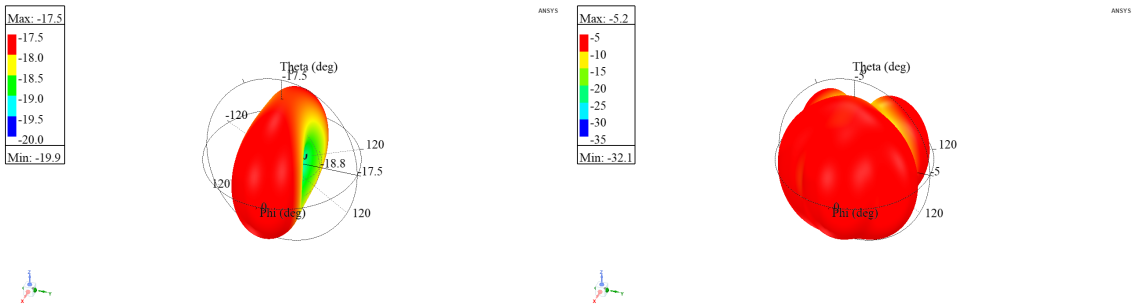

(a) Realized gain at 1 GHz.

(b) Realized gain at 5 GHz.

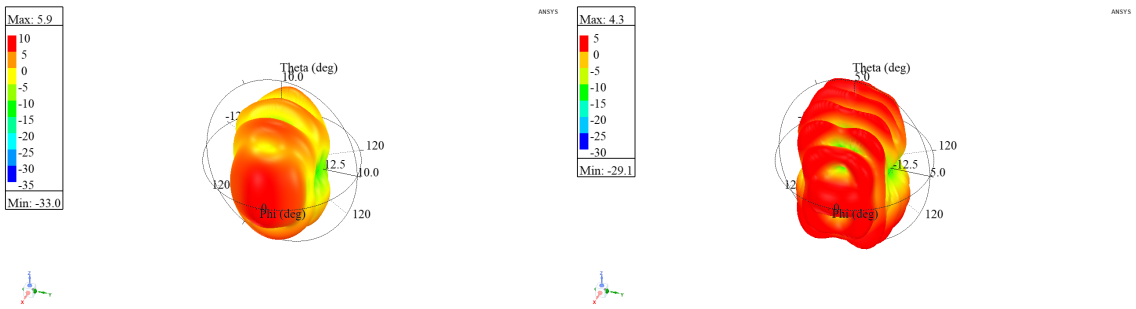

(c) Realized gain at 15 GHz.

(d) Realized gain at 25 GHz.

Figure 6.16: Simulated radiation pattern at different frequencies.

We can now see a significant improvement in the cross-polarization isolation, meaning that a minimum of 23 dB difference between polarization gains was achieved. As previously stated the intended cross-polarization isolation is 40 dB [3, p.1012]. However, due to time contains, it

was not possible to improve the design or to test other designs. So this design was selected to be manufactured, meaning that further analysis was required.

To better visualize the realized gain of the antenna in space, the radiation pattern was plotted. Figure 6.16 illustrates the antenna's radiation pattern that used a color code where red represents the highest realized gain and blue represents the lowest. For the effect, four frequencies were chosen to illustrate the changes in the pattern with frequency.

Considering Figure 6.16, the probe performs as expected. Although the presented radiation patterns are representative of most of the frequency range, at the lower end of the spectrum the probe has reduced radiation toward the front of the probe. This problem coincides with the most significant dip in gain close to 3 GHz. Figure 6.17 illustrates the radiation pattern of the probe at a frequency of 2.8 GHz. As you can see, there is a higher gain toward the side of the probe when compared to the front.

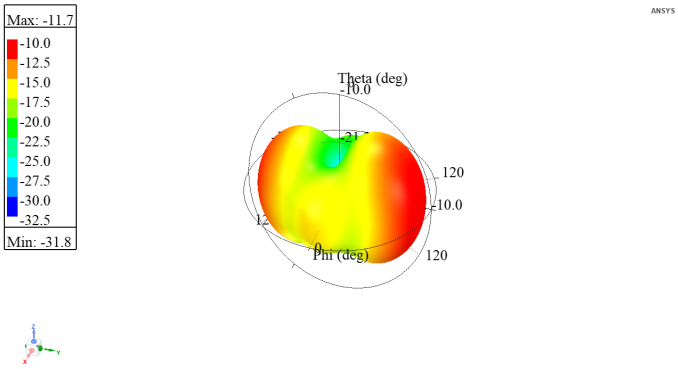

Figure 6.17: Simulated radiation pattern at 2.8 GHz.

To better understand what is causing this problem, the surface current was plotted on the model, as illustrated in Figure 6.18. We can observe that there is, in fact, a current unbalance on the surface of the model that is causing it to radiate in the undesired direction.

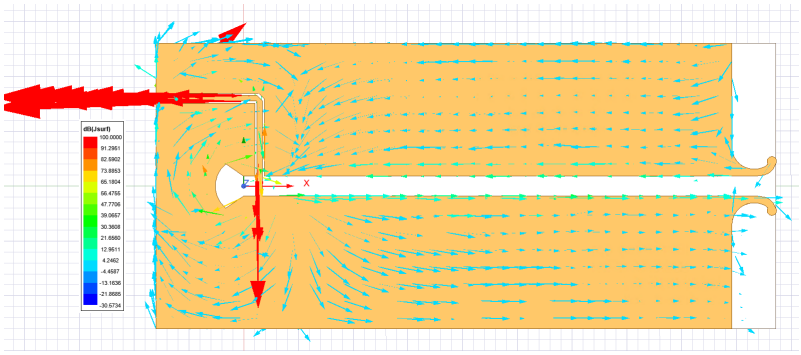

Figure 6.18: Simulated surface current at 2.8 GHz.

Although the probe did not perform as intended for the lower end of the spectrum, it had satisfactory behavior in the remaining frequency range. As such, the next step was to fit both polarization into one assembly. Considering that the RF switching circuit and its control circuit

will be mounted in the same PCB as the probe, extra space was added to the probe. The feed line was slightly extended to leave some free space between the topmost IC and the bottom of the probe already simulated. The extra space was added to avoid disturbing the surface currents that exist at the end of the slot line. If these were affected, it would also affect the performance of the probe. Because of the way the extension was made, it is not expected that the behavior of the completed assembly will significantly change when compared to the single probe previously simulated.

The model present in Figure 6.19 includes space to solder the switching circuit and digital control circuit, with the majority of the integrated circuits installed in the horizontal polarization PCB. For the effect the model shown in Figure 6.14 was extended by 30 mm in the X axis direction and by 22 mm on each side of the extension, for the horizontal polarization, and the vertical polarization was just extended by 30 mm in the X axis direction.

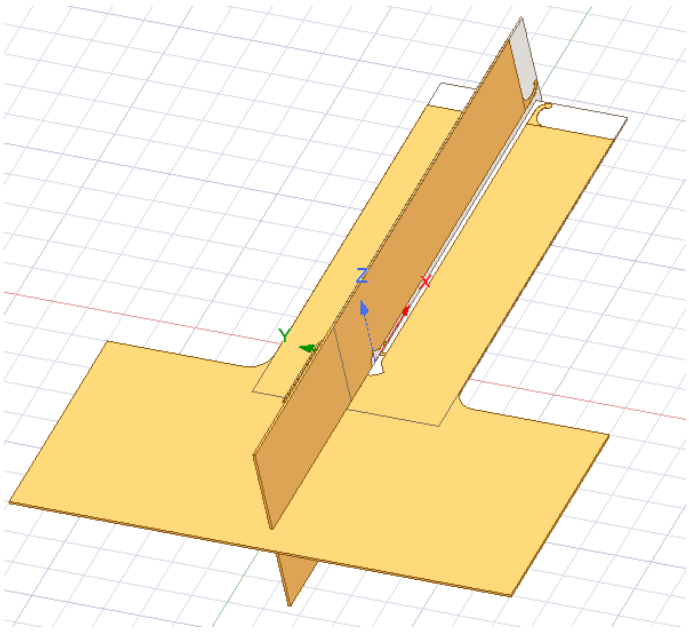

Figure 6.19: Probe assembly simulation model.

As mentioned in section 6.2, the objective was to have both dipoles with the same phase center, with this design, this was only possible in two axes. Considering the axes defined in Figure 6.19 the dipoles only have the same phase center in the Z and Y axes. On the X axis, the phase centers are shifted by 1.5 mm. Considering the horizontal polarization as the reference, the vertical polarization is shifted to allow the CPWG lines to cross each other. The offset between polarizations was optimized with the objective of decreasing the coupling between polarizations while keeping the offset small when compared to the wavelength at the maximum operating frequency. The practical effect of this offset is a phase shift between the fields received by the horizontal probe and the vertical probe. It is expected that the difference in phase of the measured field can be corrected in post-processing, as it is required given that the signal path from the horizontal and vertical polarizations are different. After optimization, the S parameters of the assembly were registered, as illustrated by Figure 6.20, where port one is the port connected to the horizontal polarization.

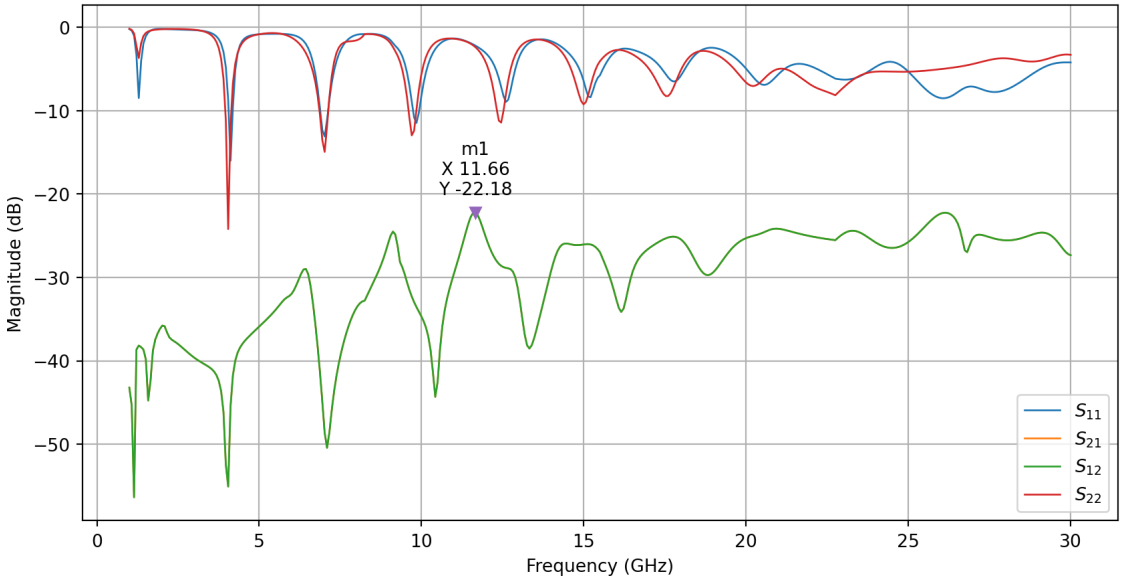

Figure 6.20: Probe assembly simulated S parameters.

As expected, the reflected power is considerable for some frequencies while for others, for example, 17.5 GHz is quite low, though these parameters are not relevant in this situation. The critical parameter is the isolation between polarizations. The higher the isolation, the better the probe will perform [3, p.1012], *i.e.* the lower the orange trace in Figure 6.20, the better.

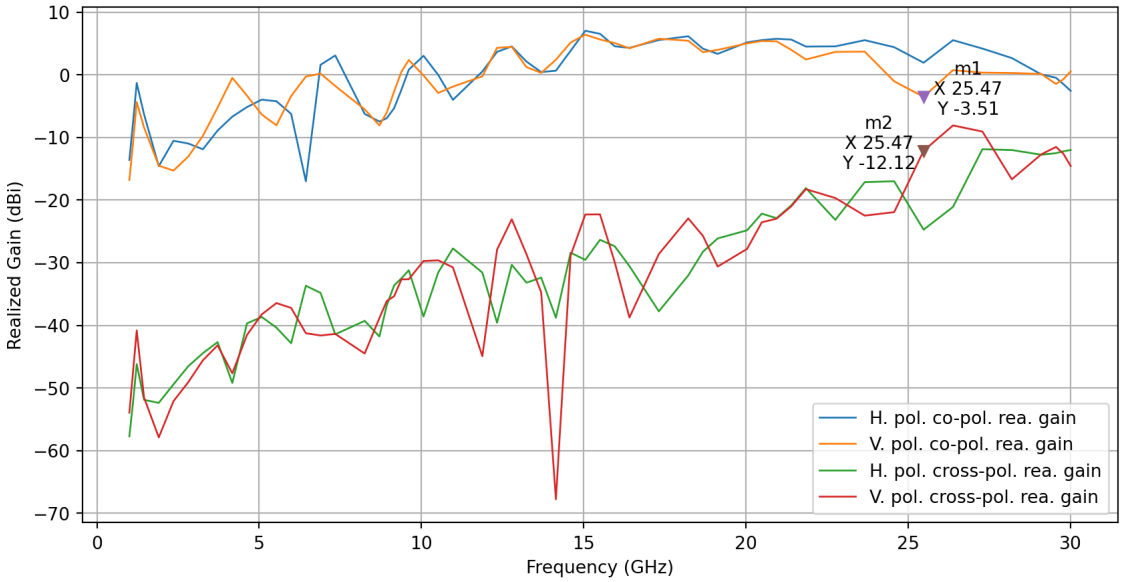

Figure 6.21: Simulated realized gain (dBi) in the X axis direction of both polarizations.

The S_{12} and S_{21} of the complete probe represent the attenuation, in this case, in signal power when a vertically polarized signal is received by the respective polarization and then coupled through to the horizontal polarization and vice versa, which differs from the cross-polarization of the single probe. In other words, the power received by the horizontal polarization (considering

a vertically polarized signal) will have two components, the power received by the horizontal polarization in cross-polarization and the power received by the vertical polarization attenuated by the S_{12}. As you can observe in Figure 6.20 the desired goal of 40 dB could not be achieved. Nonetheless, isolation of 22 dB was achieved over the entire frequency range. Furthermore, tests should be performed to verify if the isolation is sufficient for signal processing or if further design iterations must be performed.

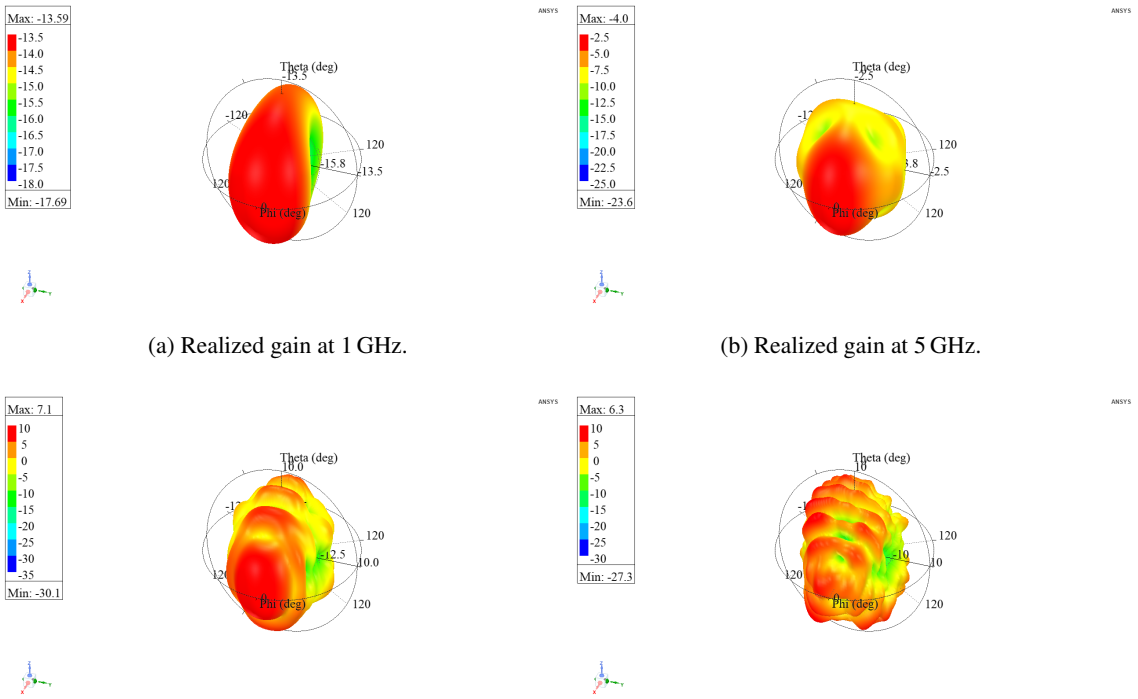

(a) Realized gain at 1 GHz.

(b) Realized gain at 5 GHz.

(c) Realized gain at 15 GHz.

(d) Realized gain at 25 GHz.

Figure 6.22: Simulated horizontal polarization radiation pattern at different frequencies.

To evaluate the effect that the second polarization has on the probe's realized gain, both of the polarizations were fed individually. Figure 6.21 illustrates the realized gain for both polarizations, including the cross-polarization gain. The orange and red traces represent the co and cross-polarization realized gain of the vertical polarization, and the blue and green represent co and cross-polarization realized gain of the horizontal polarization, respectively.

In fact, the behavior of the probe changes when compared to single polarization. The cross-polarization has increased to a minimum of -8.6 dB, significantly decreasing its performance. We can also observe that the vertical polarization was more affected than the horizontal. This is probably caused by the fact that the slot line termination of the vertical polarization is cut due to limitations of the PCB assembly, as this is an area that has a large current density, as illustrated by Figure 6.27, as such slight variations can significantly affect the performance. Future work should be performed on this topic to improve the performance of the design, if possible. Another possible cause is the extended ground at the bottom. However, by observing the surface current density in

the same Figure, this is less likely as there is only residual current in the extended ground area.

Based on the realized gain, it is expected that the radiation pattern also changed. To better visualize the effect, polar plots were created for the horizontal and vertical polarizations as illustrated by Figure 6.22 and Figure 6.23, respectively.

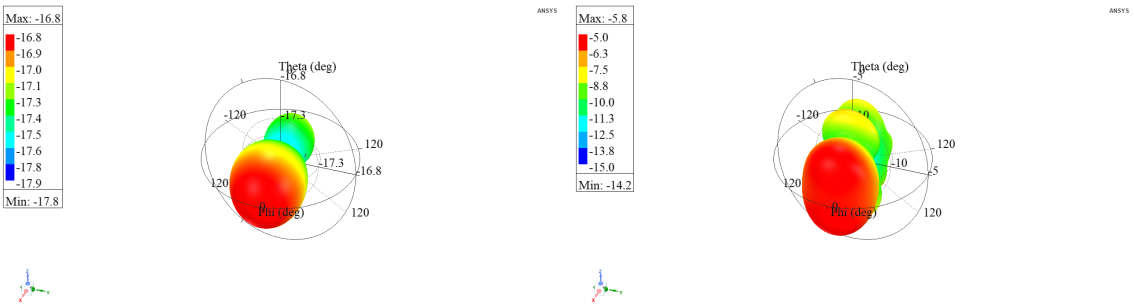

(a) Realized gain at 1 GHz.

(b) Realized gain at 5 GHz.

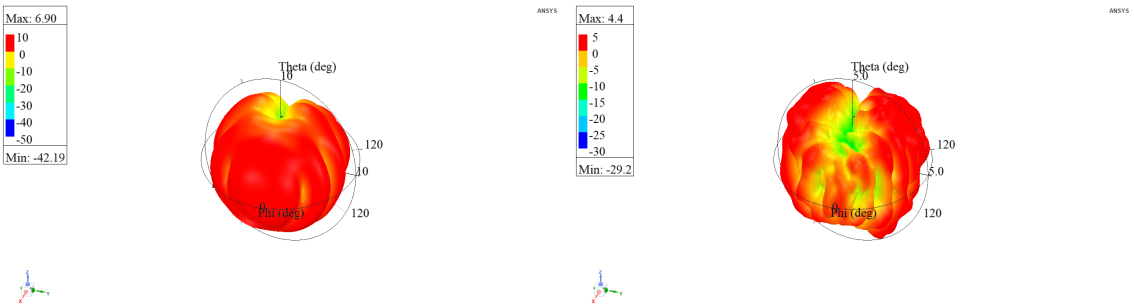

(c) Realized gain at 15 GHz.

(d) Realized gain at 25 GHz.

Figure 6.23: Simulated vertical polarization radiation pattern at different frequencies.

From the polar plots, we can observe that the pattern has indeed changed, but there is still some radiation emitted to the front of the probe. However, near the frequencies where the cross-polarization is reduced, mainly at the top end of the spectrum above 25 GHz, the pattern does not maintain a well-defined main lobe that points to the desired direction, as illustrated in Figure 6.24.

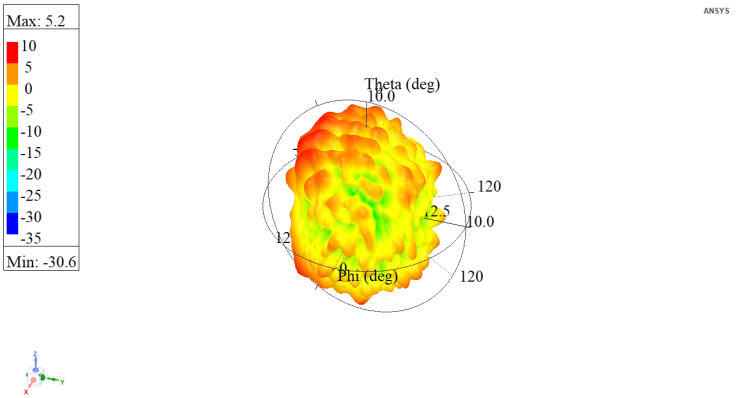

Figure 6.24: Simulated horizontal polarization radiation pattern at 30 GHz.

Even though the cross-polarization did not change considerably at the lower end of the spectrum, the radiation pattern did change. Within the simulated frequencies, it was noticed that for 1.7 GHz, 4.2 GHz, and 6.4 GHz the radiation was being directed to the sides instead of forward. In fact, at 1.7 GHz, the shape of the radiation pattern is the worst, as illustrated by Figure 6.25.

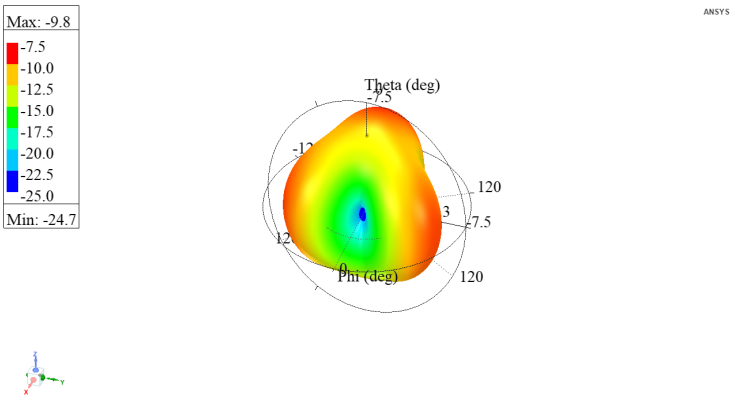

Figure 6.25: Simulated horizontal polarization radiation pattern at 1.7 GHz.

To better understand the source of the problem, the surface current was plotted on the model as illustrated in Figure 6.26.

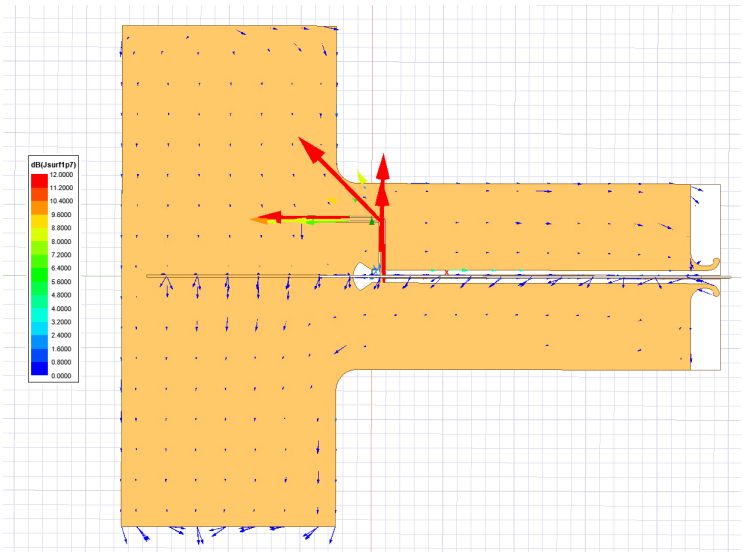

Figure 6.26: Simulated horizontal polarization surface current at 1.7 GHz.

Similarly to the previously analyzed surface current, we can observe that there is an unbalance in the current in the slot line, which is likely what is causing the probe to radiate to the sides. Further work should be performed to try to correct the described problems. However, with this design, it might not be possible to achieve the desired performance.

Hereupon, an analysis of the currents in the ground plane was performed over the full spectrum to ensure that the electronic circuit will not affect the operation of the probe. For the same

reason, the design explored in section 6.2 requires a BALUN to suppress these undesired currents. Considering the same frequencies as the ones used for the polar realized gain plots, Figure 6.27 shows the currents when the horizontal polarization is excited. The current distribution in the vertical polarization is similar to the horizontal.

To better visualize small currents, a logarithmic scale was used. As you can see, the difference between the regions of higher current density and lowest is about 45 dB. In other words, the current density in the green region is about 0.003 % of the current density in the red region. As such, the green and blue regions can be considered areas with only a residual current density. From the previous analysis, we can conclude that the electronic circuit should not affect the operation of the simulated probe. Note that the results presented are only for four representative frequencies, but the current distribution for the rest of the simulated frequencies was also analyzed, yielding similar current distribution to the one presented (in terms of surface current density), except for 1.7 GHz, which had significant current in some areas of the extended ground.

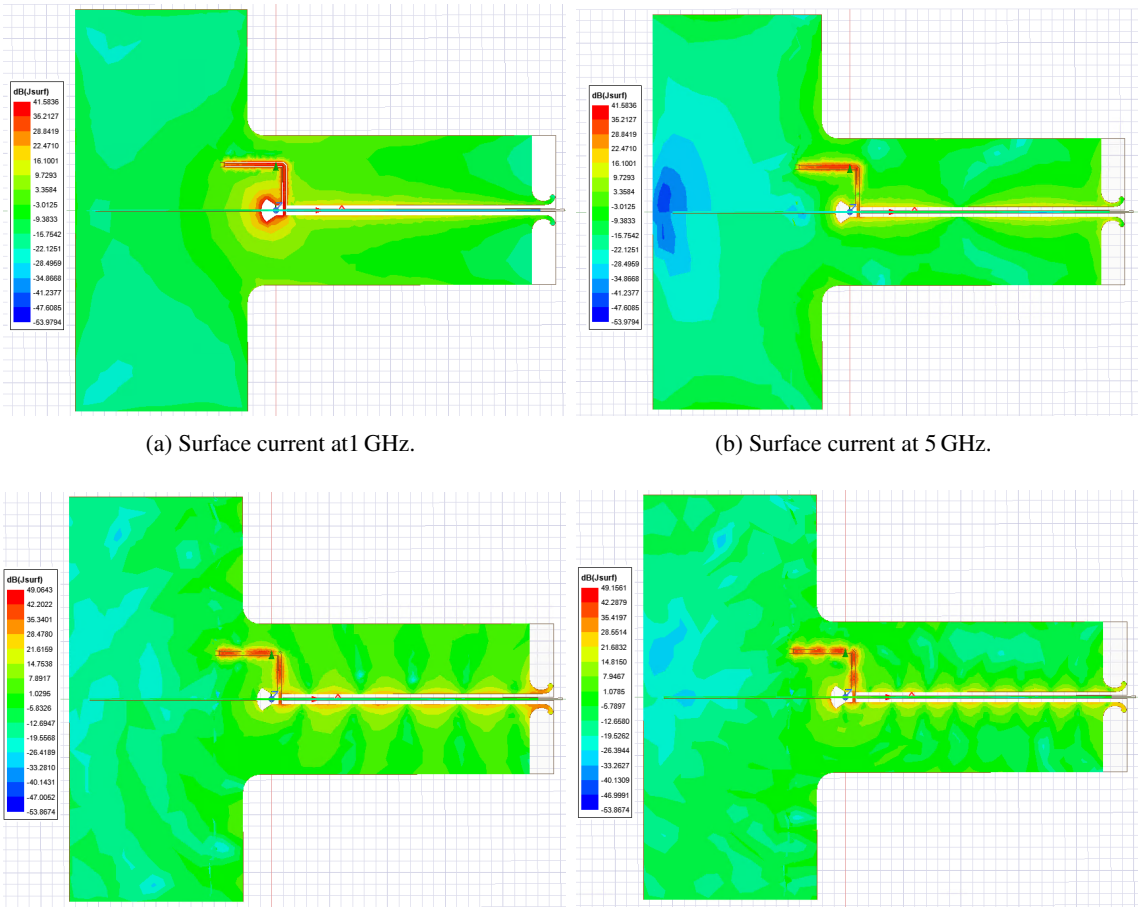

(a) Surface current at1 GHz.

(b) Surface current at 5 GHz.

(c) Surface current at 15 GHz.

(d) Surface current at 25 GHz.

Figure 6.27: Simulated horizontal polarization surface current at different frequencies.

6.4 PCB Design

As previously mentioned, the CPWG design was selected to be manufactured, even with the aforementioned issues. Due to time constraints, it was not possible to correct the described problems or to test other designs.

The models created in HFSS were imported into Fusion 360 as Drawing Interchange Format (DXF) files and then used to create a component in a custom electronic library inside Fusion. After joining the RF switching circuit, the logic control circuit, and the probe in the schematic, the layout was designed. Figure 6.28 illustrates the generated PCB 3D model. Note that to emulate the simulated ground block via stitching was used with a separation of $\lambda/10$ (considering the wavelength on the transmission line) on the sections of higher current, *i.e.* close to the transmission lines, and a separation of $\lambda/5$ on the rest of the PCB.

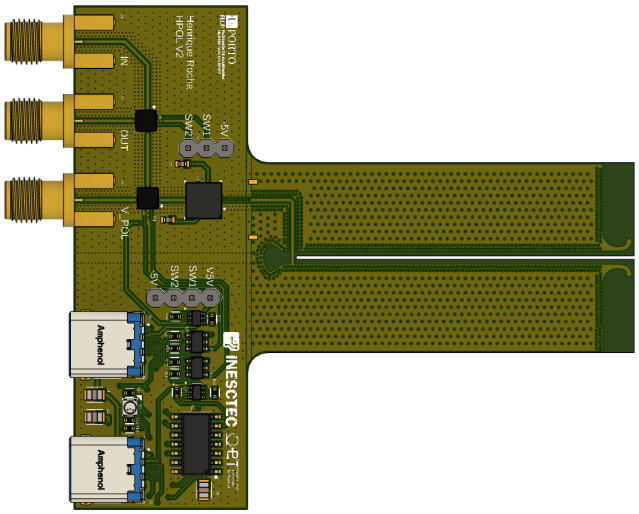

Figure 6.28: Horizontal polarization 3D model.

The layout of the RF switching circuit remained unchanged so that the results obtained in ADS for the dimensions chosen in section 4.3 remain valid. However, the layout of the digital control circuit was adapted, though the schematic remained the same *i.e.* the operation of the circuit was unchanged.

For the other polarization, the workflow was the same. Figure 6.29 shows the 3D model of the PCB.

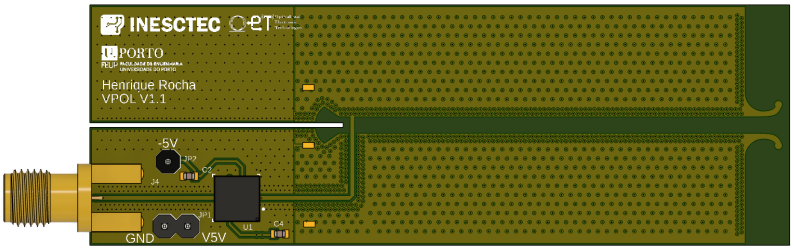

Figure 6.29: Vertical polarization 3D model.

To be able to validate the probe itself, in case something went wrong with the RF switching circuit or the digital control, a third PCB was also manufactured. This probe was also intended to serve as a transmission antenna for the experimental tests, as there was no antenna available at the moment capable of operating on the entire frequency range. In the end, it was not used for this purpose, as it will be explained in section 6.5. To validate the operation of the single probe, other known available antennas can be used, even though on a limited frequency range. If the proper operation is validated in this frequency range, an assumption can be made that the behavior will follow the simulation results for the rest of the frequency range. A 3D model of the antenna in PCB is shown in Figure 6.30.

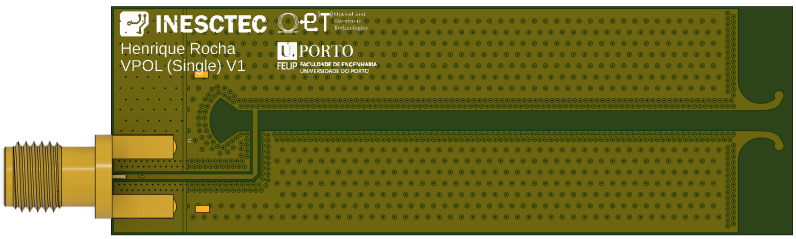

Figure 6.30: Single probe 3D model.

6.5 Experimental Tests

Prior to the experimental tests, the PCBs were assembled. The assembly and soldering process were done in-house, which proved to be a big mistake, as will be demonstrated by the experimental results. In subsection 6.5.1, the assembled PCBs are presented.

6.5.1 PCB Assembly

All PCBs were soldered using solder paste, stencil, and a hot plate. The first PCB to be assembled was the single probe, as illustrated in Figure 6.31. In this case, the end result was satisfactory.

Figure 6.31: Single probe PCB.

The second PCB to be assembled was the vertical polarization, as it had fewer components than the horizontal one. At this stage, everything appeared to be operational. The last PCB to be assembled was the horizontal polarization. Once again, the components appeared to be soldered correctly, as illustrated in Figure 6.32.

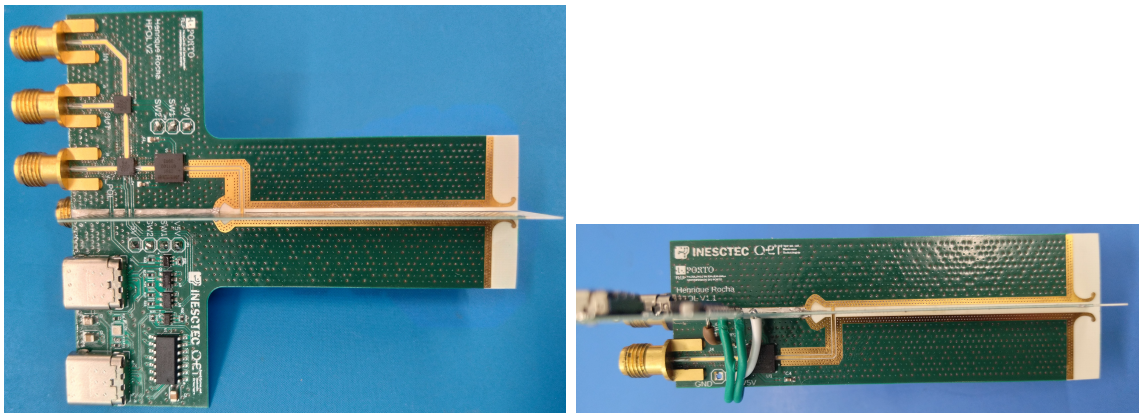

(a) Horizontal polarization.

(b) Vertical polarization.

Figure 6.32: Assembled probe.

After assembly, the DC operating point of the components was tested, and it was confirmed that they were operating as specified in the datasheet. As already mentioned in subsection 4.6.1, the soldering job was not satisfactory as the components did not perform as expected. Bad performance at higher frequencies usually means that the components are poorly soldered. The same problem occurred in the probes as these PCBs were soldered at the same time. Ideally, the final design is only assembled after validating the individual components, such as the switching circuit or the control logic. However, due to delays in ordering and manufacturing the PCBs the decision was made to order them together. This allowed the validation of the individual circuits in the design but assumed that the components were properly soldered, which was not the case. In other words, poorly soldered components mean that the experimental tests are compromised, and the results obtained do not allow the design to be validated.

6.5.2 Measurements

To measure the manufactured design, a far-field anechoic chamber was used. Future work should include measurements of a known antenna using the designed probe (or a future design) in the near-field and then apply near-to-far-field conversion algorithms, which are beyond the scope of this dissertation. Nonetheless, these first measurements served to test the design and PCB assembly.

To be able to fully characterize the manufactured probe, the single probe would be measured from 2 GHz to 18 GHz using the A-INFO LB-20180-SF horn antenna as the known antenna, as it was the one available at the time that best suited the required frequency range. Then if the measurements agreed with the simulation, an assumption would be made that for the rest of the frequency span, the behavior of the probe would be the same as the one simulated. In the end, this method was not used as the measurements were limited to 18 GHz by the coaxial cables installed in the anechoic chamber. Because of the frequency limit imposed by the cables, there was no advantage in using the manufactured probe as a reference, so the horn antenna was kept as a reference for all the measurements. To better visualize the measurement setup used for the

measures, the diagram is shown in Figure 6.33 while in Figure 6.34 a photograph of the single probe and horn antenna mounted inside the anechoic chamber.

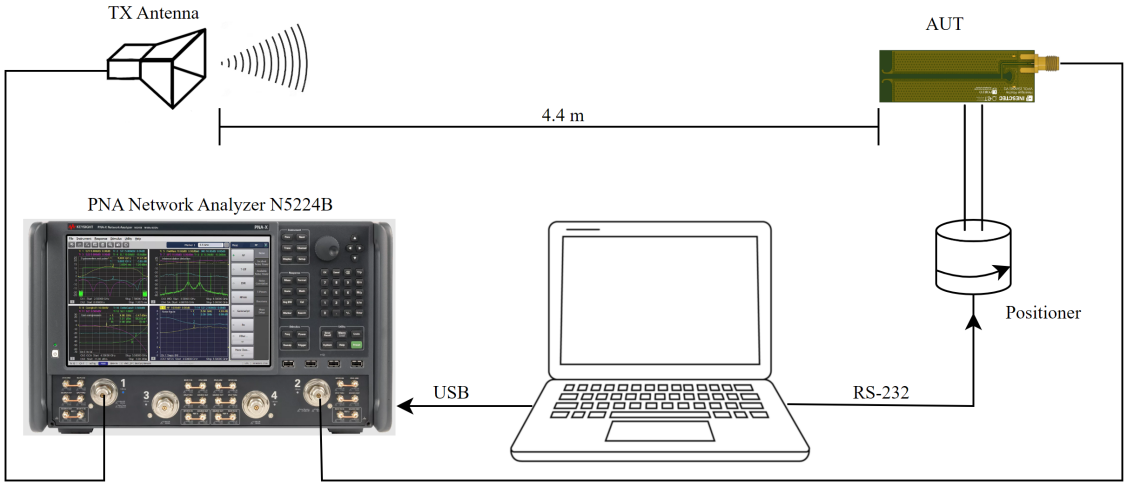

Figure 6.33: Single probe measurement diagram.

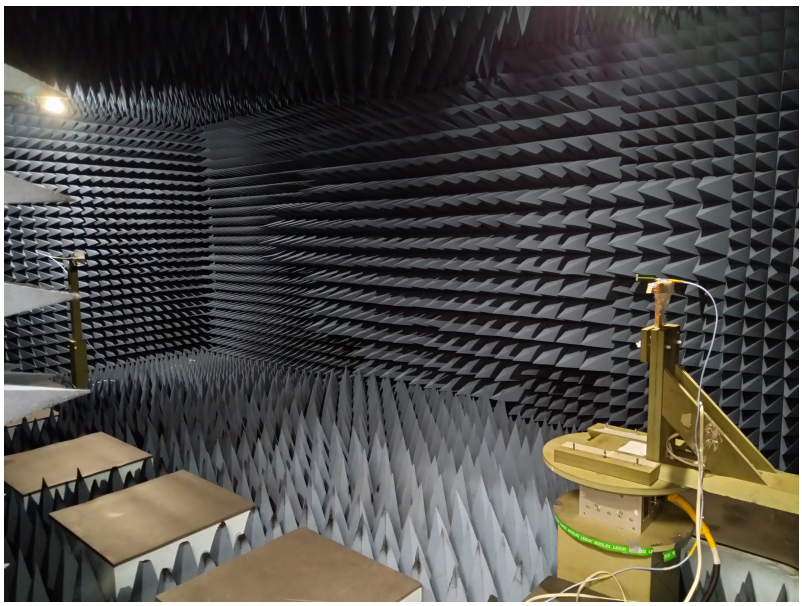

Figure 6.34: Single probe and horn antenna mounted inside the anechoic chamber.

To validate the design, four sets of measurements were performed, two to measure the co-polarized radiation pattern and two to measure the cross-polarization radiation pattern. The S parameters of the system were measured with a step of five degrees for each of the measurements.

To remove the effect of the coaxial cables that connect the network analyzer to the reference antenna and the AUT, a two-port calibration was performed using the Keysight 85052D calibration kit. Although the calibration was performed correctly, the coaxial cables that were installed at the time were damaged. The damages were enough to affect the S_{11} and S_{22} just by moving the cable when the calibration load was installed. As such, the results do not truly portray the

performance of the designed probe. In the future, these measurements should be repeated with suitable cables. Nonetheless, the measurements were performed even though the results may not be the most realistic due to the equipment available. In an attempt to mask the effect of the damaged cables, the RF power on the network analyzer was increased to 15 dBm (the maximum allowed before causing port unlevel), the IF bandwidth was reduced to 10 kHz, the sweep time increased to 200 ms, and the collected data was averaged over eight samples. Despite the efforts, the effects were still noticeable, as seen in the following Figures.

The results for the realized gain measured in front of the antenna are shown in Figure 6.35, where the green and red traces are the simulated data and the blue and orange the measured data, for the co and cross-polarization respectively.

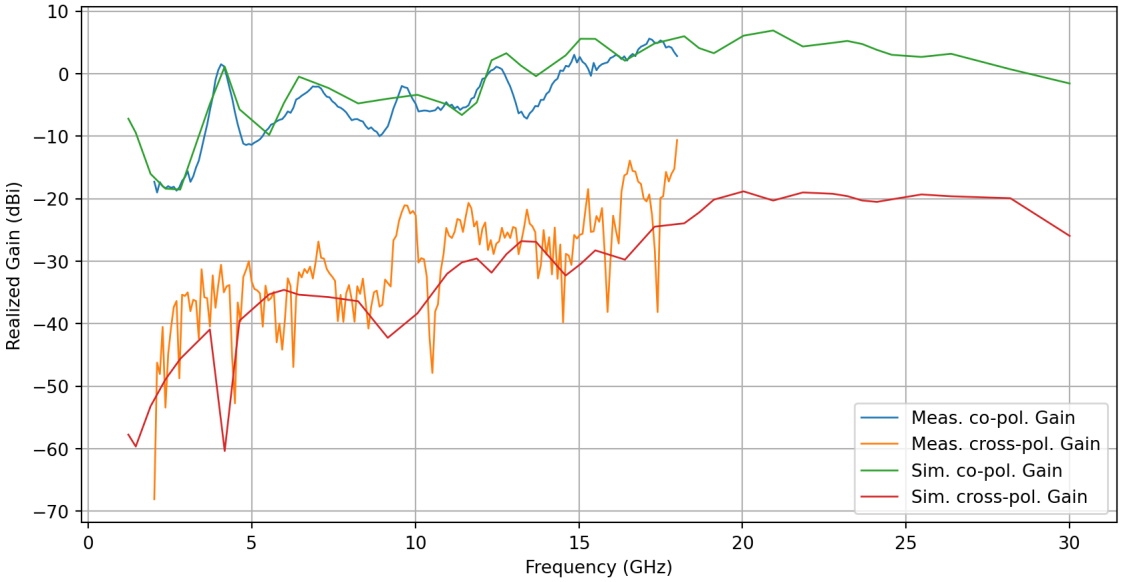

Figure 6.35: Simulated and measured realized gain (dBi) of the single probe in the X axis direction.

As we can see, on the one hand, the co-polarized gain closely follows the simulation, which is expected. On the other hand, the cross-polarization gain loosely follows the simulation, and this is probably caused by the damaged coaxial cables as the received power is lower. As such, the effect of the cable is more noticeable.

The realized gain was computed from the S_{21} measured for the specified direction. To obtain the realized gain, equation (6.2) was used, where G_{AUT} is the realized gain of the AUT, G_f is the gain of the reference antenna, and L_f is the free space loss at frequency f.

$$G_{\text{AUT}} = S_{21} + L_f - G_f \tag{6.2}$$

In this case, the gain of the reference antenna was used as the reflection coefficient met the one specified in the datasheet. As such, the mismatch from the line to the antenna can be discarded.

After measuring the realized gain at the front of the probe, the radiation pattern was measured for 5 GHz and 15 GHz as these are two of the frequencies for which the radiation pattern was

already shown in Figure 6.16, and fall within the operating frequencies of the reference antenna. In this case, only the electric and magnetic planes were measured. Figure 6.36 shows the simulated and measured for the co-polarization radiation pattern for 5 GHz and Figure 6.37 shows the same measurements for 15 GHz.

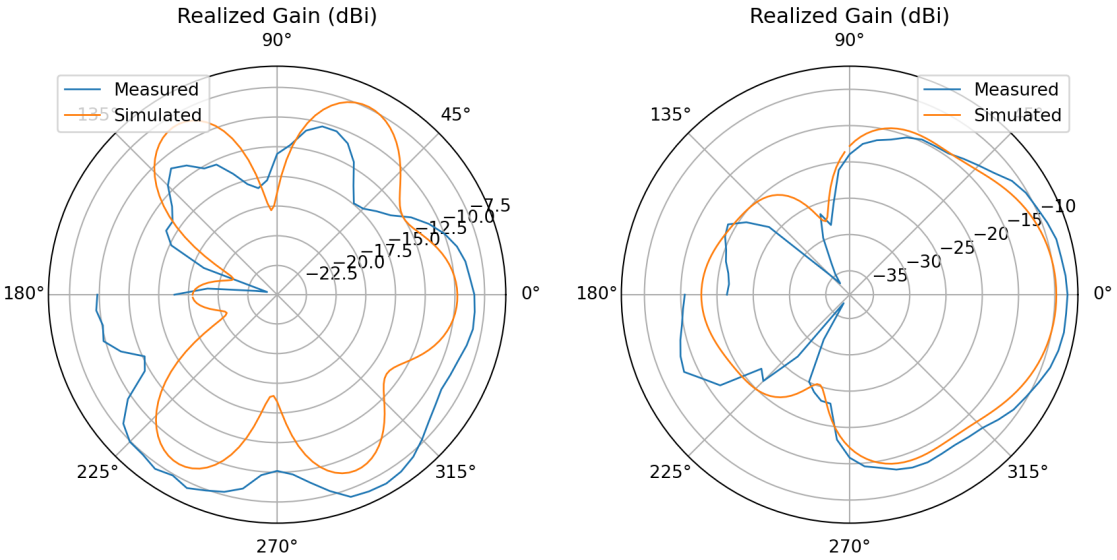

(a) E plane. (b) H plane.

Figure 6.36: Simulated and measured radiation patterns at 5 GHz.

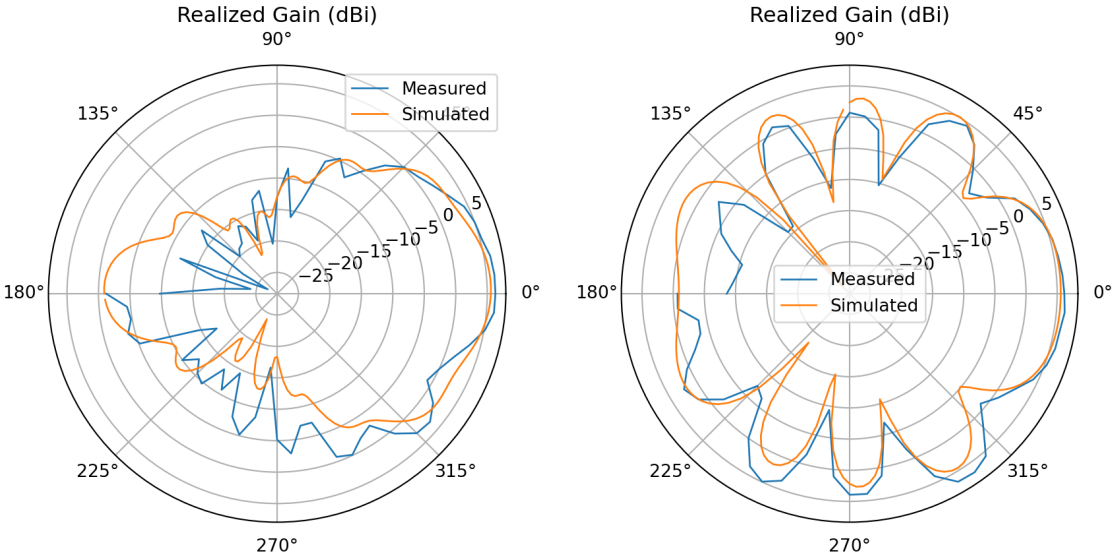

(a) E plane. (b) H plane.

Figure 6.37: Simulated and measured radiation patterns at 15 GHz.

Note that the presented radiation patterns are only for the co-polarized realized gain. The

results for the cross-polarization are not consistent with the simulation, which is probably caused by the damaged cables. As aforementioned, some effort was made to try and mask the effect of the damaged cables, but without success. Moreover, the effect of the cable is prominent in the radiation patterns measured, shown in Figures 6.36 and 6.37. Overall the measurements agree with the simulation results. However, a drift in gain is noticeable throughout the sweep and most pronounced near the start and end of the measurements, *i.e.*, near 180°. This effect is most likely caused by the movement imposed by the positioner, which is rotating the AUT, on the damaged coaxial cable.

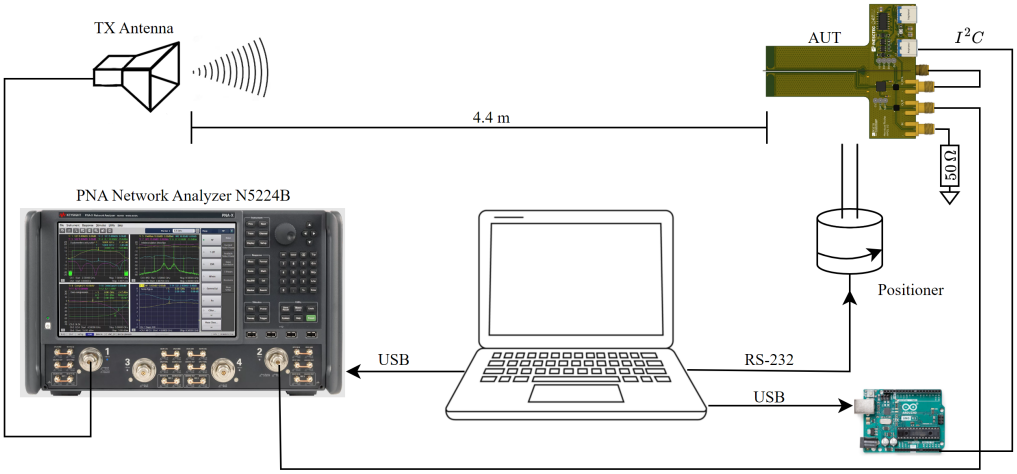

Figure 6.38: Compleate probe measurement diagram.

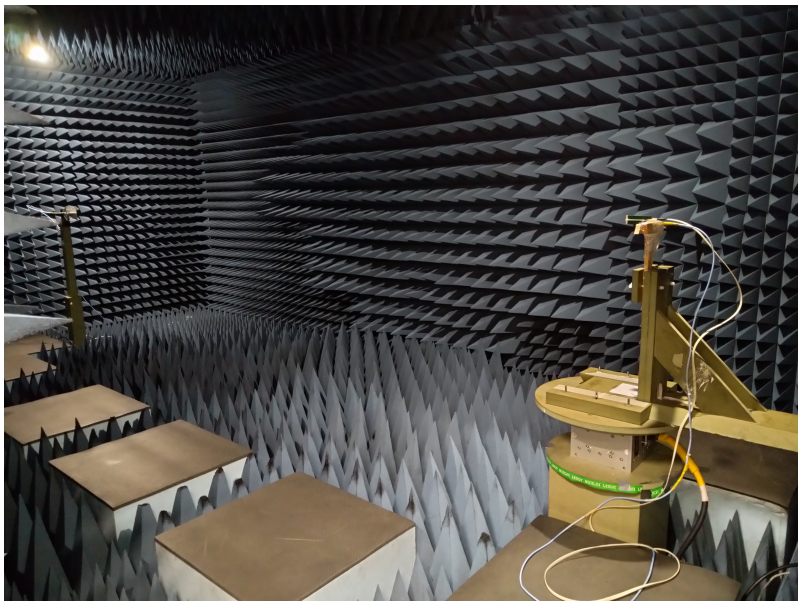

Figure 6.39: Compleate probe and horn antenna mounted inside the anechoic chamber.

After measuring the single probe, the full probe was also measured. To measure the complete probe, the measurement setup required one more controller between the probe and the computer,

as illustrated in the diagram shown in Figure 6.38. Figure 6.39 shows a photograph of the complete probe and horn antenna mounted inside the anechoic chamber.

To fully measure the radiation pattern (E and H planes) of the complete probe, it requires four different antenna positions. In other words, the AUT had to be rotated by ninety degrees once, as well as the reference antenna, by the same amount. With these four measurement setups, it would be possible to measure co and cross-polarization radiation patterns for both polarization and for both E and H planes.

The first measurement performed was for the co-polarization of the horizontal polarization E plane and, at the same time, for the cross-polarization of the vertical polarization H plane. Then the reference antenna was rotated, and two more patterns were measured, and so on until all data was collected. The simulated and measured co and cross-polarization realized gain for the horizontal polarization towards the front of the probe is illustrated in Figure 6.40.

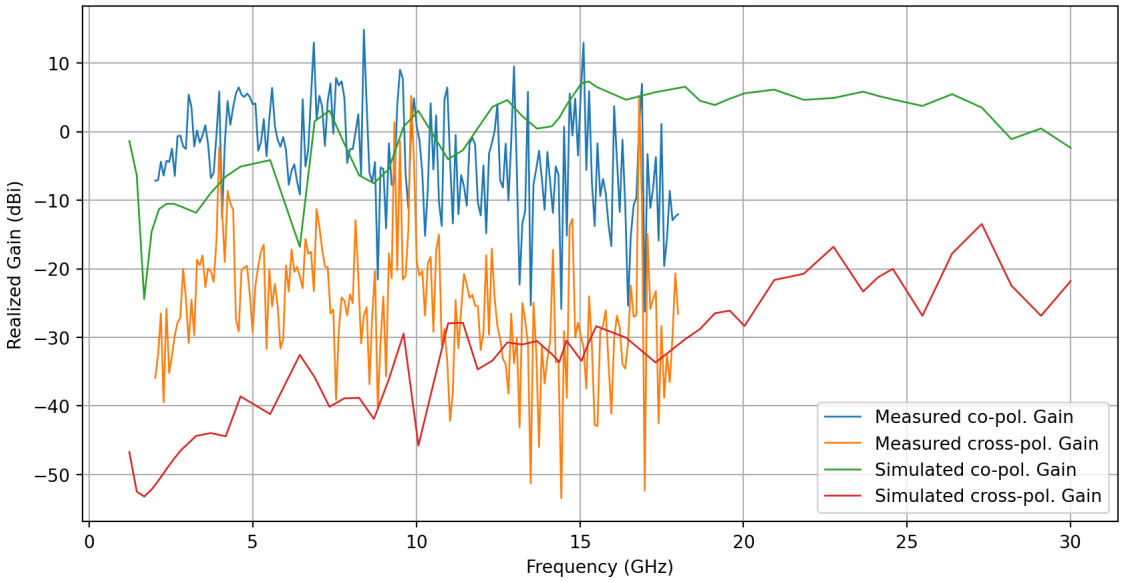

Figure 6.40: Simulated and measured realized gain (dBi) of the complete probe in the X axis direction.

As we can see in the previous plot, the measurements do not agree with the simulation. Moreover, the obtained data appears to be mostly noise, increasing as the frequency increases. The observed behavior is consistent with badly soldered RF components, having a larger influence at greater frequencies. At lower frequencies, we can indeed observe some gain about 8 dB from the expected 12 dB gain of the combined gain of the LNA and the attenuation of the switching circuit. Similar to the single probe, the radiation pattern for 5 GHz and 15 GHz were obtained for the E and H planes as shown in Figures 6.41 and 6.42.

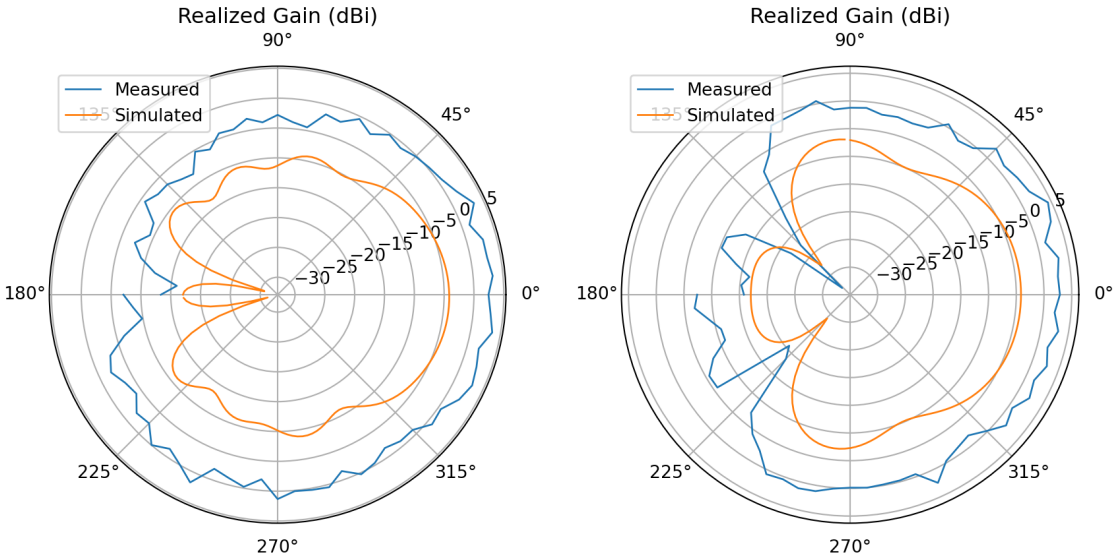

(a) E plane.

(b) H plane.

Figure 6.41: Simulated and measured radiation patterns at 5 GHz.

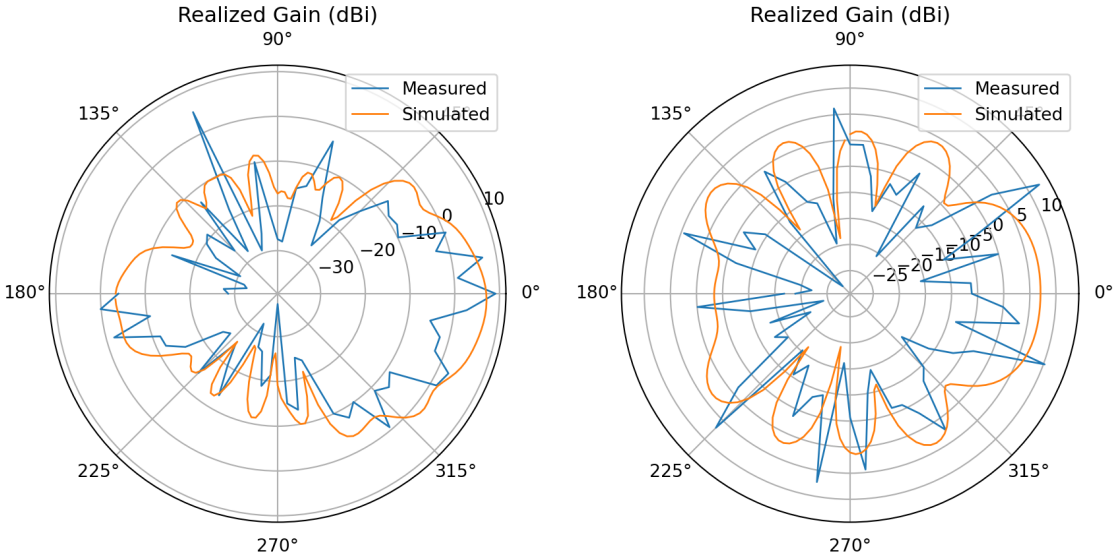

(a) E plane.

(b) H plane.

Figure 6.42: Simulated and measured radiation patterns at 15 GHz.

Once again, the cross-polarization measurements are not presented, as they contain mostly noise, which is visible in Figure 6.40. From the radiation patterns presented, we can clearly understand that for higher frequencies, the performance of the probe is highly degraded, indicating that the LNA and the switches are not properly soldered. It is also possible that the assembled probe with the integrated circuits does not perform as intended, this is less likely as a current

analysis was performed in simulation. Nevertheless, future work is required to better understand the source of the problem. The radiation patterns for the vertical polarization follow the same behavior as the ones present for the horizontal polarization. As such, they will not be presented. However, to confirm that both the switches and LNA are contributing to the problem observed, the vertical polarization was measured by itself. In other words, the network analyzer was directly connected to the output of the LNA of the vertical polarization. Note that during the measurement process, the probe was still fully assembled. In Figure 6.43 you can see that the switching circuit was bypassed.

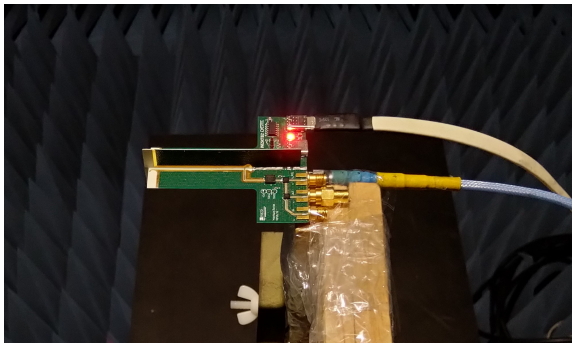

Figure 6.43: Close-up of connection from the vertical polarization to the network analyzer.

The realized gain for both co and cross-polarizations towards the front of the probe is illustrated in Figure 6.44.

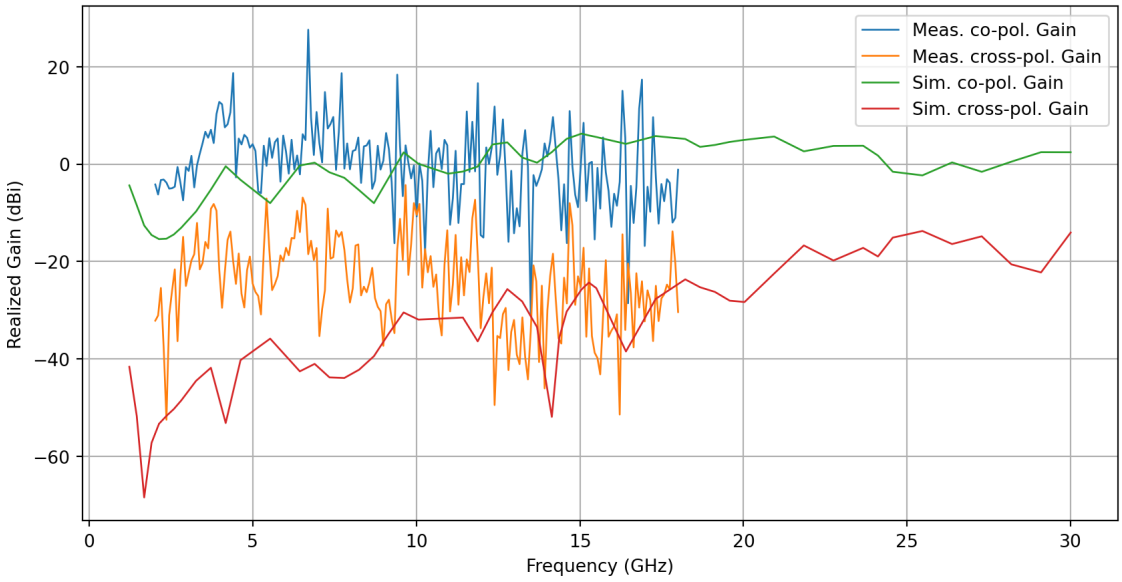

Figure 6.44: Simulated and measured realized gain (dBi) of the vertical polarization with the switches bypassed in the X axis direction.

The results observed are very similar to the ones presented in Figure 6.40, which leads us to conclude that both the LNA and the switches are poorly soldered. Similar behavior is observed in

the tests performed of the individual circuits in section 4.6 and appendix A. The radiation patterns at 5 GHz and 15 GHz obtained for the E and H planes shown in Figures 6.45 and 6.46 show similar results to the ones previously presented for the horizontal polarization.

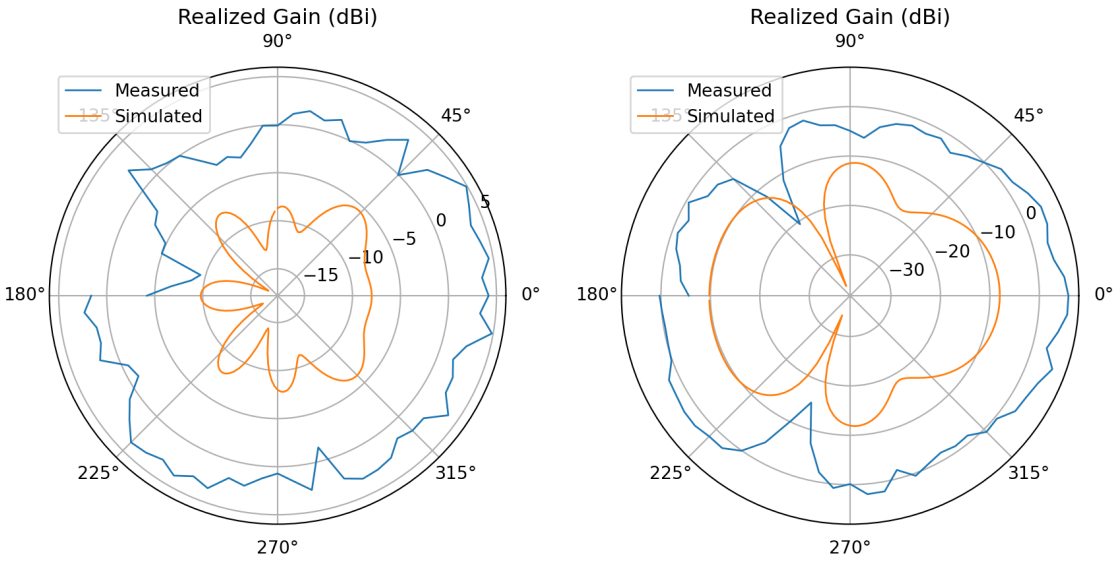

(a) E plane.

(b) H plane.

Figure 6.45: Simulated and measured radiation patterns at 5 GHz.

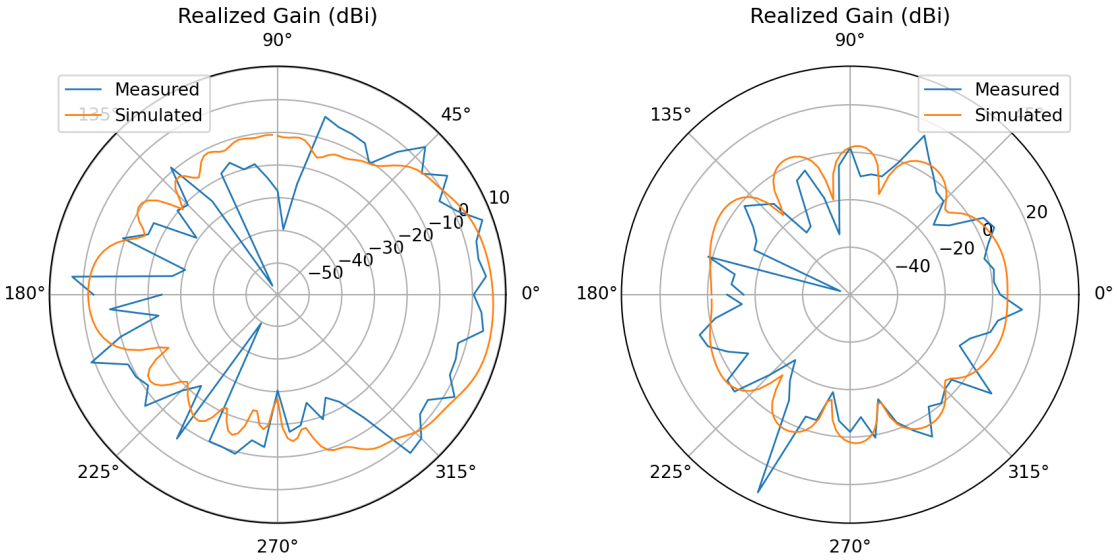

(a) E plane.

(b) H plane.

Figure 6.46: Simulated and measured radiation patterns at 15 GHz.

Similarly to the horizontal polarization that was directly connected to the switching circuit, the isolated vertical polarization also demonstrates the same behavior for higher frequencies. For

5 GHz, we can observe that there is more gain about 13 dB (which matches with the gain in the datasheet of the LNA) when compared to the results of the horizontal polarization. There is also a significant difference in the shape of the measured and simulated radiation pattern, presented in Figure 6.45(a). The effect might be caused by a small misalignment of the horizontal polarization PCB during assembly. However, this was not noticed at the time of measurement. The S parameters of the switching circuit for the RF input, the vertical polarization, and the return loss at the output of the LNA of the complete probe were also measured, yielding similar results to the ones presented in section 4.6 and appendix A, respectively. As such, these will not be presented in this section.

6.6 Sumary

In this chapter, the work performed for the near-field probe design was presented. First, some design requirements were analyzed, as well as the intended design construction. Then, two major designs were evaluated in simulation. The second design included three variations of the feed line. Based on the results obtained and the time frame allocated for this work the CPWG design was selected to be manufactured and tested. After the design was selected a more detailed analysis was performed revealing that some improvements are required as the cross-polarization isolation decayed to unacceptable values at the higher end of the spectrum. Nonetheless, the design was fabricated and measured in an existing far-field anechoic chamber so that it would be possible to confirm the simulation results. Similarly to the RF switching circuit, the probe was also poorly soldered resulting in poor measurement results. So, future work is required not only to improve the design (or evaluate a different one) but to repeat the measurement process using equipment that is not damaged and that is capable of operating in the frequencies of interest. In this case, the measurements were limited in frequency by the coaxial cables available. Although the measurements performed with the assembled dual polarization probe did not allow for the design validation, the measurements performed on the single probe agreed with the simulation in the measured frequency range.

Chapter 7

Chamber Design

7.1 Introduction

The physical chamber design includes two main mechanical systems: structure and positioning systems. The goal was to design an arch capable of forming different radii depending on the antenna's dimensions, of course, limited to the frequency range of the developed probes. Given the time frame allocated for this dissertation, it was impossible to manufacture a prototype of the arch. However, a 3D model of a proof of concept design was created, which will be analyzed in section 7.3. Furthermore, an analysis of the fields in the vicinity of some common antennas was performed to better understand how the antenna structure influences the radiated fields and how they correlate with the region limits explored in section 2.2. Lastly, in section 7.5, the system diagram is presented, which includes the developed components, as well as a description of how they interact.

7.2 Region Analysis

As previously mentioned, in different regions that surround an antenna, the reactive power (energy exchanged between the antenna and the surroundings per unit of time) and active power (energy radiated per unit of time) have different strengths. To better understand the behavior of different antennas, some simulations were performed in HFSS to plot the reactive and active power of a given antenna using the Poynting vector. The wave impedance was also plotted. Both the Poynting vector, real and imaginary components, and the wave impedance were plotted in the direction of greater radiation. Knowing that in air, the wave impedance is approximately $120\pi \approx 377\,\Omega$ the far-field can be seen as the region where the wave impedance is close to the wave impedance at infinity. The antennas chosen for the simulations were an electric and magnetic (loop) dipole, and a patch.

In the following subsections, the plots are generated from mathematical expressions defined in HFSS. One expression computes the Poynting vector $\vec{S}$ by calculating the vector product of the electric and the magnetic fields $\vec{S} = \vec{E} \times \vec{H}$, this is computed automatically by HFSS. The previous

expression is subdivided into the real and imaginary parts of the Poynting vector corresponding to the radiated and reactive power, respectively. The other expression divides the electric field by the magnetic field to obtain the wave impedance in the direction of maximum radiation.

7.2.1 Electric Dipole

The dipole antenna was chosen to be the first to be analyzed as it is the one used by Balanis [3] in the computations that are at the base for equations (2.13), (2.19) and (2.20). The simulation model used can be seen in Figure 7.1, and in Figure 7.2, the results obtained after the simulation.

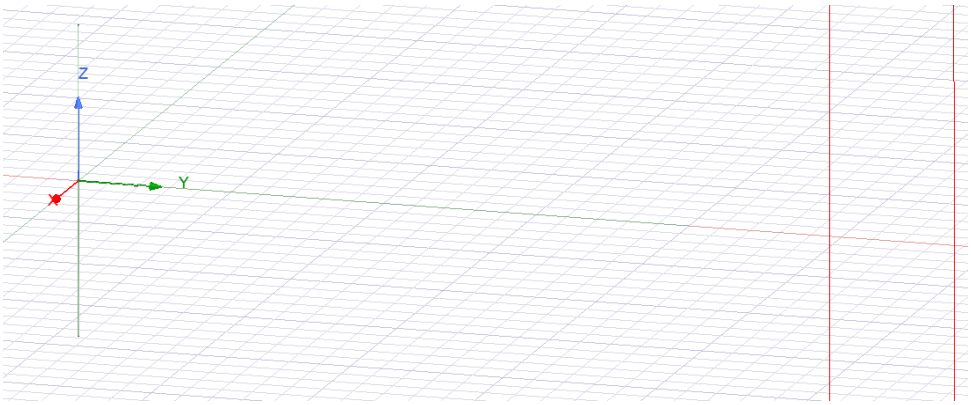

Figure 7.1: Electric dipole simulation model.

Note that the reactive near-field, the region closest to the antenna, was considered to end when the reactive power is below 10 % of its initial value, assuming that for this amount the effect it has in the measurements is negligible. Considering that the antenna used is a half-wavelength dipole and that the operating frequency is 300 MHz, then the boundary between reactive near-field and radiating near-field is approximately 40 mm away from the antenna, matching closely to the distance where the reactive power gets below 10 % of its highest value. The computed far-field boundary is situated 500 mm away from the antenna, where the reactive power at this distance is practically zero.

When considering the wave impedance, the curve follows the expected behavior converging to $120\pi\,\Omega$ with increasing distance to the antenna. As expected at the computed far-field boundary, the wave impedance is slightly below the $120\pi\,\Omega$.

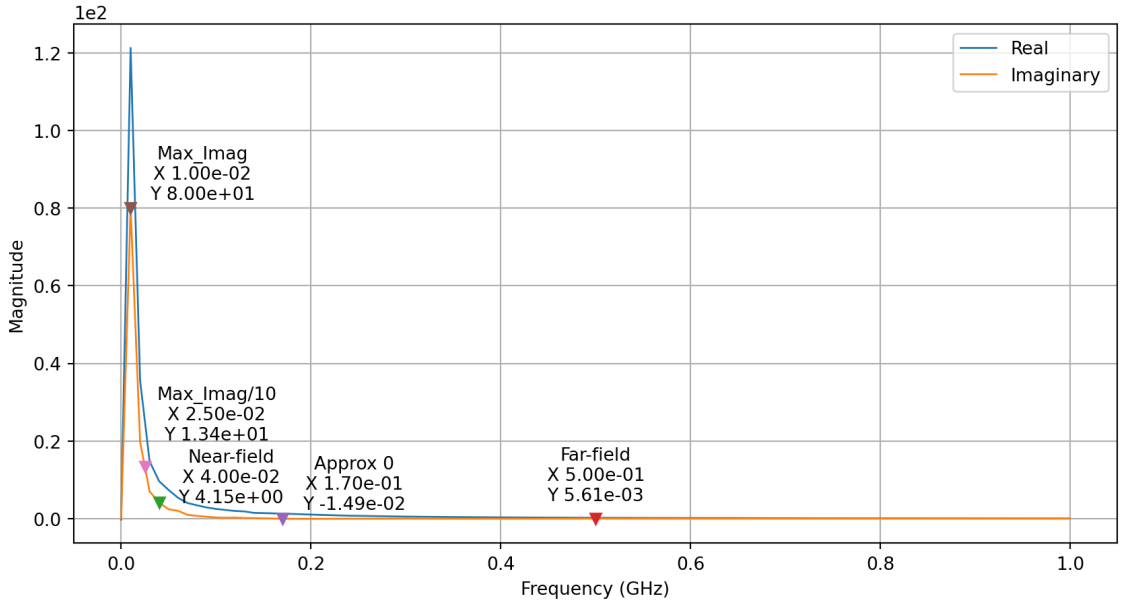

(a) Poynting vector real and imaginary components.

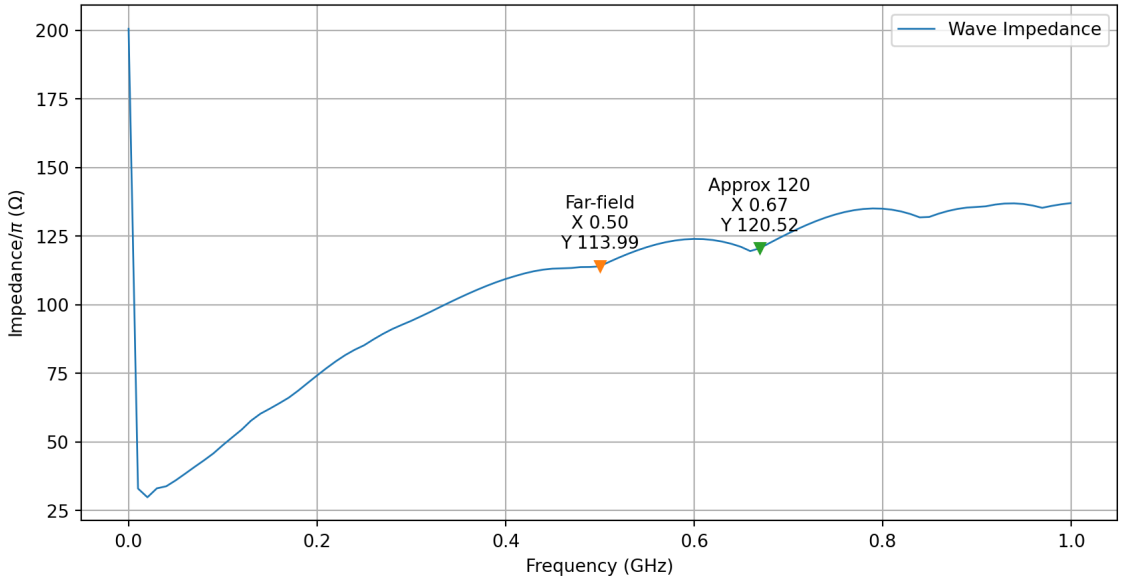

(b) Wave impedance.

Figure 7.2: Electric dipole simulation results.

7.2.2 Magnetic Dipole

The magnetic dipole antenna is a loop of wire that can take more than one shape, for example, circular, square, triangular, elliptical, ... The circular shape loop antenna was chosen for its simplicity. The computed radius of the antenna is $r = \frac{L}{2\pi}$, where $L \approx 1\,\text{m}$, for an operating frequency of 300 MHz. Furthermore, the conductor used for the antenna has a 1 mm radius, and the feed gap

was set at 1 mm also. The simulation model used is depicted in Figure 7.4, and in Figure 7.3, the results obtained after the simulation.

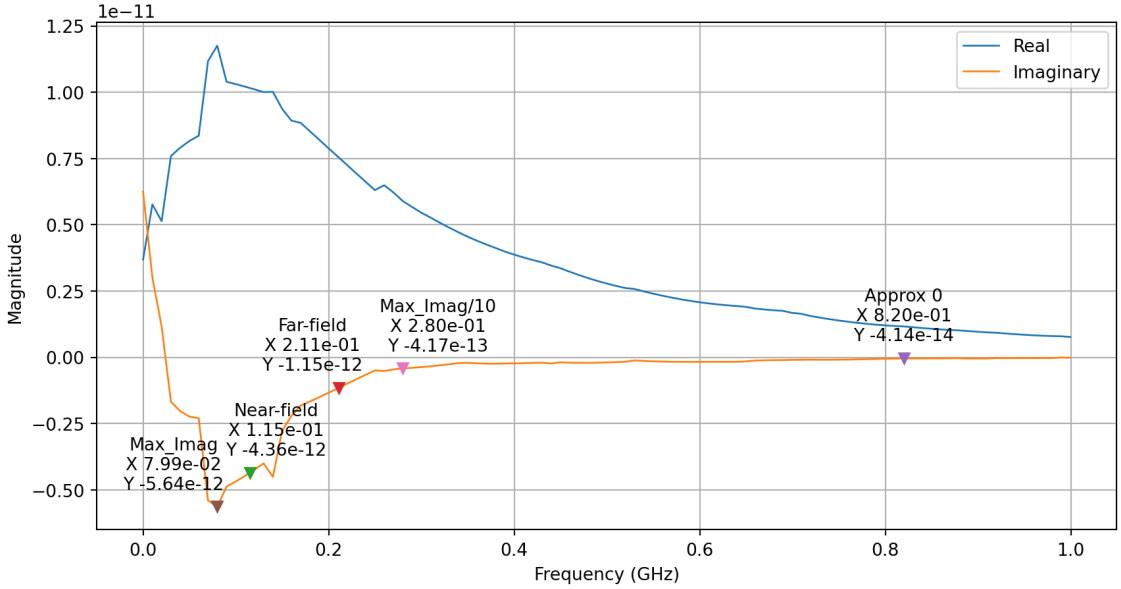

(a) Poynting vector real and imaginary components.

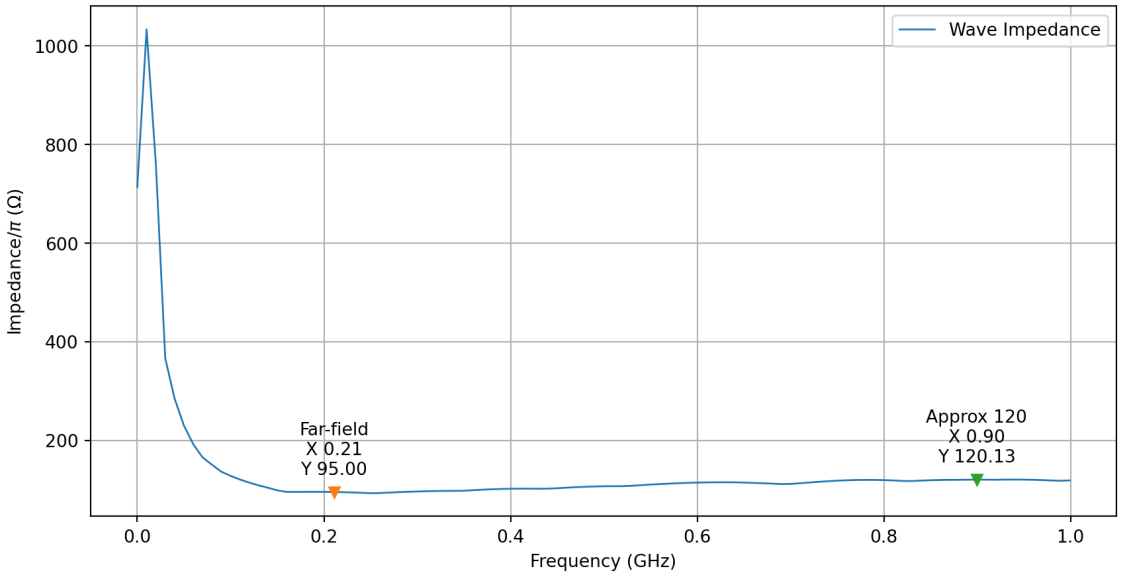

(b) Wave impedance.

Figure 7.3: Magnetic dipole simulation results.

By comparing the results obtained for the dipole antenna and the loop antenna, we can observe that the power and wave impedance behavior differ considerably from one antenna to the other. Furthermore, we can also observe that the wave impedance converges to 120π Ω faster than the previous antenna. Note that the antenna dimensions are different, as such, the near and far-filed distances are also different, as indicated by the cursors in the plots.

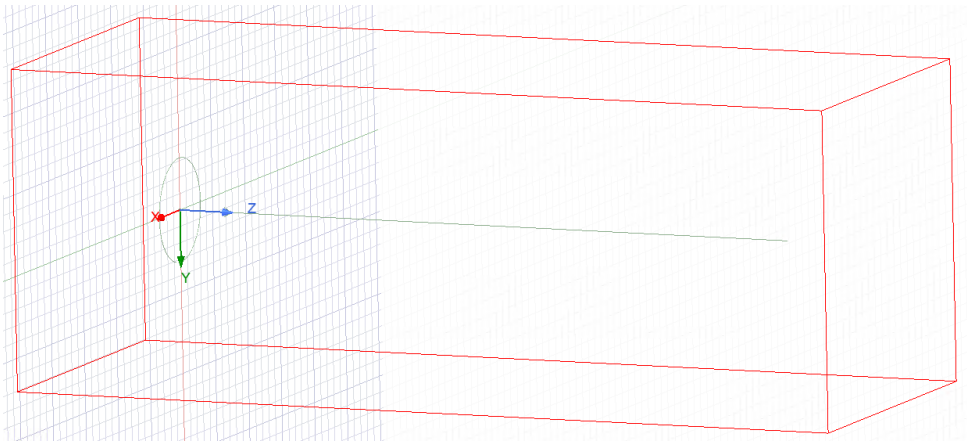

Figure 7.4: Magnetic dipole simulation model.

7.2.3 Patch

As a complementary analysis, a square patch antenna fed by a short microstrip line was used. The antenna was sized, similarly to the previous cases, to operate at 300 MHz. The substrate used in the model is 1 mm thick ($h = 1\,\text{mm}$) FR4 with $\varepsilon_r = 4.4$. The microstrip was designed to match 50 Ω, which results in a line width $L_W = 2\,\text{mm}$ and an arbitrary length of $L_L = 25\,\text{mm}$. The dimensions obtained for the patch were $L = 304.1\,\text{mm}$ and $W = 238.2\,\text{mm}$. For the copper height $t = 35\,\mu\text{m}$ was used. The described dimensions are associated with the variables shown in Figure 7.5.

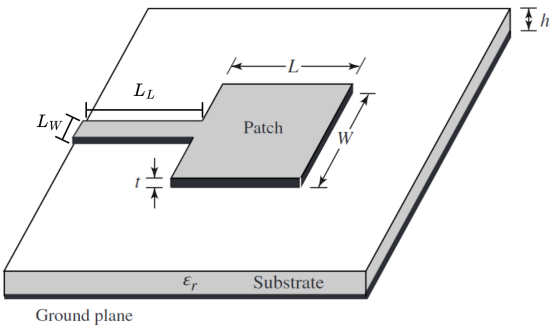

Figure 7.5: Patch antenna model (adapted from [3, p.5]).

The simulation model used is shown in Figure 7.7, and in Figure 7.6, the results obtained after the simulation. Similarly to the last analysis, the results correspond to the direction of greater radiation.

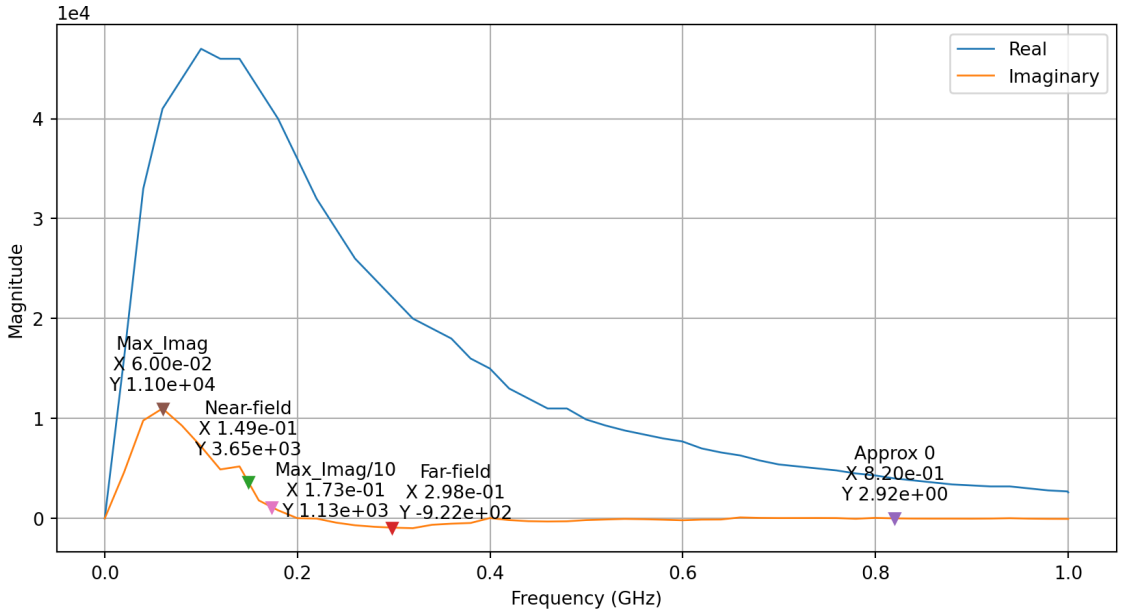

(a) Poynting vector real and imaginary components.

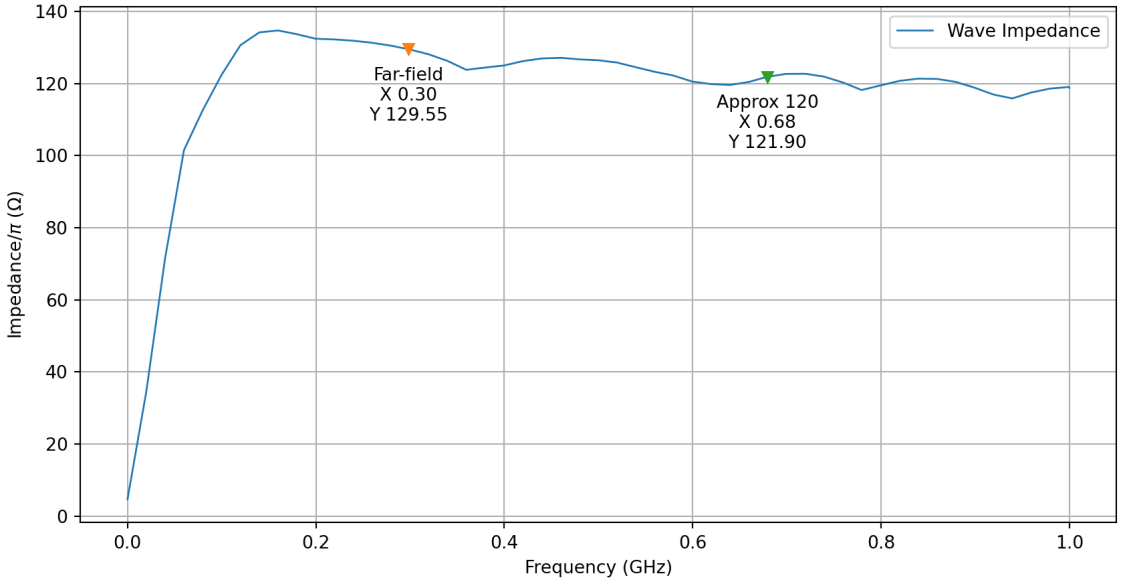

(b) Wave impedance.

Figure 7.6: Patch antenna simulation results.

Once again, the behavior of the wave impedance and the active and reactive power is different from the previous antennas. In this case, considering that the diagonal is the larger dimension of the antenna [3, p.161], the distances for the near and far-field were updated in the plots. By comparing the results obtained for the dipole antenna and the loop antenna, we can observe that the wave impedance converges to 120π Ω faster than the previous antennas and that the power distribution is also different.

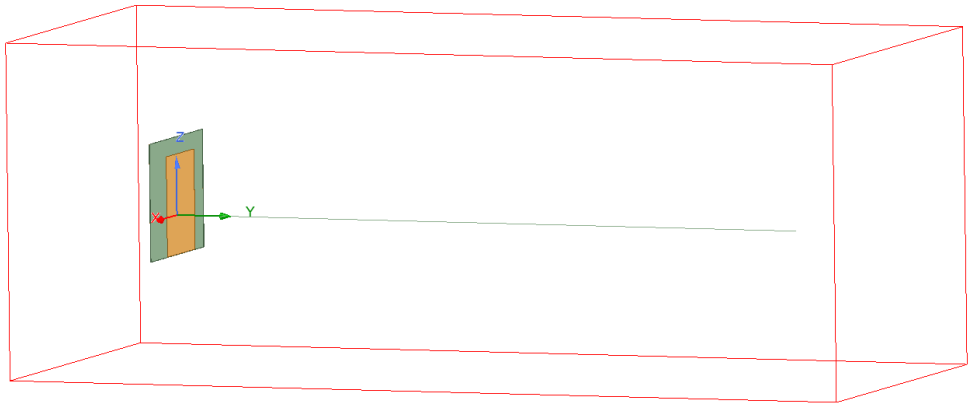

Figure 7.7: Patch antenna simulation model.

These results show that before measuring an antenna, the reactive near-field region dimension should be checked so that it does not extend up to the probe antennas.

7.3 Structure

As a proof of concept design, a measurement arch model with a usable radius of 0.6 m was simulated. Figure 7.8 shows the 3D model used for the simulations.

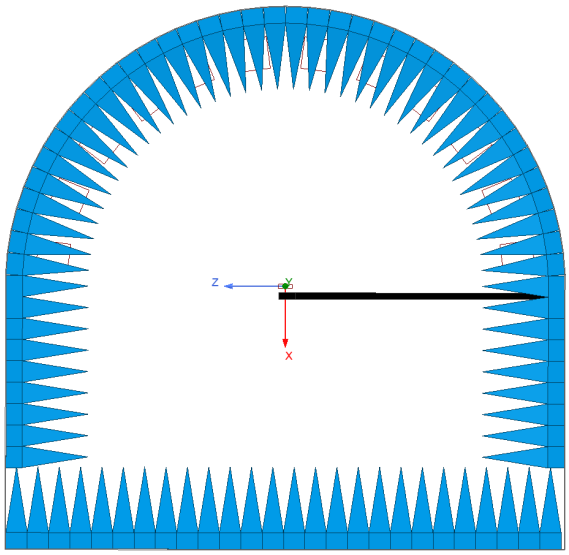

Figure 7.8: Measurement structure simulation model.

The model used for simulation is intended to be as simple as possible, to reduce simulation execution time while maintaining essential detail like the absorber's shape and the presence of the AUT support, which is connected to the positioner. The goal of the proposed design was to have a measurement arch supported on its ends. A connection plate at the bottom was also included to improve the structure's mechanical stability. To cover the metal components of the structure, absorber material (colored blue) was placed all around the perimeter of the structure.

The absorber material selected was the polyurethane pyramidal absorber with a pyramid height of 200 mm, totaling 250 mm, including the size of the base. This absorber material, according to the manufacturer, has a minimum reflectivity of −25 dB at the 0.5 GHz [24]. Because this material did not exist in the simulation library, a new one was added using the measurements performed in [8, p.100] as a dataset for the material. Ideally, new measurements of the material should be performed at the simulated frequencies. However, due to time constraints, this was not possible.

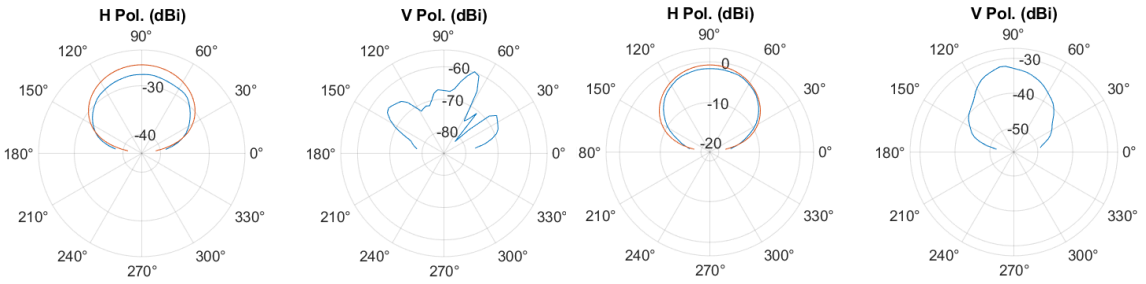

(a) Realized gain at 1 GHz.

(b) Realized gain at 5 GHz.

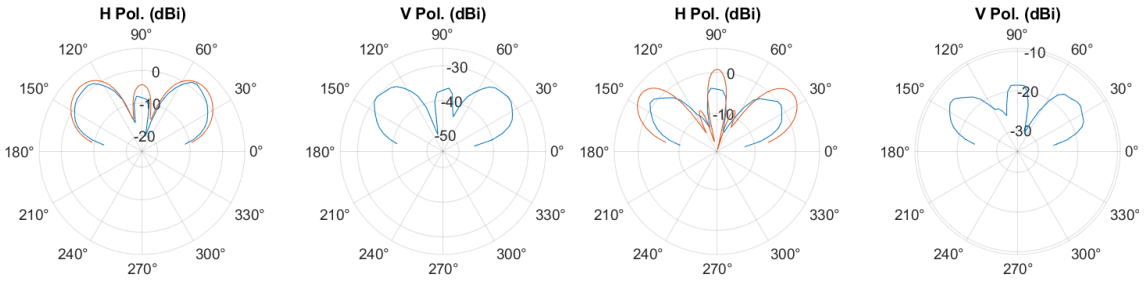

(c) Realized gain at 15 GHz.

(d) Realized gain at 25 GHz.

Figure 7.9: Simulated and measured (using SBR+) radiation pattern using horizontal polarization.

For the chosen arch radius, the number of probes that could be fitted, while leaving some space between them to fit absorber material, was twelve. Note that the number chosen was arbitrary. As such, future work should include an analysis of the minimum distance required between probes to provide satisfactory results. Given that the mentioned analysis was not performed, absorber material was left between probes to reduce mutual coupling, which was kept below −60 dB. In the model, the probes are represented with a red box.

As previously mentioned, the simulations were performed in the far-field. This was done not only because the near-to-far-field algorithms are beyond the scope of this dissertation but also because the probes were experimentally measured in the far-field. So this simulation aims to prove that the design can produce accurate data. Note that, in the SBR+ simulation, the received power is measured at the antenna port, so there is no effect of the RF switching circuit and cables considered. Nevertheless, the S parameters of the system were measured to ensure that the probes performed as expected.

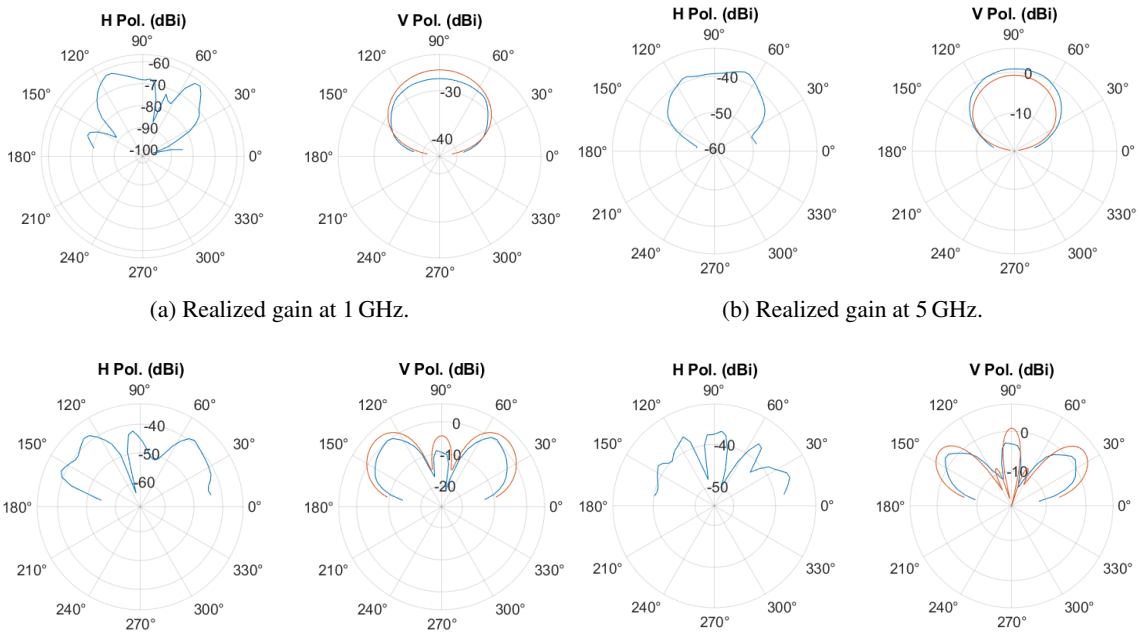

(a) Realized gain at 1 GHz.

(b) Realized gain at 5 GHz.

(c) Realized gain at 15 GHz.

(d) Realized gain at 25 GHz.

Figure 7.10: Simulated and measured (using SBR+) radiation pattern using vertical polarization.

To test the system, a 30 mm long dipole antenna was placed at the center of the chamber, and an SBR+ simulation was performed. The simulation was performed for 1, 5, 15, and 25 GHz, while keeping the dipole the same size. After exporting the measured S parameters, the data was processed in Matlab. Given the reduced number of probes, the data points were oversampled by a factor of four and then interpolated. The transmission S parameter between the AUT and probe n is given by $S_{n,\mathrm{AUT}}$ are used to plot the radiation pattern of the AUT using equation (6.2) for both horizontal and vertical polarization. Figure 7.9 shows a radiation diagram of the AUT for the aforementioned frequencies using the horizontal polarization of the AUT, while in Figure 7.10 the data collected using the vertical polarization is shown.

By comparing the results with the expected radiation pattern (plotted in orange), we can say that the system is working as intended. We can observe that the results obtained from the SBR+ simulation do not fully match the expected gain. However, the shape of the pattern obtained closely follows the expected for both polarizations. The difference in measured gain is not fully understood, so future work is required on this topic. We can also observe that the effect of the reduced cross-polarization of the vertical polarization is clearly noticeable when performing measurements with the horizontal polarization. This is more pronounced at 25 GHz, where the probe has reduced cross-polarization isolation as illustrated by Figure 6.21. As such, a redesign is required to try and correct the aforementioned issues. Regarding the modeled AUT support, there is no noticeable difference in the radiation pattern. If the support were to affect the measurements, an asymmetry in the radiation pattern would be expected, which is not noticeable.

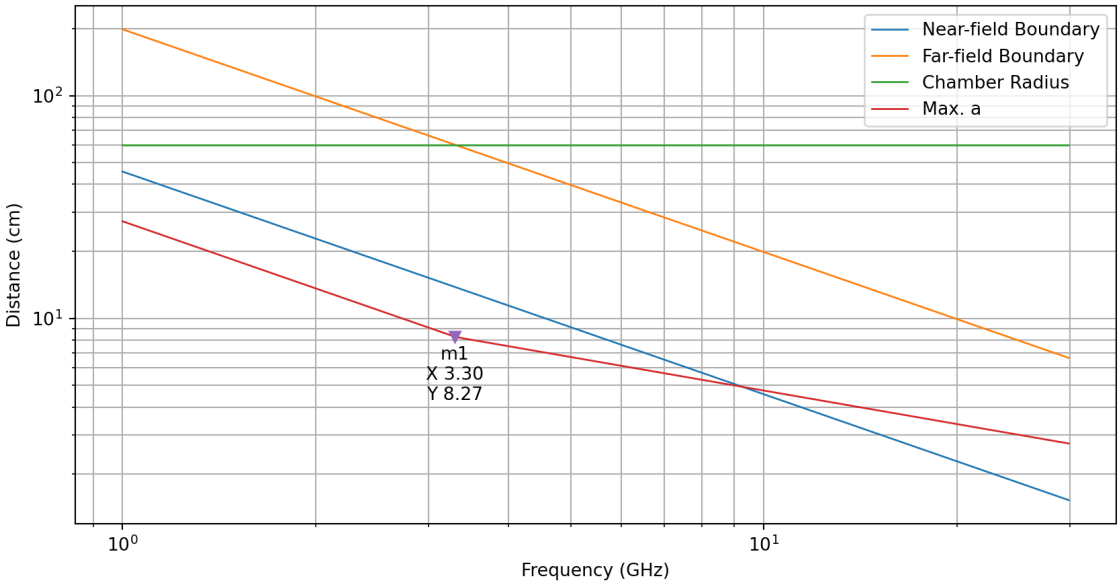

Figure 7.11: Near and far field boundaries for maximum sphere radius surrounding the AUT considering a chamber radius of 0.6 m with twelve probes.

To better understand how the number of probes, the size of the AUT, and the operating frequency affected the system, an analysis was performed based on the criteria specified in [3, p.995], where it is described that for the algorithms to reliably convert the near-to-far-field information, a maximum spacing between samples must be met. For spherical conversion, the one intended for this design, the maximum angle on the azimuth plane is given by equation (7.1), where λ represents the wavelength and a the radius of the smallest sphere that surrounds the antenna.

$$\Delta\phi = \frac{\lambda}{2(a+\lambda)} \tag{7.1}$$

On the elevation plane, the maximum sampling angle is equal to the angle defined for the azimuth plane, as illustrated by equation (7.2).

$$\Delta\theta = \frac{\lambda}{2(a+\lambda)} \tag{7.2}$$

With this information, and considering a usable radius of 0.6 m (measured from the tip of the absorbers to the center of the chamber), a plot can be made where the maximum sphere radius a is shown based on the maximum sampling angle and the fact that the probes must be outside the reactive near-filed region. In the plot, shown in Figure 7.11, the reactive near-field and the far-field boundary were considered to be at a distance defined in equations (2.20) and (2.13).

From the previous plot, we can conclude that up to 3.3 GHz, the limiting factor is the maximum sampling angle defined in equation (7.2). Above 3.3 GHz the limiting factor becomes the far-field, as in this frequency range, the space between probes no longer meets the maximum sampling angle specified in equation (7.2). However, the measurements can be performed in the far-field as there is no longer a need to apply the conversion algorithms.

7.4 Postitioner

The positioning system developed only covers a certain range of antennas, limited by its weight-carrying capability. The proposed solution was designed to support antennas up to a quarter of a kilogram, which, in most cases, suffices. As previously explained, the positioning system should be as transparent as possible to the radiation emitted to the antenna so that it does not interfere with the measurements being taken. The goal was to design the positioner so that it could be 3D printed. Having analyzed different 3D printing materials, PLA was an excellent candidate to build the positioner. Figure 7.12 shows the positioner arm 3D model. Considering that the positioner can be mounted horizontally, additional support should be placed closer to the AUT. However, further experimentation is still required.

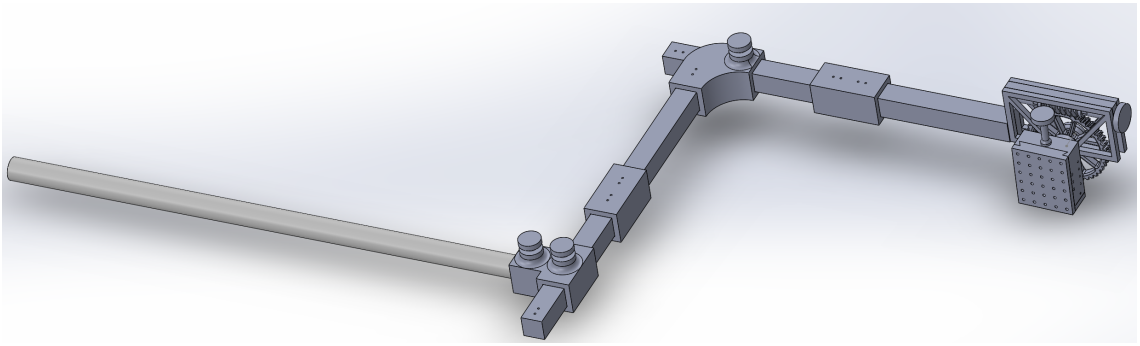

Figure 7.12: Positioner 3D model.

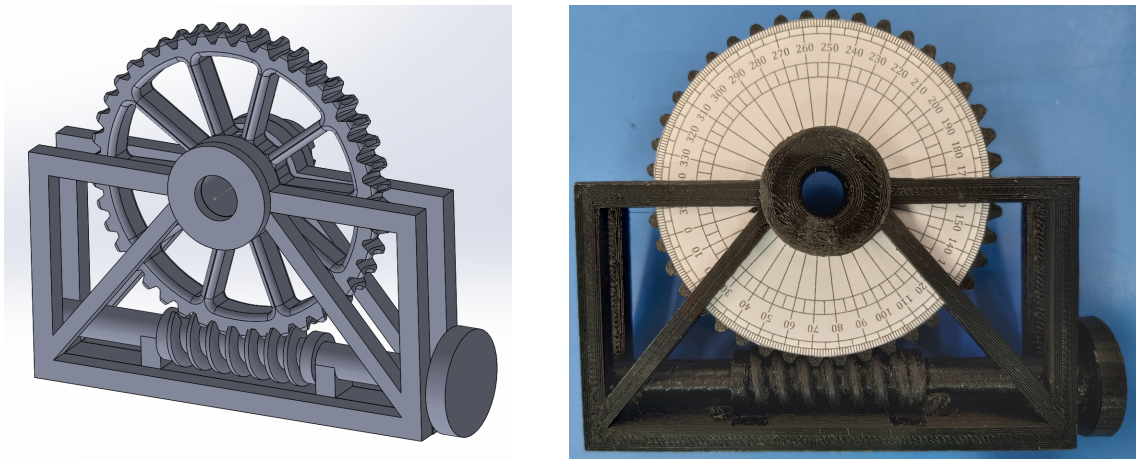

(a) 3D model.

(b) Printed assembly.

Figure 7.13: Postitioner θ adjustment.

Due to the constraints imposed by the near-to-far-field conversion algorithms (equation (7.2)), the defined arch radius could only measure in the near-field up to 3.3 GHz due to the maximum angle required. A manual adjustment in θ was added to the positioner to work around this problem. Although manual adjustments in the measurement setup may introduce errors, this solution was

seen as a good compromise between design simplicity and measurement error. The proposed solution is shown in Figure 7.13.

The design uses a worm gear to increase the precision of the rotation of the AUT. The increase in accuracy is due to the different radii of the gears, in this case, a 45:1 gear ratio. In other words, for each rotation of the input shaft (connected to the smaller gear), the output shaft (larger gear) rotates 8°. A critical advantage of this type of gear mesh is that the output gear cannot drive the input gear, essentialy acting as a self-locking mechanism. Furthermore, to reduce the measurement error, the gear assembly was tuned to minimize the backlash.

With the θ adjustment mechanism designed, the AUT adjustment mechanism was designed to connect to the output gear shaft. This mechanism was adapted from a previously developed model for a similar purpose. The design is inspired by the working platform of a milling machine, as illustrated by Figure 7.14.

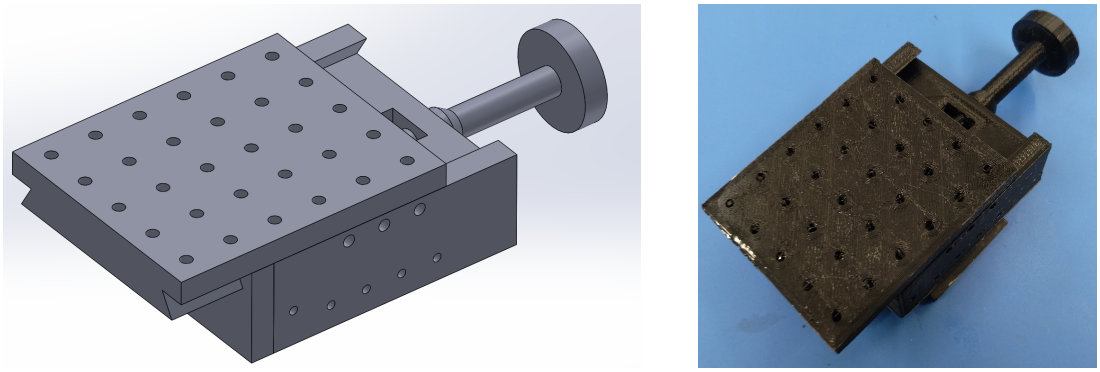

(a) 3D Model. (b) Printed mechanism.

Figure 7.14: AUT adjustment mechanism.

This design was also tuned to reduce the backlash to close to zero. This assembly allows the user to adjust the antenna's phase center to the center of rotation of the main positioner shaft.

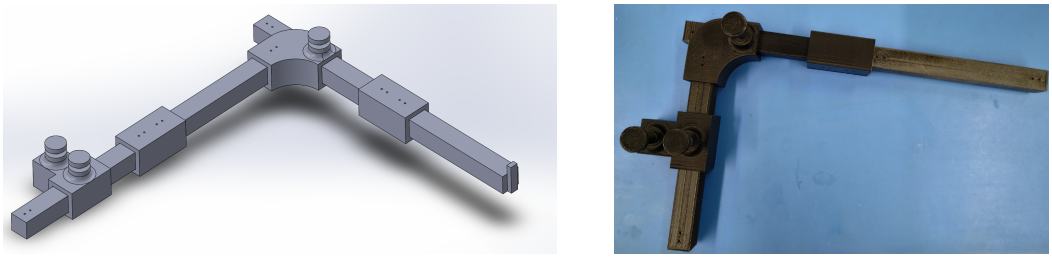

(a) 3D model. (b) Printed mechanism.

Figure 7.15: Arm adjustment mechanism.

Two arms connected the components mentioned above to the main positioner shaft. These were sized to allow for the biggest antenna that could be measured using the proof of concept radius. Based on the computations performed, this antenna has to fit inside a sphere with a 30 cm

radius, so 30 cm long arms were designed. Due to building plate constraints, the components were separated in half, this also allowed the arm's length to be reduced to half for a more sturdy assembly. The final design is visible in Figure 7.15.

Furthermore, this design also allows the AUT's phase center to be adjusted to the center of the chamber. Like the other components, the arms were fine-tuned to guarantee the tightest fitting possible, reducing measurement error and increasing stability.

Note that there is more than one possible solution to this problem. For example, the orientation of the positioning system could be changed to work vertically. If the positioner arm was placed vertically, its weight-carrying capabilities would increase. However, the probes would only have access to the top part of the antenna, as the antenna would rotate in the horizontal plane. In other words, only half of the radiation pattern could be analyzed, which may be desired depending on the antenna being measured. For example, when measuring a horn antenna, there is little to no radiation emitted from the back side, so representing this part of the radiation pattern may not be of great interest. So there is a compromise between measurement capabilities, positioner orientation and weight-carrying capabilities, assuming that the probes do not fully surround the AUT, which is the case for the proposed design.

7.5 System Diagram

To better understand how the designed components interact, Figure 7.16 shows a diagram of the complete system.

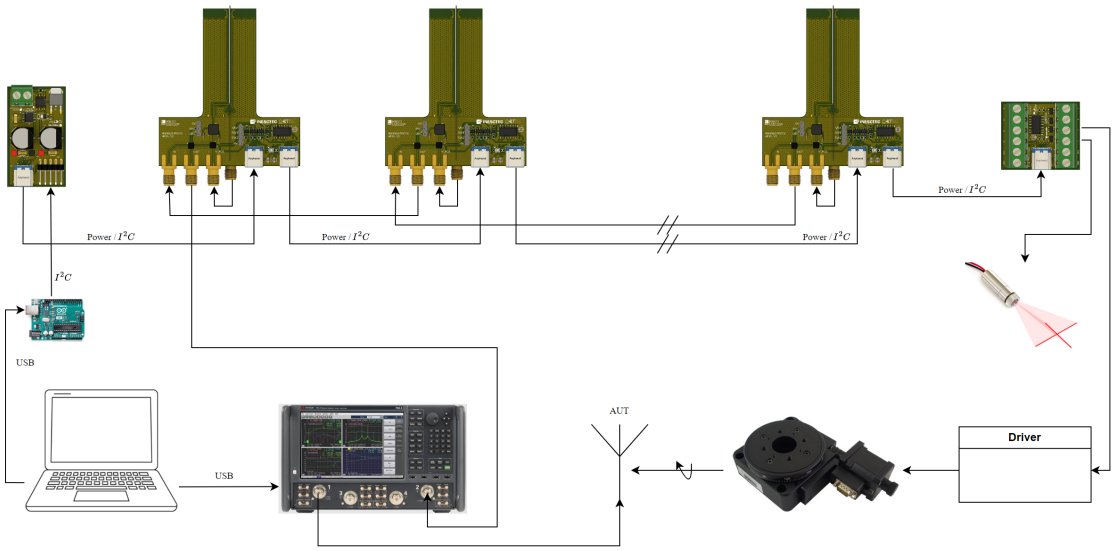

Figure 7.16: System diagram.

The system is controlled by the computer, and every other device follows the commands given by it.

On the one hand, to acquire data, the computer communicates with the VNA via USB using the Virtual Instrument Software Architecture (VISA) communication protocol. The VNA is then

connected to the AUT (transmitter antenna) and to the last probe in the chain (receiver antennas), receiving the RF signal to then be analyzed by the computer. Note that because the system includes a RF switching circuit in each probe, the VNA can receive the signal from any of the probes, from both polarizations.

On the other hand, to control the position of the antenna and enable the probe that is receiving the signal, the computer communicates with a microcontroller (Arduino UNO, in this case) via USB. The microcontroller then translates the received USB command to I^2C. As the probes are all connected to the same I^2C bus, the microcontroller can reach any of them, as each probe is assigned a different address when it is programmed. The IO expander is also connected to the same I^2C bus. As such, it is also controlled by the Arduino. The objective of this last device is to be able to control the LASER pointer used to align the phase center of the AUT with the center of the chamber and to send commands to the driver of the positioning system.

The power supply board is located between the microcontroller and the probes, providing not only proper voltage for the electrics used, a connection from the USB-C connector to the microcontroller and some protection against user error, such as reverse polarity protection. There are five exposed pins: GND, SCL/SCK, SDA/MOSI, MISO, and RESET. Where ground (GND) is the reference pin, and the others are used both for programming and communication.

Regarding the probe connections, the communication and power are connected in parallel throughout all the devices. The RF signal is connected from the first probe in the chain (further away from the VNA) down to the last probe (the one connected to the VNA) in the chain using the integrated switching circuit. As already mentioned, with this approach, the signal is attenuated every time it goes through a switch, which is a limitation of the system. To compensate for the attenuation caused by the switches, an extra LNA can be placed in the signal path to reamplify the signal, as already mentioned in section 4.2.2. The developed PCB, analyzed in appendix A does not include the control circuit required to be installed in the chain as it was designed to be an evaluation board.

7.6 Sumary

In this chapter, the chamber structure and positioner design were developed. Furthermore, a brief study of the extension of the reactive and active power of three different antennas was also performed to better understand how they correlate to the typical region separation limits. The work performed in the chamber structure as well as the positioning arm are preliminary, due to the time frame allocated to this work it was not possible to manufacture a proof of concept structure, meaning that the positioning system could also not be fully tested. A simulation was performed to validate that the system could work in the far-field using a dipole as AUT and the probes as receiver antennas surrounding the AUT. The results were consistent with the expected, showing that the cross-polarization isolation of the probe has to be improved, mainly at higher frequencies, as already stated in the previous chapter. A study of the requirements imposed by the near-to-far-field conversion algorithms was also performed to better understand the limitations of

the design. Then, a four-axis positioner arm design, capable of centering the AUT in the chamber, was proposed. Lastly, the system diagram was presented along with a description of how the developed components interact.

Chapter 8

Conclusions and Future Work

8.1 Conclusion

In this dissertation, work regarding the development of a near-field anechoic chamber was presented. The work included anechoic chamber subsystems such as the switching, measurement, control and mechanical systems.

The proposed solution for the RF switching circuit is composed of two SPDT switches that receive the signal from two LNAs connected to each of the probe's polarization and from the previous probe in the chain. The proposed design is easily scalable up to a certain number of probes, then it requires a complementary amplifier to compensate for the attenuation introduced by the switching circuit. Although the simulations show that the circuit was working as intended, the experimental measurements did not agree with the simulation. Once again, this is thought to be caused by the poorly executed soldering job.

For the measurement system a dual polarization near-field probe designed to operate from 1 to 30 GHz was analyzed and tested. The work included the simulation of four probe designs with different feed lines: parallel conductor, open microstrip, shorted microchip and shorted CPWG, from which only the last was selected to be manufactured and measured experimentally. Although the performance was not the best, mainly at the higher end of the spectrum, as demonstrated by the simulation results, the design was still manufactured so that it could be measured and compared with the simulation results. In the end, only the single polarization test probe yielded acceptable results, as the complete probe appeared to have issues with the soldering of the components. Furthermore, it was also concluded that the cables used during the measurements were damaged, further degrading the experimental data.

The work also included the control circuitry for the RF switching circuit and the positioning system, as well as, a power supply that allows for the correct operation of the system. To facilitate the power distribution and control a USB-C connector was used. Due to the selected pinout, custom cables and breakout boards were also designed and manufactured. In the end, the control system was successfully tested.

Regarding the mechanical systems only preliminary work was developed given the limited time available, meaning that the simulated proof of concept measurement system could not be manufactured. Nevertheless, the work included an analysis of the wave impedance along with the extension of reactive and active power radiated by three common antennas: electric and magnetic dipoles and a patch. The results were then compared to the region limits studied in chapter 2. It was possible to conclude that different antenna designs have different power distributions in the space that surrounds them. A simulation of the chamber structure with a dipole as the AUT and the designed probes surrounding it was also performed. Although there was a difference between the expected and computed radiation pattern, that could not be explained, their shapes were in agreement. Furthermore, the reduced cross-polarization isolation in the top end of the spectrum, previously observed in the probe simulation, was also noticeable in the obtained results. Lastly, the AUT support was developed, which allows for the adjustment of the antenna in four axes, so that it can be properly placed in the chamber.

Although part of the work was less successful than expected, either because the design could be improved or there were some issues during the experimental measurements, for the most part, the developed work was successful, leading the way for future work.

8.2 Future Work

Despite all the work developed, it represents a small part of the required work to have a fully functional near-field anechoic chamber. As already mentioned throughout the document, some problems were encountered during the experimental tests, namely poorly soldered components and defective coaxial cables in the anechoic chamber. As such, future work should include professionally soldered PCBs and new experimental tests of the RF switching circuit and near-field probe.

The developed dual-polarization probes still require improvements, namely in the achieved cross-polarization isolation. In the future, a different transmission line feed should be tested, perhaps starting with a slot line and then tapering to a coplanar parallel conductor transmission line feeding the dipole, also, different dipole shapes would be of interest. An improvement that should be studied, is to somehow place the phase center of the dipoles aligned in all planes. The experimental tests should also be repeated with professionally soldered PCBs.

The mechanical components of the measurement system still require work, as the analysis performs was preliminary. Namely, an analysis of the measurement system in the near-field to confirm that it performs as expected, for this, near-to-far-field conversion algorithms should be employed. It would also be relevant to characterize the absorber material in the used frequency range. Furthermore, a study of the minimum separation angle between probes should also be performed. After validating the system in simulation, the mechanical structure should be manufactured and full system measurements performed, for this purpose, a known AUT should be used to validate the operation, again using the conversion algorithms to process the data collected and stored during the measurements.

Appendix A

Complementary LNA

As previously mentioned, given the way the probes are connected, the signal is attenuated by a maximum of 3 dB, per probe, at the highest frequency. This attenuation is caused mainly by the RF switches used. To compensate, a complementary PCB was designed, as illustrated by Figure A.1.

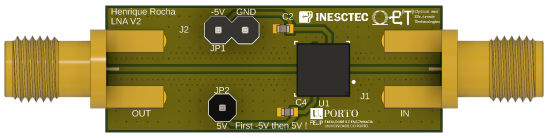

Figure A.1: LNA PCB.

The LNA used is the same as the one used in the probe design. Note that the PCB design is quite simple, including only the amplifier and two smoothing capacitors. The design was kept this way intentionally, to provide a way to measure the performance of the standalone LNA. Even though the system is only designed to operate from 1 GHz to 30 GHz, the LNA can operate from 100 MHz to 40 GHz. A more permanent solution would be to place a microcontroller and USB-C connectors to allow the amplifier board to be fully integrated into the system.

To properly measure the performance of the LNA, a calibration kit would have to be developed to cancel the effect of the transmission lines and connectors that lead up to the device itself. Nonetheless, a good approximation of the operation of the amplifier can be inferred with a port calibration up to the connectors. To measure the LNA, a similar setup to the one presented in section 4.6.2 was used. Figure A.2 shows the setup used to measure the LNA, where port one is connected to the input of the amplifier.

The measured and simulated S parameters for the enabled LNA are plotted in Figure A.3.

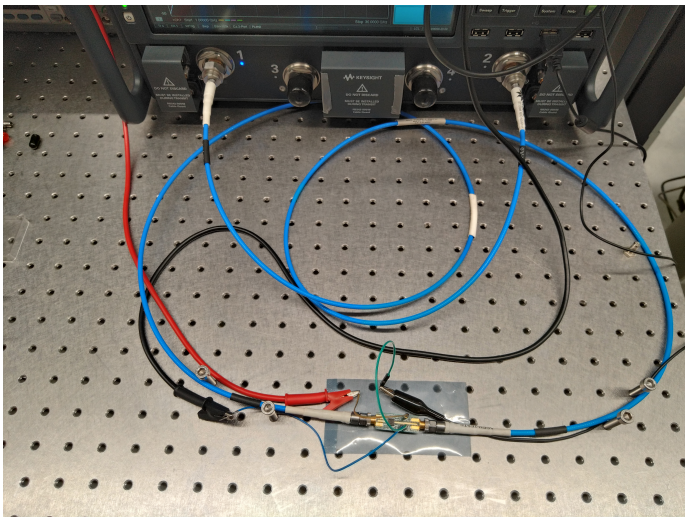

Figure A.2: LNA measurement setup.

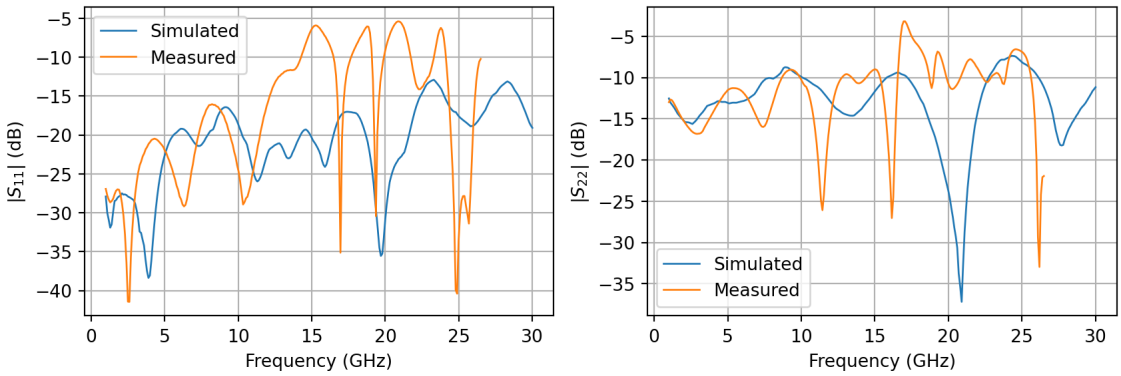

(a) Reflection S parameters.

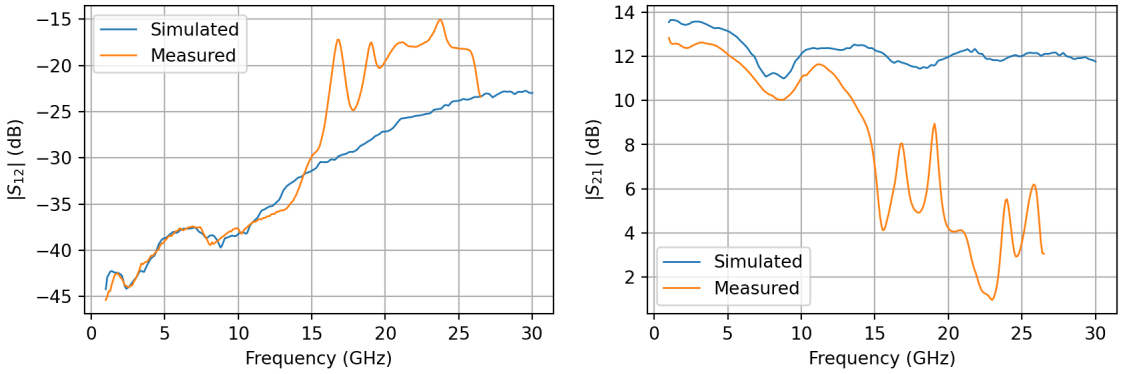

(b) Transmission S parameters.

Figure A.3: Enabled LNA simulated and measured S parameters.

Once again, we can observe that the LNA does not perform as expected, which is probably caused by a poorly executed soldering job, given that it operates as expected for low frequencies but not at high frequencies. It is also noticeable that the reflection coefficient on the output could

not be kept below −10 dB over the entire frequency range, even in simulation. Although undesired, it is expected to happen as indicated in the datasheet of the amplifier.

One more measurement was performed with the same setup but now with the LNA disabled. The measured S parameters as shown in Figure A.4.

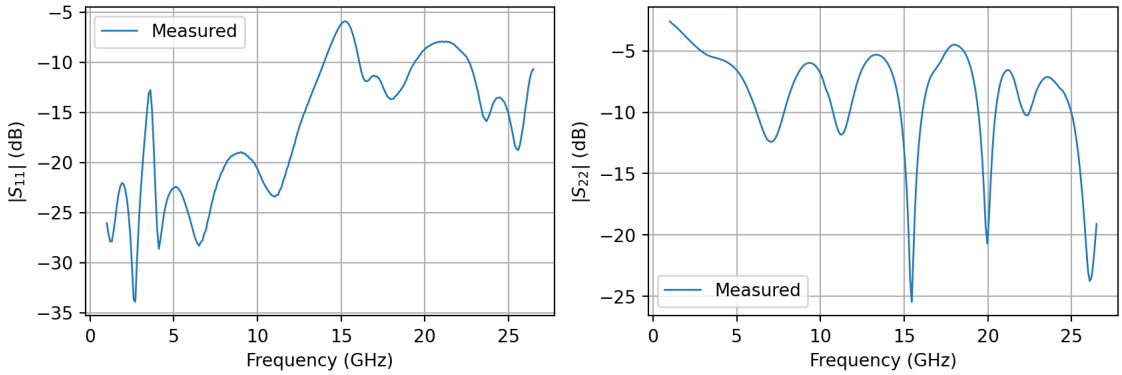

(a) Reflection S parameters.

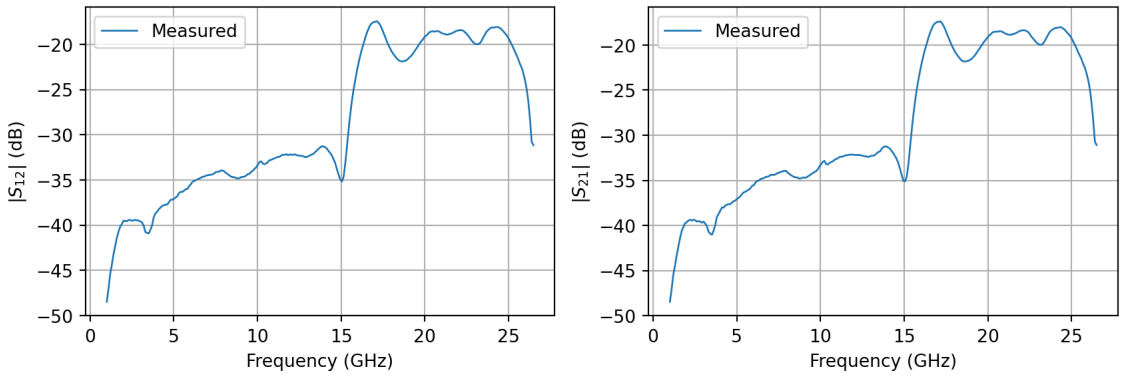

(b) Transmission S parameters.

Figure A.4: Disabled LNA measured S parameters.

From the measured data, we can observe that the LNA maintains its input matched even though it is not powered, which is a characteristic of distributed amplifiers. This characteristic means the simulation holds even when the amplifier is disabled, as its input maintains close to a 50 Ω impedance. Note that the results are not the best due to the way the amplifier was soldered, so the S_{11} is not entirely below the −10 dB design goal.

Appendix B

CPWG Line Radiation

To better understand the effect the width of a transmission line has on the amount of energy radiated, a simple simulation was performed using the model shown in Figure B.1.

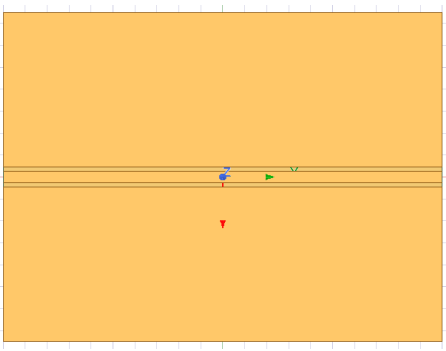

Figure B.1: Line radiation simulation model.

Given that CPWG was used in the RF switching circuit and in the feed line of the probes, this simulation also used the same transmission line. The first used the same dimensions for the transmission line and substrate thickness as the ones used in the switching circuit and the probes. To be able to compare the different models, radiation efficiency was used as a metric. In this case, the lower the radiation efficiency, the better. A radiation efficiency of 0 % would mean that no power is radiated. The radiation efficiency in this first case is 5 %, which means that 5 % of the energy, that is received by the transmission line supplied by port one (the active port), is radiated and does not reach the load (port two). To confirm that the line is matched to the desired 50 Ω Figure B.2 shows the S parameters of the transmission line. As you can observe, the line is matched as the S_{11} and S_{22} are below -17 dB, meaning that only 2 % of the power is reflected, which is negligible.

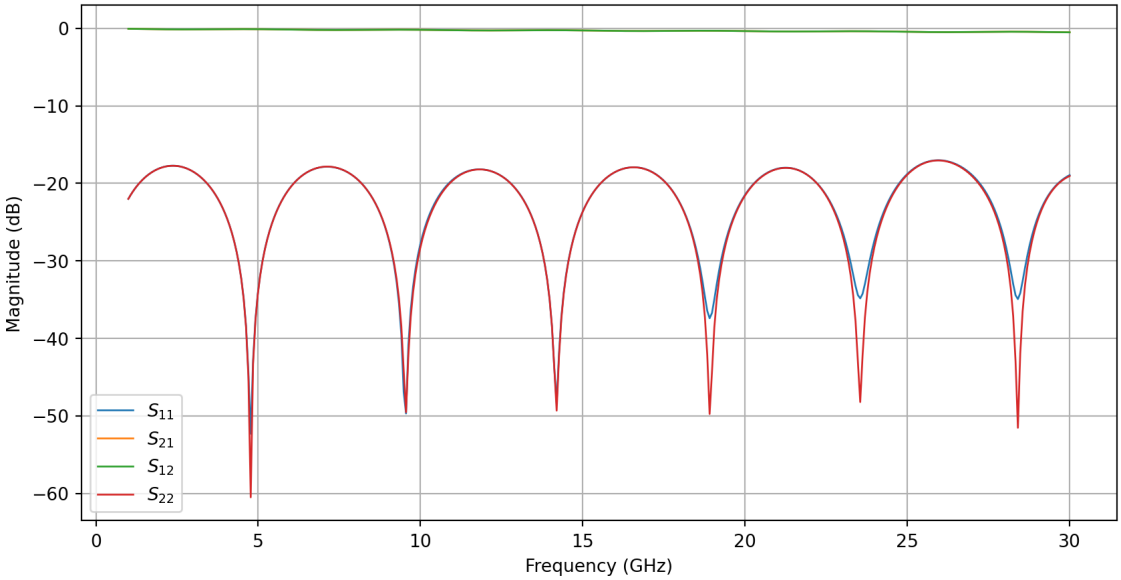

Figure B.2: Simulated S parameter for a 0.254 mm substrate height.

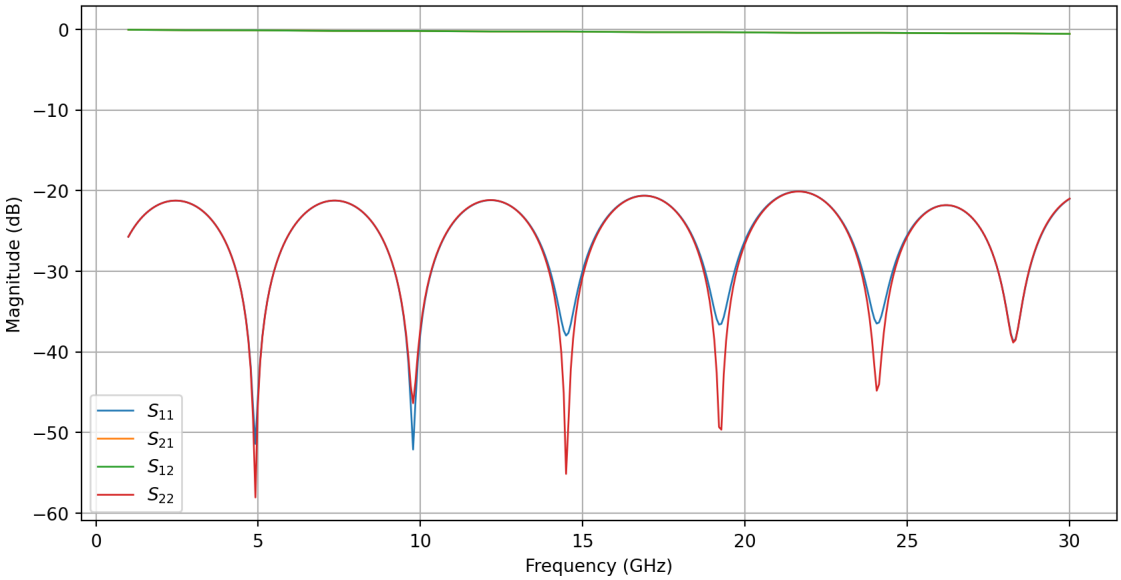

Figure B.3: Simulated S parameter for a 0.5 mm substrate height.

Repeating the simulation for a 0.5 mm thick substrate implies that the transmission line must be resized accordingly to match the desired impedance. Using the equations presented in section 4.4, the dimensions obtained were $S = 1$ mm and $W = 0.42$ mm. With the new dimensions applied to the model, the radiation efficiency increased to 22 %, representing an increase of about four times. Once again, to confirm that the line is matched to the desired 50 Ω Figure B.3 shows the S parameters of the transmission line. As you can observe, the line is matched as the S_{11} and S_{22} are below -19 dB, meaning that only 1.3 % of the power is reflected, which is negligible.

When considering the effective electric permittivity of the line in the simulations above ($\varepsilon_{\text{eff}} \approx 2.8$) the wavelength at the highest operating frequency (30 GHz) is approximately 6 mm. From the simulations performed, we can conclude that for a transmission line that has a width smaller than a tenth of the wavelength (0.6 mm), the radiation emitted by the transmission line is small (close to 5 %). However, when the line width is increased to 1 mm, which is now larger than a tenth of the wavelength, the radiated efficiency increases to 22 %, which is considerably large. This means that a transmission line should have its width reduced to a minimum to reduce line radiation.

Appendix C

Coaxial to CPWG Transition

The connection between the GPWG transmission line and the coaxial cable is achieved by using a specially designed connector. To ensure that the connector does not affect the simulation results, a separate simulation was performed to ensure that the coaxial connector performed as expected. The simulation was performed in HFSS using the 3D model of the connector retrieved from the manufacturer's website. However, the provided 3D model did not have the internal conductor separate from the insulator and the outer conductor, which is required to perform the simulation. The model was cut to the region of interest and separated into its components (metal and insulator) using SolidWorks. After obtaining the separate bodies, these were imported into HFSS, and the correct materials were assigned to the connector. The model used in the simulation is shown in Figure C.1, and the obtained S parameters are shown in C.2.

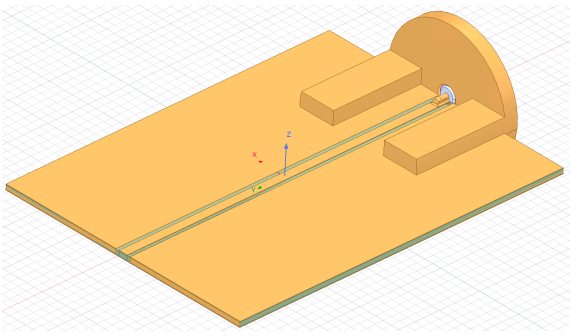

Figure C.1: Coaxial to GPWG transition simulation model.

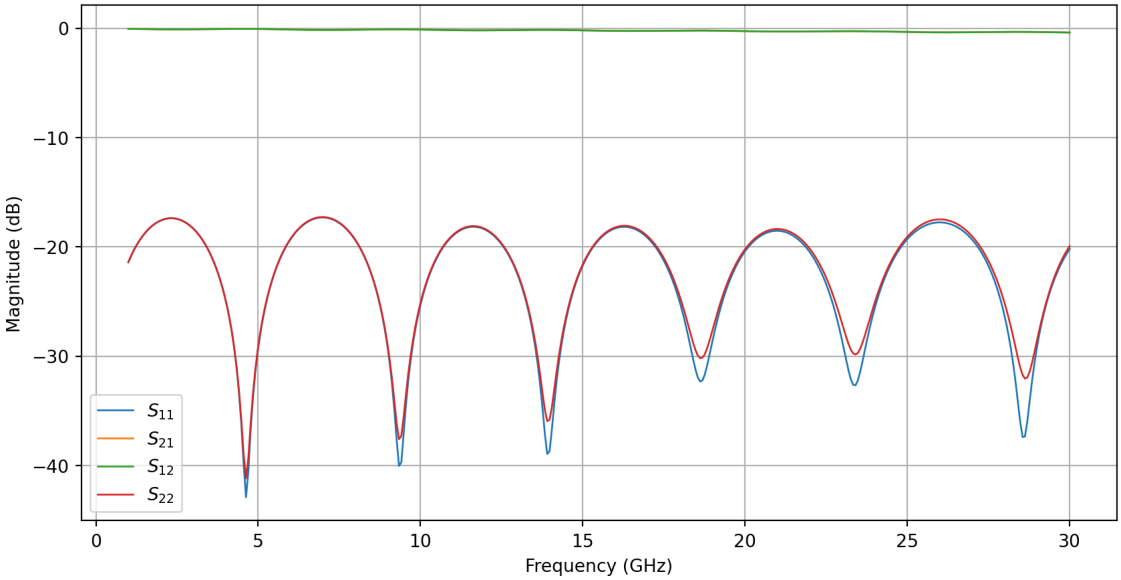

Figure C.2: Coaxial to GPWG transition S parameters.

From the simulated S parameters it is possible to conclude that the transition does not cause any undesired effects. Within the frequency range, the reflection coefficient is maintained below -15 dB, which is acceptable. Regarding the insertion loss, it is also within acceptable values, with a maximum of 0.4 dB at 30 GHz. So it is safe to say that the connector does not pose a problem in this design, further pointing to poorly soldered components.

Appendix D

Line Isolation

To confirm that the distance used for optimizing the feed line to the slot line is valid, a simple simulation was performed for each feed line used. The goal of these simulations is to ensure that the line-to-line coupling is negligible. For the effect, an isolation greater than 40 dB is considered to be sufficient. First, the isolation between microstrip lines was analyzed, and then between CPWG lines. Figures D.2 and D.1, respectively, show the model and transmission S parameters obtained after simulation.

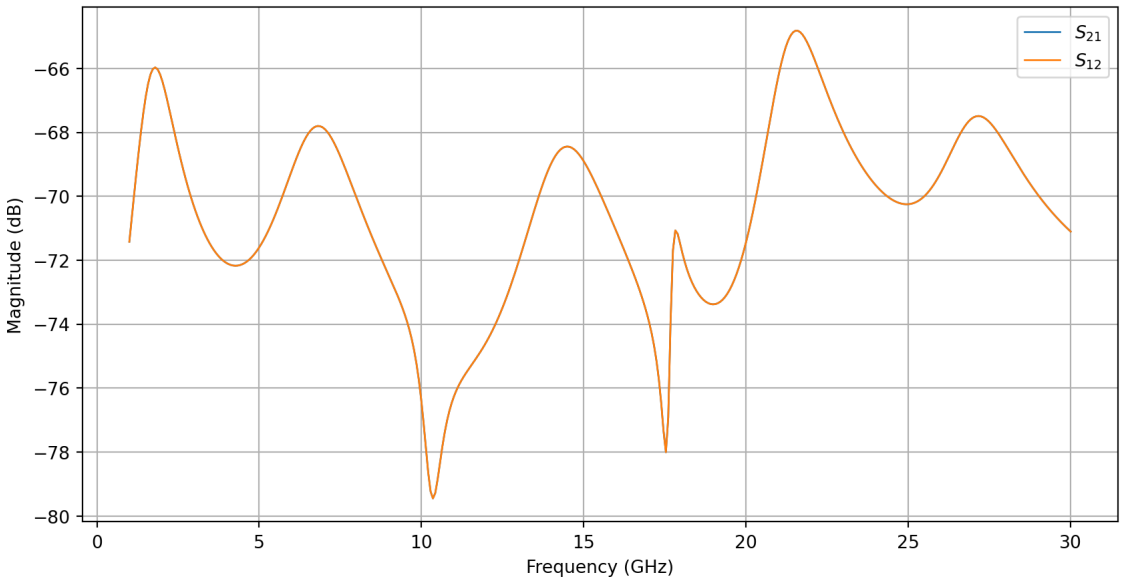

Figure D.1: Open microstrip simulated transmission S parameters.

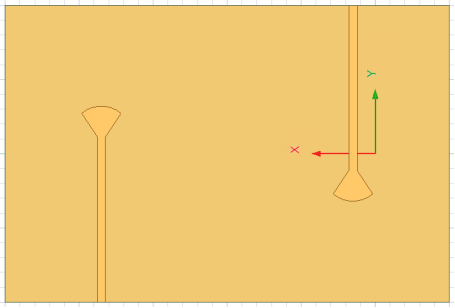

Figure D.2: Open microstrip line isolation 3D model.

The results obtained confirm that the isolation between input and output transmission lines is below -64 dB, ensuring that the distance used is suitable to consider that the coupling between lines is negligible.

Figures D.3 and D.4, respectively, show the model and transmission S parameters obtained after simulating the short microstrip transmission line.

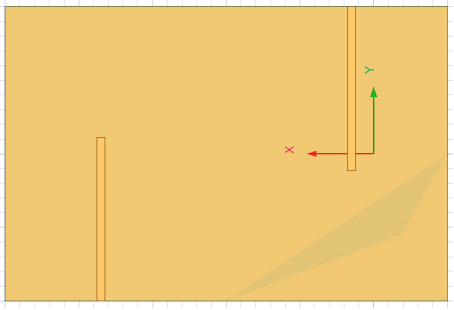

Figure D.3: Short microstrip line isolation 3D model.

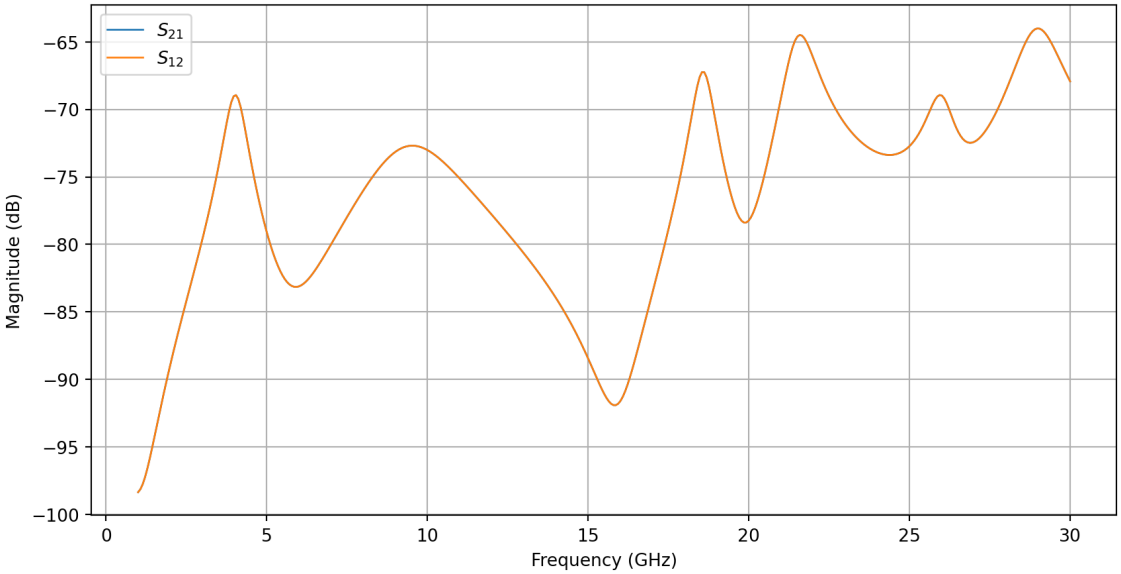

Figure D.4: Shorted microstrip simulated transmission S parameters.

Once again, the results show that the coupling between transmission lines is below $-63\,\text{dB}$ and can be neglected.

Figures D.5 and D.6, respectively, show the model and transmission S parameters obtained after simulating the CPWG transmission line.

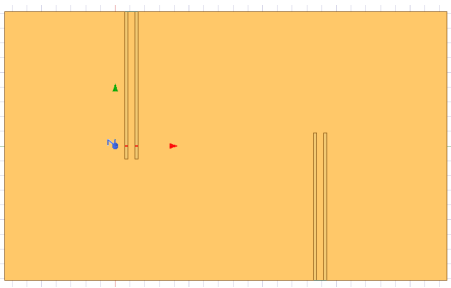

Figure D.5: CPWG line isolation 3D model.

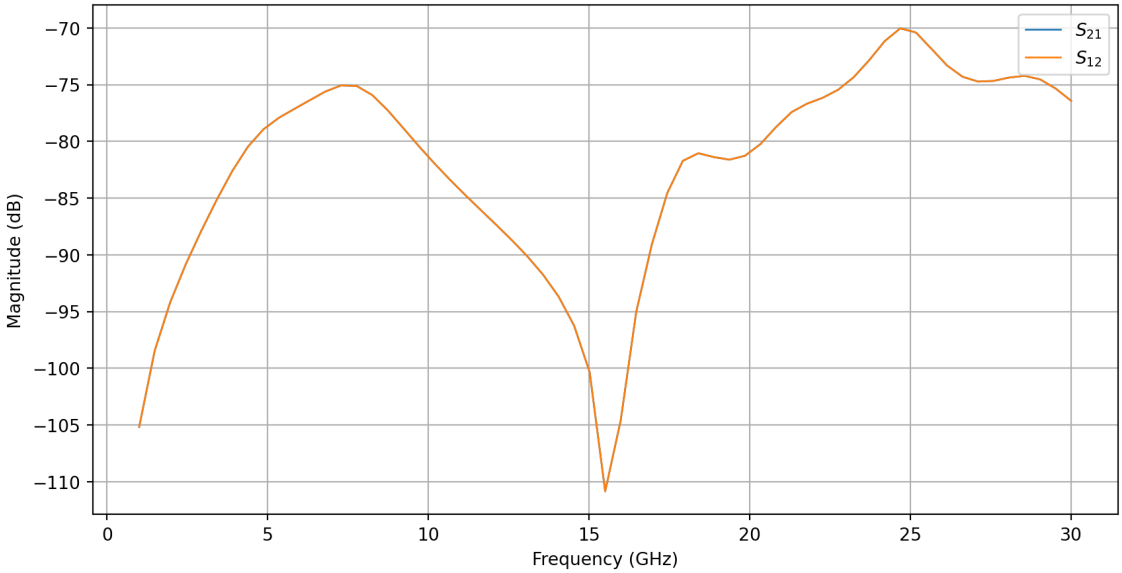

Figure D.6: CPWG simulated transmission S parameters.

Last but not least, the simulated coupling between CPWG transmission lines is below $-70\,\text{dB}$, which is perfectly acceptable.

Appendix E

CPWG to Slot Line Transition with Reduced Insertion Loss

After optimizing the CPWG to slot line transition in section 6.3.3, with the discussed limitations of the slot line width imposed by the polarization isolation, a second analysis of the transition was performed. The goal was to better understand how the S parameters were affected if the optimization was performed without limiting the minimum width of the slot line. Considering that the insertion loss increased with the width of the slot line, the ideal width should be smaller than the minimum value specified in the initial optimization. Figure E.1 shows the 3D model used for the simulations, and Figure E.2 the S parameters obtained after optimization.

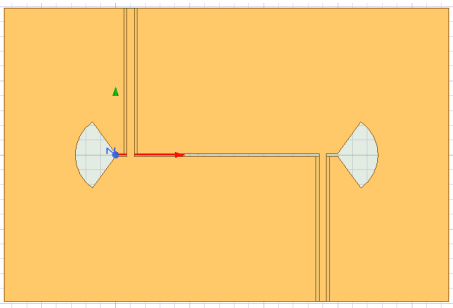

Figure E.1: CPWG to slot line transition 3D model.

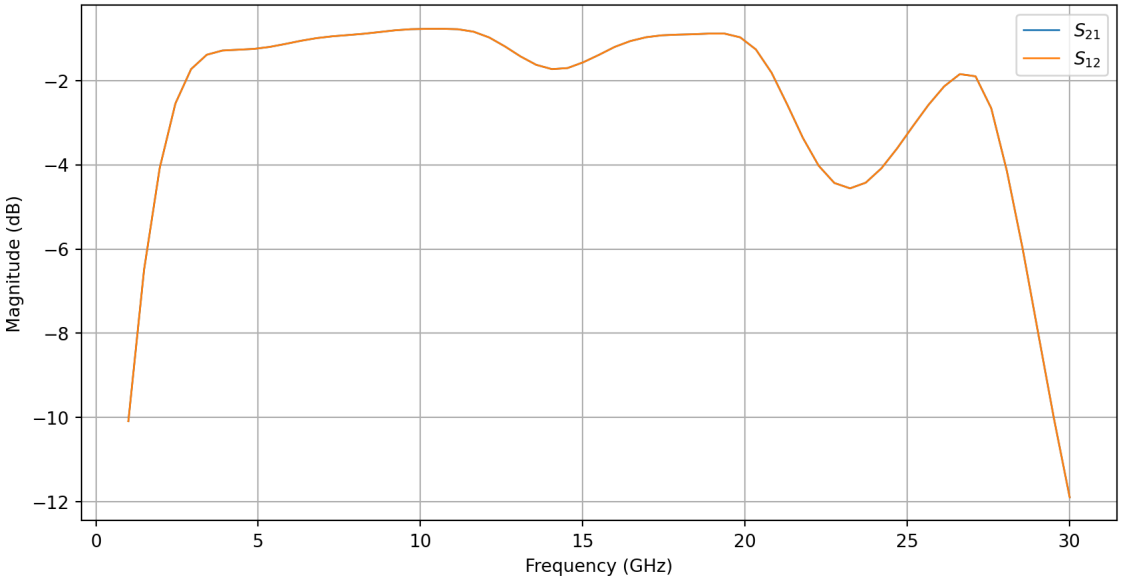

(a) Transmission parameters.

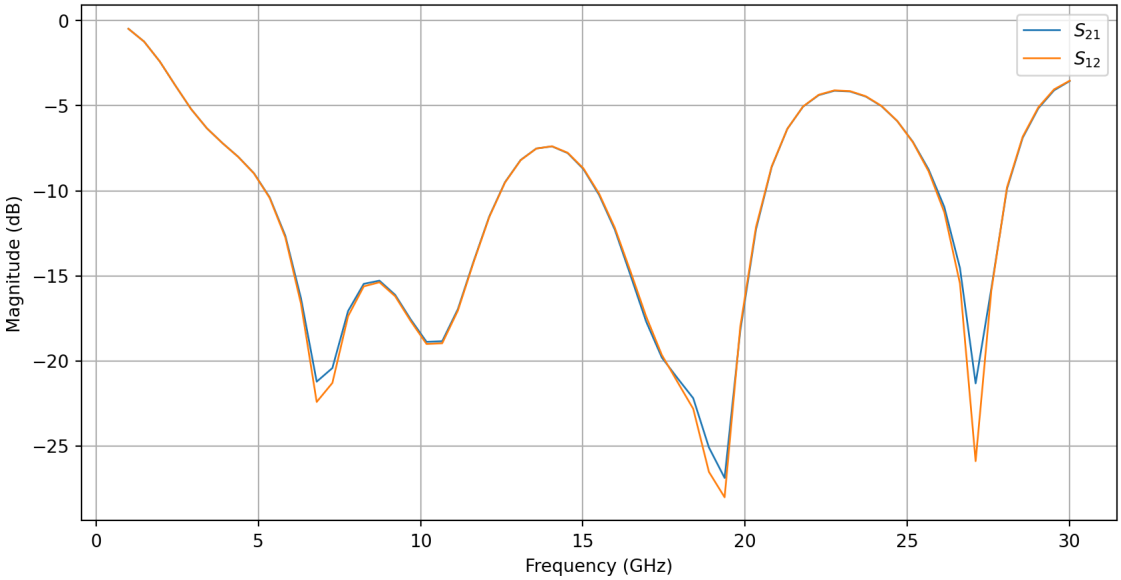

(b) Reflection parameters.

Figure E.2: CPWG to slot line transition S parameters.

As expected, it is possible to obtain a lower insertion loss with a narrower slot line. The presented results correspond to a 0.19 mm wide slot line. Note that the actual attenuation of the transmission is half the one presented in Figure E.2(a). This is because, on the signal path from one port to the other, there are two transitions, one to enter and one to exit the slot line.

Note that the only optimized parameter in this simulation was the width of the slot line, the other dimensions were unchanged, so an even lower insertion loss design may exist.

References

[1] E. Explained, *EMF - 5G Explained - How 5G Works*. [Online]. Available: https://www.emfexplained.info/?ID=25916 (visited on 04/22/2023).

[2] E. T. S. Bhd, *Design capabilities - anechoic chamber*. [Online]. Available: https://www.emits.com.my/index.php/anechoic-chamber/ (visited on 04/22/2023).

[3] C. A. Balanis, *Antenna Theory: Analysis and Design*, 4th ed. Wiley, 2016, ISBN: 978-1-118-64206-1.

[4] MVG, *Starlab a cost-effective and space-saving portable system*. [Online]. Available: https://www.mvg-world.com/media/1431/download/reference (visited on 04/22/2023).

[5] E. Miller and J. Landt, "Direct time-domain techniques for transient radiation and scattering from wires," *Proceedings of the IEEE*, vol. 68, no. 11, pp. 1396–1423, 1980. DOI: 10.1109/PROC.1980.11881.

[6] J. D. Kraus, *Antenna Theory Analysis and Design*, McGRAW-HILL, Ed. 1988.

[7] C. Balanis, "Antenna theory: a review," *Proceedings of the IEEE*, vol. 80, no. 1, pp. 7–23, 1992. DOI: 10.1109/5.119564.

[8] H. M. G. P. Santos, H. M. C. F. Salgado, and P. R. T. Pinho, "Antenna Design for Integration into Active Devices Targeting 5G and Beyond," 2020. [Online]. Available: https://www.mdpi.com/2079-9292/9/5/804.

[9] N. K. Nikolova, M. Ravan, and R. K. Amineh, *Chapter Six - Substrate-Integrated Antennas on Silicon* (Advances in Imaging and Electron Physics), M. J. Deen, Ed. Elsevier, 2012, vol. 174, pp. 391–458. DOI: https://doi.org/10.1016/B978-0-12-394298-2.00006-5. [Online]. Available: https://www.sciencedirect.com/science/article/pii/B9780123942982000065.

[10] "IEEE Standard for Definitions of Terms for Antennas - Redline," *IEEE Std 145-2013 (Revision of IEEE Std 145-1993) - Redline*, pp. 1–92, 2014.

[11] D. M. Pozar, *Microwave Engineering*, 4th ed., Inc John Wiley & Sons, Ed. Wiley, 2012.

[12] Y. Chen and R. G. Vaughan, "Determining the three-dimensional phase center of an antenna," in *2014 XXXIth URSI General Assembly and Scientific Symposium (URSI GASS)*, 2014, pp. 1–4. DOI: 10.1109/URSIGASS.2014.6929023.

[13] C. H. Walter, *Traveling wave antennas*. Peninsula Publishing, 1990.

[14] MVG, *Near-field or Far-field Antenna Measurement Chamber : Anechoic Chambers*. [Online]. Available: https://www.mvg-world.com/en/products/antenna-measurement/anechoic-chambers/near-field-or-far-field-antenna-measurement-chamber (visited on 12/30/2022).

[15] P. Pinho, H. Santos, and H. Salgado, "Design of an anechoic chamber for w-band and mmwave," *Electronics (Switzerland)*, vol. 9, 5 May 2020, ISSN: 20799292. DOI: 10.3390/electronics9050804.

[16] J. Aubin and M. Winebrand, "Side wall diffraction & optimal back wall design in elongated chambers for far-field antenna measurements at VHF/UHF frequencies," pp. 1–4, 2010. DOI: 10.1109/APS.2010.5562157.

[17] M. Winebrand, J. Aubin, and M. Boumans, "A two-Level GTD utilization in designing anechoic chambers for antenna measurements," pp. 1–4, 2009. DOI: 10.1109/APS.2009.5172308.

[18] MVG, *StarLab : Multi-probe Systems*. [Online]. Available: https://www.mvg-world.com/en/products/antenna-measurement/multi-probe-systems/starlab (visited on 12/30/2022).

[19] F. T. Faul, H. J. Steiner, and T. F. Eibert, "Near-field antenna measurements with manual collection of the measurement samples," *Advances in Radio Science*, vol. 18, pp. 17–22, Dec. 2020, ISSN: 16849973. DOI: 10.5194/ars-18-17-2020.

[20] Minikits, *Eme225-kit*. [Online]. Available: https://www.minikits.com.au/eme225 (visited on 04/25/2023).

[21] T. Singh, "Computation of beam stress and rf performance of a thin film based q-band optimized rf mems switch," *Transactions on Electrical and Electronic Materials*, vol. 16, pp. 173–178, 4 Aug. 2015, ISSN: 20927592. DOI: 10.4313/TEEM.2015.16.4.173.

[22] everithingRF, *463200000 - mega industries | waveguide switch*. [Online]. Available: https://www.everythingrf.com/products/waveguide-switches/mega-industries/678-544-463200000 (visited on 04/25/2023).

[23] R. W. World, *How rf switch works | rf switch equivalent circuits pin diode,fet*. [Online]. Available: https://www.rfwireless-world.com/Terminology/RF-Switch-working-with-equivalent-circuits.html (visited on 04/25/2023).

[24] dmcrf, *RF & Microwave Pyramidal Foam Absorber | EMC Absorbers*. [Online]. Available: https://www.dmcrf.com/rf-and-microwave-absorbers/ (visited on 12/31/2022).

[25] A. von Hippel, *Theory and application of rf/microwave absorbers*. [Online]. Available: https://www.laird.com/resources/white-papers/laird-tech-notes-theory-and-application-rf-microwave.

[26] S. Ganchev, S. Bakhtiari, and R. Zoughi, "A novel numerical technique for dielectric measurement of generally lossy dielectrics," *IEEE Transactions on Instrumentation and Measurement*, vol. 41, no. 3, pp. 361–365, 1992. DOI: 10.1109/19.153329.

[27] P. Poshala, "Signal chain noise figure analysis," 2014. [Online]. Available: https://www.ti.com/lit/an/slaa652/slaa652.pdf?ts=1687389439837%5C&ref%5C_url=https%253A%252F%252Fwww.google.com%252F.

[28] R. N. Simons, *Coplanar Waveguide Circuits, Components, and Systems*. 2001, ISBN: 978-0-471-46393-1. [Online]. Available: https://www.wiley.com/en-ie/Coplanar+Waveguide+Circuits%2C+Components%2C+and+Systems-p-9780471463931.

[29] T. Tice and J. Richmond, "Probes for microwave near-field measurements," *IRE Transactions on Microwave Theory and Techniques*, vol. 3, no. 3, pp. 32–34, 1955. DOI: 10.1109/TMTT.1955.1124943.

[30] R. C. Johnson, H. A. Ecrer, and J. S. Hollis, "Determination of far-field antenna patterns from near-field measurements," vol. 61, 1973. DOI: 10.1109/PROC.1973.9358. [Online]. Available: https://ieeexplore.ieee.org/abstract/document/1451288 (visited on 04/30/2023).

[31] P. A. Dzagbletey, J. Y. Shim, J. Y. Jeong, and J.-Y. Chung, "Dual-polarized vivaldi antenna with quarter-wave balun feeding," in *2017 Asia-Pacific International Symposium on Electromagnetic Compatibility (APEMC)*, 2017, pp. 108–110. DOI: 10.1109/APEMC.2017.7975437.

[32] G. Adamiuk, T. Zwick, and W. Wiesbeck, "Dual-orthogonal polarized vivaldi antenna for ultra wideband applications," in *MIKON 2008 - 17th International Conference on Microwaves, Radar and Wireless Communications*, 2008, pp. 1–4.

[33] X. B. Zhao, F. Wei, and X. W. Shi, "A broadband and low cross-polarization balanced dual-polarized cross quasi-yagi antenna," *International Journal of RF and Microwave Computer-Aided Engineering*, vol. 31, 3 Mar. 2021, ISSN: 1099047X. DOI: 10.1002/mmce.22537.

[34] N. Seman and M. E. Bialkowski, "Microstrip-slot transition and its applications in multilayer microwave circuits," in *Passive Microwave Components and Antennas*, V. Zhurbenko, Ed., Rijeka: IntechOpen, 2010, ch. 12. DOI: 10.5772/9415. [Online]. Available: https://doi.org/10.5772/9415.

[35] B. Shuppert, "Microstrip/slotline transitions: Modeling and experimental investigation," *IEEE Transactions on Microwave Theory and Techniques*, vol. 36, no. 8, pp. 1272–1282, 1988. DOI: 10.1109/22.3669.